

DTIC FILE COPY

12

(WT-1636)(EX)
EXTRACTED VERSION

OPERATION HARDTACK

PROJECT 5.3

In-Flight Structural Response of FJ-4 Aircraft to Nuclear Detonations

J. H. Walls, Project Officer
Bureau of Aeronautics
Washington, DC
R. W. Harr
D. A. Smith
K. C. Holmboe
G. A. Pierce
North American Aviation, Inc.
Columbus Division
Columbus, Ohio

DTIC
ELECTE
JUN 05 1987
S D
D

AD-A995 486

8 April 1965

NOTICE:

This is an extracted version of WT-1636, OPERATION HARDTACK, Project 5.3.

Approved for public release;
distribution is unlimited.

Extracted version prepared for
Director
DEFENSE NUCLEAR AGENCY
Washington, DC 20305-1000

1 September 1985

87 6 4 097

Destroy this report when it is no longer needed. Do not return to sender.

PLEASE NOTIFY THE DEFENSE NUCLEAR AGENCY
ATTN: TITL, WASHINGTON, DC 20305 1000, IF YOUR
ADDRESS IS INCORRECT, IF YOU WISH IT DELETED
FROM THE DISTRIBUTION LIST, OR IF THE ADDRESSEE
IS NO LONGER EMPLOYED BY YOUR ORGANIZATION.



UNCLASSIFIED

SECURITY CLASSIFICATION OF THIS PAGE

AD-A995486

REPORT DOCUMENTATION PAGE

1a. REPORT SECURITY CLASSIFICATION UNCLASSIFIED		1b. RESTRICTIVE MARKINGS	
2a. SECURITY CLASSIFICATION AUTHORITY		3. DISTRIBUTION / AVAILABILITY OF REPORT Approved for public release; distribution is unlimited.	
2b. DECLASSIFICATION / DOWNGRADING SCHEDULE		4. PERFORMING ORGANIZATION REPORT NUMBER(S)	
6a. NAME OF PERFORMING ORGANIZATION 1-Bureau of Aeronautics 2-North American Aviation, Inc.		5. MONITORING ORGANIZATION REPORT NUMBER(S) WT-1636 (EX)	
6b. ADDRESS (City, State, and ZIP Code) 1-Washington, DC 2-Columbus, OH		7a. NAME OF MONITORING ORGANIZATION Defense Atomic Support Agency	
8a. NAME OF FUNDING / SPONSORING ORGANIZATION		7b. ADDRESS (City, State, and ZIP Code) Washington, DC	
8b. OFFICE SYMBOL (if applicable)		9. PROCUREMENT INSTRUMENT IDENTIFICATION NUMBER	
8c. ADDRESS (City, State, and ZIP Code)		10. SOURCE OF FUNDING NUMBERS	
		PROGRAM ELEMENT NO.	PROJECT NO.
		TASK NO.	WORK UNIT ACCESSION NO.
11. TITLE (Include Security Classification) OPERATION HARDTACK; PROJECT 5.3 - In-Flight Structural Response of FJ-4 Aircraft to Nuclear Detonations, Extracted Version			
12. PERSONAL AUTHOR(S) J. H. Walls, R. W. Harr, D. A. Smith, K. C. Holmboe, and G. A. Pierce			
13a. TYPE OF REPORT	13b. TIME COVERED FROM TO	14. DATE OF REPORT (Year, Month, Day) 611003	15. PAGE COUNT 174
16. SUPPLEMENTARY NOTATION This report has had sensitive military information removed in order to provide an unclassified version for unlimited distribution. The work was performed by the Defense Nuclear Agency in support of the DoD Nuclear Test Personnel Review Program.			
17. COSATI CODES		18. SUBJECT TERMS (Continue on reverse if necessary and identify by block number)	
FIELD	GROUP	FJ-4 Aircraft Operation Hardtack	
18	3	Structural Response	
1	3	Nuclear Explosions	
19. ABSTRACT (Continue on reverse if necessary and identify by block number)			
<p>The objectives of this project were to (1) measure the effects input and structural response of the FJ-4 aircraft when subjected in flight to the effects of high-yield nuclear detonations; (2) correlate the data obtained by this project with the data obtained from the FJ-4 participation in Operation Plumbbob; and (3) define and verify the Class D delivery capability of this aircraft.</p> <p>Radiant exposure, nuclear radiation, and overpressure were the phenomena limiting the proximity of the test aircraft to the detonations. Positioning an aircraft for the collection of data was accomplished by the use of a racetrack flight pattern with the final leg traversing surface zero so that the aircraft was either tail-on or directly over detonation point at time of shock arrival.</p>			
20. DISTRIBUTION / AVAILABILITY OF ABSTRACT <input checked="" type="checkbox"/> UNCLASSIFIED/UNLIMITED <input type="checkbox"/> SAME AS RPT. <input type="checkbox"/> DTIC USERS		21. ABSTRACT SECURITY CLASSIFICATION UNCLASSIFIED	
22a. NAME OF RESPONSIBLE INDIVIDUAL MARK D. FLOHR		22b. TELEPHONE (Include Area Code) 202-325-7559	22c. OFFICE SYMBOL DNA/ISCM

DD FORM 1473, 84 MAR

83 APR edition may be used until exhausted.
All other editions are obsolete.

SECURITY CLASSIFICATION OF THIS PAGE

UNCLASSIFIED

OPERATION HARDTACK—PROJECT 5.3

IN-FLIGHT STRUCTURAL RESPONSE OF FJ-4 AIRCRAFT
TO NUCLEAR DETONATIONS

J. H. Walls, Project Officer

Bureau of Aeronautics
Washington, D. C.

R. W. Harr
D. A. Smith
K. C. Holmboe
G. A. Pierce

North American Aviation, Inc.
Columbus Division
Columbus, Ohio



Accession For	
NTIS CRA&I	<input checked="" type="checkbox"/>
DTIC TAB	<input type="checkbox"/>
Unannounced	<input type="checkbox"/>
Justification	
By	
Distribution/	
Availability Codes	
Dist	Avail and/or Special
M	

UNANNOUNCED

FOREWORD

Classified material has been removed in order to make the information available on an unclassified, open publication basis, to any interested parties. The effort to declassify this report has been accomplished specifically to support the Department of Defense Nuclear Test Personnel Review (NTPR) Program. The objective is to facilitate studies of the low levels of radiation received by some individuals during the atmospheric nuclear test program by making as much information as possible available to all interested parties.

The material which has been deleted is either currently classified as Restricted Data or Formerly Restricted Data under the provisions of the Atomic Energy Act of 1954 (as amended), or is National Security Information, or has been determined to be critical military information which could reveal system or equipment vulnerabilities and is, therefore, not appropriate for open publication.

The Defense Nuclear Agency (DNA) believes that though all classified material has been deleted, the report accurately portrays the contents of the original. DNA also believes that the deleted material is of little or no significance to studies into the amounts, or types, of radiation received by any individuals during the atmospheric nuclear test program.

ABSTRACT

The objectives were to: (1) measure the effects input and structural response of the FJ-4 aircraft when subjected in flight to the effects of high-yield nuclear detonations; (2) correlate the data obtained by this project with the data obtained from the FJ-4 participation in Operation Plumbbob; and (3) define and verify the Class D delivery capability of this aircraft.

Radiant exposure, nuclear radiation, and overpressure were the phenomena limiting the proximity of the test aircraft to the detonations. Positioning an aircraft for the collection of data was accomplished by the use of a racetrack flight pattern with the final leg traversing surface zero so that the aircraft was either tail-on or directly over the detonation point at time of shock arrival. The primary positioning equipment was the same as that used during Operation Plumbbob—modified M-33 gun-tracking radars on the ground with X-band radar beacons in the aircraft to insure positive lock-on.

A variety of instrumentation, including calorimeters, radiometers, strain gages, pressure transducers, thermocouples, film badges, and oscillographs, was used to measure and record the inputs and responses.

Each of two aircraft participated in eight surface shots with yields ranging from
Maximum weapon effects and aircraft responses measured were:

Test conditions varied from 4,000 to 16,000 feet in altitude and from 9,100 to 24,000 feet in slant range at time zero. Elevation angles of the aircraft at shock arrival varied from 6° to 85°. The only damage sustained during the tests was nonstructural, consisting of scorching of paint and miscellaneous seals during Shot Walnut.

The following are considered to be the most significant of the conclusions drawn from final analysis of the test data: (1) The methods for predicting radiant exposure and thermal response gave acceptable results for shots that were not shielded. Small amounts of shielding gave protection from the thermal output of low-yield devices, and it is concluded that shielding by ground structures in operational situations should provide an additional margin of safety for the escape of delivery aircraft if shielding is unaccounted for in the prediction techniques. (2) Correlations of predicted free-stream peak overpressures and times of shock arrival with their corresponding measured values were excellent, thus confirming the accuracy of the prediction methods. (3) The methods for predicting dynamic response were substantiated for both low- and high-yield weapons over the complete range of blast-incidence angles. (4) No engine structural damage or adverse operational effects will occur in the vicinity of low- or high-yield nuclear detonations for aircraft positions limited by other criteria. (5) In conjunction with the data obtained from Operation Plumbbob, thermal, blast, and structural response data has been obtained over a sufficiently wide range of yields and incidence angles to permit subsequent definition of the Class D delivery capability of the FJ-4B aircraft. (6) The correlations obtained justify the use of the present thermal and dynamic response prediction methods in future delivery-capability studies of similar aircraft.

FOREWORD

This report presents the final results of one of the projects participating in the military-effect programs of Operation Hardtack. Overall information about this and the other military-effect projects can be obtained from ITR-1660, the "Summary Report of the Commander, Task Unit 3." This technical summary includes: (1) tables listing each detonation with its yield, type, environment, meteorological conditions, etc.; (2) maps showing shot locations; (3) discussions of results by programs; (4) summaries of objectives, procedures, results, etc., for all projects; and (5) a listing of project reports for the military-effect programs.

PREFACE

The project was conducted by North American Aviation, Inc., Columbus Division, for the Navy Bureau of Aeronautics, Washington, D. C., with Mr. J. H. Walls acting as the Project Officer.

The operational phase of the project was conducted under the cognizance of the U. S. Naval Air Special Weapons Facility, Kirtland Air Force Base, New Mexico, with LCDR M. A. Esmiol, Jr., USN, and LT G. E. LeBlanc, Jr., USN, acting as Project Officer and Assistant Project Officer, respectively.

Mr. R. W. Harr, of North American Aviation, directed and was technically responsible for the research described in this report.

CONTENTS

ABSTRACT-----	5
FOREWORD-----	6
PREFACE-----	6
CHAPTER 1 INTRODUCTION-----	17
1.1 Objectives-----	17
1.2 Background-----	17
1.3 Theory-----	18
1.3.1 Thermal Effects-----	18
1.3.2 Nuclear Radiation-----	18
1.3.3 Overpressure Limitations-----	18
1.3.4 Dynamic Response-----	18
CHAPTER 2 PROCEDURE-----	21
2.1 Operations-----	21
2.2 Instrumentation-----	21
2.3 Data Requirements and Reduction-----	21
2.3.1 Requirements-----	21
2.3.2 Reduction-----	22
2.3.3 Correlation-----	22
CHAPTER 3 RESULTS-----	25
3.1 Radiant Exposure-----	25
3.2 Thermal Response-----	25
3.3 Thermal Stress-----	26
3.4 Nuclear Radiation-----	26
3.5 Free-Stream Peak Overpressure and Time of Shock Arrival-----	26
3.6 Dynamic Response-----	27
3.7 Wing Overpressure Survey-----	27
3.8 Engine Response-----	28
CHAPTER 4 DISCUSSION-----	80
4.1 Radiant Exposure-----	80
4.2 Thermal Response-----	81
4.3 Thermal Stresses-----	84
4.4 Nuclear Radiation-----	85
4.5 Peak Free-Stream Overpressure and Time of Shock Arrival-----	85
4.6 Dynamic Response-----	86
4.6.1 Measured Response-----	86
4.6.2 Calculated Response-----	86
4.6.3 Correlation of Maximum Responses-----	86
4.6.4 Rigid-Aircraft Response-----	87
4.6.5 Wing Structural Response-----	88

4.6.6 Factors Affecting the Delivery Capability	89
4.7 Wing-Pressure Survey	89
4.8 Engine Response	90
 CHAPTER 5 CONCLUSIONS AND RECOMMENDATIONS	 94
5.1 Conclusions	94
5.2 Recommendations	95
 APPENDIX A THERMAL-EFFECT THEORY	 96
A.1 Computational Procedure for Radiant Exposure	96
A.1.1 Transmissivity	98
A.1.2 Albedo	102
A.2 Computational Procedure for Irradiance	102
A.3 Thermal Response	103
A.3.1 Temperature-Time History of a Thin Skin	103
A.3.2 Thin-Skin Maximum Temperature Rise	105
A.3.3 Honeycomb-Panel Temperature-Time Histories	105
A.3.4 Honeycomb Faceplate Maximum Temperature Rise	106
A.3.5 Combined Flyaway and Convective Cooling Factor, (1-FH)	107
A.3.6 Turbulent-Heat-Transfer Coefficient	107
A.4 Thermal-Stress Theory	108
 APPENDIX B NUCLEAR-RADIATION THEORY	 117
B.1 Total Nuclear Dose	117
B.2 Relative Air Density	117
 APPENDIX C BLAST-PARAMETER THEORY	 118
C.1 Free-Stream Overpressure	118
C.1.1 Free-Stream Peak Overpressure	118
C.1.2 Time History of Overpressure	118
C.2 Time of Shock Arrival	118
C.3 Shock-Front-Propagation Velocity	119
C.4 Particle Velocity Behind the Shock Front	119
C.4.1 Peak Particle Velocity	119
C.4.2 Time History of Particle Velocity	119
C.5 Density Behind the Shock Front	119
C.5.1 Peak Density Behind the Shock Front	119
C.5.2 Time History of Density Behind the Shock Front	120
C.6 Positive-Phase Duration	120
C.7 Time Histories for a Moving Receiver	120
 APPENDIX D DYNAMIC-RESPONSE THEORY	 122
D.1 Basic Considerations	122
D.2 Detailed Formulations	122
 APPENDIX E INSTRUMENTATION AND SPECIAL EQUIPMENT	 126
E.1 Instrumentation	126
E.1.1 Primary Instrumentation	126
E.1.2 Comments and Miscellaneous Instrumentation	126
E.2 Special Equipment	127

E.2.1 Rotating Navigation Light - - - - -	127
E.2.2 Thermal-Radiation Closure - - - - -	127
APPENDIX F REDUCED THERMAL DATA - - - - -	139
APPENDIX G ENGINE-RESPONSE DATA - - - - -	162
REFERENCES - - - - -	171
TABLES	
3.1 Summary of Shot Data - - - - -	29
3.2 Positions of Test Aircraft at Time of Burst and Time of Shock Arrival - - - - -	29
3.3 Atmospheric Conditions at Time of Shot - - - - -	30
3.4 Flight Conditions of Test Aircraft at Time of Burst and Time of Shock Arrival - - - - -	31
3.5 Calculated and Measured Radiant Exposure Data - - - - -	32
3.6 Calculated and Measured Values of Maximum Temperature Rise for Selected Thermocouple Locations - - - - -	33
3.7 Calculated and Measured Thermal-Stress Increments - - - - -	34
3.8 Measured and Calculated Nuclear Dose - - - - -	34
3.9 Measured and Calculated Values of Peak Free-Stream Overpressure and Time of Shock Arrival - - - - -	35
3.10 Shock-Wave Parameters - - - - -	35
3.11 Calculated and Measured Maximum Values of Aircraft Stability Variables After Shock Arrival - - - - -	36
3.12 Calculated and Measured Maximum Perturbation Values of Wing Bending-Moment Stress After Shock Arrival, Percent Limit Allowable - - - - -	37
3.13 Calculated and Measured Maximum Perturbation Values of Wing Shear Stress After Shock Arrival, Percent Limit Allowable - - - - -	38
A.1 Intermediate Parameters Used in Calculation of Radiant Exposure - - - - -	111
A.2 Parameter Values Used in Calculation of Heat Capacity, G, for Thin Skins - - - - -	112
A.3 Combined Flyaway and Convective Cooling Factors for Selected Thermocouple Locations - - - - -	112
A.4 Flyaway Factors Used in the Thermal-Response Analysis - - - - -	113
A.5 Values Used in Calculation of Honeycomb Thermal-Response Parameter - - - - -	113
E.1 Legend for Figure E.1 for Strain-Gage Installations - - - - -	129
E.2 Legend for Figure E.1 for Thermocouple Locations - - - - -	129
E.3 Legend for Figure E.2 for Miscellaneous Installations - - - - -	131
E.4 Recording Summary for Oscillographs A and B - - - - -	132
E.5 Recording Summary for Oscillographs C and D - - - - -	133
E.6 Recording Summary for Photorecorder - - - - -	134
FIGURES	
1.1 FJ-4 aircraft instrumented for Operation Hardtack - - - - -	20
2.1 Typical FJ-4 test aircraft flight profile, Aircraft 139467, Shot Koa - - - - -	24
3.1 Comparison of calculated with measured generalized thermal pulse taken from normal 160° radiometer, Aircraft 139310, Shot Yellowwood - - - - -	39
3.2 Comparison of calculated with measured generalized thermal pulse taken from direct 160° radiometer, Aircraft 139310, Shot	

Yellowwood-----	39
3.3 Comparison of calculated with measured radiant exposure taken from normal calorimeters and integrated normal radiometer, Aircraft 139310, Shot Yellowwood-----	40
3.4 Comparison of calculated with measured radiant exposure taken from direct calorimeters and integrated direct radiometer, Aircraft 139310, Shot Yellowwood-----	40
3.5 Comparison of calculated with measured generalized thermal pulse taken from normal 160° radiometer, Aircraft 139310, Shot Walnut -----	41
3.6 Comparison of calculated with measured generalized thermal pulse taken from direct 160° radiometer, Aircraft 139310, Shot Walnut -----	41
3.7 Comparison of calculated with measured radiant exposure taken from normal calorimeter and integrated normal radiometer, Aircraft 139310, Shot Walnut-----	42
3.8 Comparison of calculated with measured radiant exposure taken from direct calorimeters and integrated direct radiometer, Aircraft 139310, Shot Walnut-----	42
3.9 Comparison of calculated with measured radiant exposure for individual instruments in Shots Butternut, Yellowwood, Magnolia, and Walnut-----	43
3.10 Comparison of measured with calculated maximum temperature rise of selected thermocouple locations using calculated radiant exposure ----	44
3.11 Comparison of measured with calculated maximum temperature rise of selected thermocouple locations using measured radiant exposure from normal 160° calorimeter-----	45
3.12 Comparison of measured with calculated maximum temperature rise of selected thermocouple locations from calculated temperature- time histories using irradiance from normal 160° radiometer -----	46
3.13 Comparison of calculated with measured temperature-time histories of Fuselage Station 210.810, Aircraft 139310, Shot Yellowwood -----	47
3.14 Comparison of calculated with measured temperature-time histories of Fuselage Station 248.155, Aircraft 139310, Shot Yellowwood-----	47
3.15 Comparison of calculated with measured temperature-time histories of Fuselage Stations 333.625 and 389.125, Aircraft 139310, Shot Yellowwood-----	48
3.16 Comparison of calculated with measured temperature-time histories of Wing Stations 170.0 and 223.75, Aircraft 139310, Shot Yellowwood-----	48
3.17 Comparison of calculated with measured temperature-time histories of aileron honeycomb faceplate, Aircraft 139310, Shot Yellowwood-----	49
3.18 Comparison of calculated with measured temperature-time histories of flap honeycomb faceplate, Aircraft 139310, Shot Yellowwood-----	49
3.19 Comparison of calculated with measured temperature-time histories of elevator honeycomb faceplate, Aircraft 139310, Shot Yellowwood -----	50
3.20 Comparison of calculated with measured temperature-time histories of Fuselage Station 210.810, Aircraft 139310, Shot Walnut -----	50
3.21 Comparison of calculated with measured temperature-time histories of Fuselage Station 248.155, Aircraft 139310, Shot Walnut -----	50
3.22 Comparison of calculated with measured temperature-time histories of Fuselage Stations 333.625 and 389.125, Aircraft 139310, Shot Walnut-----	51
3.23 Comparison of calculated with measured temperature-time histories of Wing Stations 170.0 and 223.75, Aircraft 139310, Shot Walnut-----	51

3.24	Comparison of calculated with measured temperature-time histories of aileron honeycomb faceplate, Aircraft 139310, Shot Walnut - - - - -	52
3.25	Comparison of calculated with measured temperature-time histories of flap honeycomb faceplate and backplate, Aircraft 139310, Shot Walnut - - - - -	52
3.26	Comparison of calculated with measured temperature-time histories of elevator honeycomb faceplate and backplate, Aircraft 139310, Shot Walnut - - - - -	53
3.27	Measured temperature-time histories of top surface flap and elevator honeycomb faceplates, Aircraft 139310, Shot Walnut - - - - -	53
3.28	Correlation for nose-boom overpressures reduced to a 1-kt homogeneous sea-level atmosphere - - - - -	54
3.29	Correlation for fuselage measured overpressures reduced to a 1-kt homogeneous sea-level atmosphere - - - - -	54
3.30	Correlation for measured times of shock arrival reduced to a 1-kt homogeneous sea-level atmosphere - - - - -	55
3.31	Blast-induced normal-load factor versus time, Aircraft 139310, Shot Magnolia - - - - -	56
3.32	Angle of attack (due to blast-induced heaving motion) versus time, Aircraft 139310, Shot Magnolia - - - - -	56
3.33	Angle of pitch (blast-induced) versus time, Aircraft 139310, Shot Magnolia - - - - -	57
3.34	Rate of angle of pitch (blast-induced) versus time, Aircraft 139310, Shot Magnolia - - - - -	57
3.35	Blast-induced, incremental bending stress at left and right root, Wing Station 17.5, versus time, Aircraft 139310, Shot Magnolia - - - - -	58
3.36	Blast-induced, incremental bending stress at Wing Station 68 (21-percent chord) versus time, Aircraft 139310, Shot Magnolia - - - - -	58
3.37	Blast-induced, incremental bending stress at Wing Station 91.4 versus time, Aircraft 139310, Shot Magnolia - - - - -	59
3.38	Blast-induced, incremental bending stress at Wing Station 111 (35-percent chord) versus time, Aircraft 139310, Shot Magnolia - - - - -	59
3.39	Blast-induced, incremental bending stress at Wing Station 111 (40-percent chord) versus time, Aircraft 139310, Shot Magnolia - - - - -	60
3.40	Blast-induced, incremental bending stress at Wing Station 131 (41-percent chord) versus time, Aircraft 139310, Shot Magnolia - - - - -	60
3.41	Blast-induced, incremental bending stress of outer-panel-root, Wing Station 173, versus time, Aircraft 139310, Shot Magnolia - - - - -	61
3.42	Blast-induced, incremental shear stress of forward spar at Butt Plane 48 versus time, Aircraft 139310, Shot Magnolia - - - - -	61
3.43	Blast-induced, incremental shear stress of forward spar at inboard Wing Station 56.9 versus time, Aircraft 139310, Shot Magnolia - - - - -	62
3.44	Blast-induced, incremental shear stress of forward spar web at outboard Wing Station 56.9 versus time, Aircraft 139310, Shot Magnolia - - - - -	62
3.45	Blast-induced, incremental shear stress of rear spar at inboard Wing Station 60.4 versus time, Aircraft 139310, Shot Magnolia - - - - -	63
3.46	Blast-induced, incremental shear stress of aft spar at outboard Wing Station 60.4 versus time, Aircraft 139310, Shot Magnolia - - - - -	63
3.47	Blast-induced, incremental shear stress of forward spar at inboard Wing Station 105 versus time, Aircraft 139310, Shot Magnolia - - - - -	64
3.48	Blast-induced, incremental shear stress of aft spar at inboard Wing Station 105 versus time, Aircraft 139310, Shot Magnolia - - - - -	64

3.49	Blast-induced, incremental shear stress of forward spar at inboard Wing Station 153 versus time, Aircraft 139310, Shot Magnolia-----	65
3.50	Pressure gage locations for the wing static-pressure survey-----	66
3.51	Chordwise incremental pressure distributions at time intervals following shock arrival at Wing Station 82.2 for Aircraft 139467, Shot Walnut-----	67
3.52	Chordwise incremental pressure distributions at time intervals following shock arrival at Wing Station 141.0 for Aircraft 139467, Shot Walnut-----	68
3.53	Chordwise incremental pressure distributions at time intervals following shock arrival at Wing Station 175.8 for Aircraft 139467, Shot Walnut-----	69
3.54	Chordwise incremental pressure distributions at time intervals following shock arrival at Wing Station 82.2 for Aircraft 139467, Shot Tobacco-----	70
3.55	Chordwise incremental pressure distributions at time intervals following shock arrival at Wing Station 141.0 for Aircraft 139467, Shot Tobacco-----	71
3.56	Chordwise incremental pressure distributions at time intervals following shock arrival at Wing Station 175.8 for Aircraft 139467, Shot Tobacco-----	72
3.57	Chordwise incremental pressure distributions at time intervals following shock arrival at Wing Station 82.2 for Aircraft 139310, Shot Butternut-----	73
3.58	Chordwise incremental pressure distributions at time intervals following shock arrival at Wing Station 141.0 for Aircraft 139310, Shot Butternut-----	74
3.59	Chordwise incremental pressure distributions at time intervals following shock arrival at Wing Station 175.8 for Aircraft 139310, Shot Butternut-----	75
3.60	Incremental section lift following shock arrival at Wing Stations 82.2, 141.0, and 175.8, Aircraft 139467, Shot Walnut-----	76
3.61	Incremental section lift following shock arrival at Wing Stations 82.2, 141.0, and 175.8, Aircraft 139467, Shot Tobacco-----	76
3.62	Incremental section lift following shock arrival at Wing Stations 82.2, 141.0, and 175.8, Aircraft 139310, Shot Butternut-----	77
3.63	Diffraction-pulse error function as a function of blast-wave incidence angle-----	77
3.64	Throttle position, engine speed and fuel flow for Aircraft 139310, Shot Koa-----	78
3.65	Compressor inlet and discharge pressures for Aircraft 139310, Shot Koa-----	78
3.66	Fuel inlet pressure and tailpipe total temperature for Aircraft 139310, Shot Koa-----	79
3.67	Indicated altitude, airspeed and outside-air temperature for Aircraft 139310, Shot Koa-----	79
4.1	Thermal damage on the aft fuselage of Aircraft 139310, Shot Walnut-----	92
4.2	Closeup view of thermal damage on the aft fuselage of Aircraft 139310, Shot Walnut-----	92
4.3	Port external fuel drop tank thermal damage, Aircraft 139310, Shot Walnut-----	93
A.1	Combined effect of flyaway and convective cooling on honeycomb faceplate temperature rises-----	114

A.2	Thermal-response parameter for alleron and flap honeycomb panels as a function of h_g and η -----	115
A.3	Thermal-response parameter for elevator honeycomb panel as a function of h_g and η -----	116
C.1	Free-air duration of positive phase versus slant range for a 1-kt burst in a homogeneous sea-level atmosphere-----	121
E.1	Perspective instrumentation drawing of FJ-4 aircraft showing strain gage and thermocouple installations -----	128
E.2	Perspective instrumentation drawing of FJ-4 aircraft showing miscellaneous installations -----	130
E.3	Perspective drawing of instrumented wing tank for FJ-4 aircraft-----	135
E.4	Perspective drawing showing instrumentation of engine and cockpit of FJ-4 aircraft-----	136
E.5	Exterior view of fixed aft curtain and collapsible canopy hood -----	137
E.6	Actuation of the collapsible canopy hood -----	137
E.7	Interior view of windshield curtain in the closed position -----	138
F.1	Comparison of calculated with measured generalized thermal pulse taken from normal 160° radiometer, Aircraft 139467, Shot Butternut-----	140
F.2	Comparison of calculated with measured generalized thermal pulse taken from direct 160° radiometer, Aircraft 139467, Shot Butternut -----	140
F.3	Comparison of calculated with measured radiant exposure taken from normal calorimeter and integrated normal radiometer, Aircraft 139467, Shot Butternut -----	141
F.4	Comparison of calculated with measured radiant exposure taken from direct calorimeter and integrated direct radiometer, Aircraft 139467, Shot Butternut -----	141
F.5	Comparison of calculated with measured temperature-time histories of Fuselage Stations 210.810, 333.625 and 389.125, Aircraft 139467, Shot Butternut -----	142
F.6	Comparison of calculated with measured temperature-time histories of alleron and elevator honeycomb faceplates, Aircraft 139467, Shot Butternut -----	142
F.7	Comparison of calculated with measured generalized thermal pulse taken from normal 160° radiometer, Aircraft 139310, Shot Butternut-----	143
F.8	Comparison of calculated with measured generalized thermal pulse taken from direct 160° radiometer, Aircraft 139310, Shot Butternut -----	143
F.9	Comparison of calculated with measured radiant exposure taken from normal calorimeter and integrated normal radiometer, Aircraft 139310, Shot Butternut -----	144
F.10	Comparison of calculated with measured radiant exposure taken from direct calorimeter and integrated direct radiometer, Aircraft 139310, Shot Butternut -----	144
F.11	Comparison of calculated with measured temperature-time histories of Fuselage Stations 210.810 and 333.625, Aircraft 139310, Shot Butternut -----	145
F.12	Comparison of calculated with measured temperature-time histories of alleron and elevator honeycomb faceplates, Aircraft 139310, Shot Butternut -----	145
F.13	Measured radiant exposure taken from direct 90° and 160° calorimeters, Aircraft 139467, Shot Koa -----	146
F.14	Measured temperature-time histories of selected thermocouple locations, Aircraft 139467, Shot Koa-----	147

F.15	Measured radiant exposure taken from normal 160° calorimeter, Aircraft 139310, Shot Koa -----	148
F.16	Measured radiant exposure taken from direct 90° and 160° calorimeters, Aircraft 139310, Shot Koa -----	148
F.17	Measured temperature-time histories of selected thermocouple locations, Aircraft 139310, Shot Koa -----	149
F.18	Comparison of calculated with measured generalized thermal pulse taken from normal 160° radiometer, Aircraft 139467, Shot Magnolia -----	150
F.19	Comparison of calculated with measured generalized thermal pulse taken from direct 160° radiometer, Aircraft 139467, Shot Magnolia -----	150
F.20	Comparison of calculated with measured radiant exposure taken from normal calorimeter and integrated normal radiometer, Aircraft 139467, Shot Magnolia -----	151
F.21	Comparison of calculated with measured radiant exposure taken from direct calorimeter and integrated direct radiometer, Aircraft 139467, Shot Magnolia -----	151
F.22	Comparison of calculated with measured temperature-time histories of Fuselage Stations 210.810, 333.625, and 389.125, Aircraft 139467, Shot Magnolia -----	152
F.23	Comparison of calculated with measured temperature-time histories of aileron and elevator honeycomb faceplates, Aircraft 139467, Shot Magnolia -----	152
F.24	Measured temperature-time history of nose radome coating, Aircraft 139467, Shot Magnolia -----	153
F.25	Comparison of calculated with measured generalized thermal pulse taken from normal 160° radiometer, Aircraft 139310, Shot Magnolia -----	154
F.26	Comparison of calculated with measured generalized thermal pulse taken from direct 160° radiometer, Aircraft 139310, Shot Magnolia -----	154
F.27	Comparison of calculated with measured radiant exposure taken from normal calorimeter and integrated normal radiometer, Aircraft 139310, Shot Magnolia -----	155
F.28	Comparison of calculated with measured radiant exposure taken from direct calorimeter and integrated direct radiometer, Aircraft 139310, Shot Magnolia -----	155
F.29	Comparison of calculated with measured temperature-time histories of Fuselage Station 210.81, Aircraft 139310, Shot Magnolia -----	156
F.30	Comparison of calculated with measured temperature-time histories of Fuselage Station 248.155, Aircraft 139310, Shot Magnolia -----	156
F.31	Comparison of calculated with measured temperature-time histories of Fuselage Stations 333.625 and 389.125, Aircraft 139310, Shot Magnolia -----	157
F.32	Comparison of calculated with measured temperature-time histories of Wing Stations 170.0 and 223.75, Aircraft 139310, Shot Magnolia -----	157
F.33	Comparison of calculated with measured temperature-time histories of aileron honeycomb faceplate, Aircraft 139310, Shot Magnolia -----	158
F.34	Comparison of calculated with measured temperature-time histories of flap honeycomb faceplate, Aircraft 139310, Shot Magnolia -----	158
F.35	Comparison of calculated with measured temperature-time histories of elevator honeycomb faceplate and backplate, Aircraft 139310, Shot Magnolia -----	159
F.36	Comparison of calculated with measured generalized thermal pulse taken from direct 160° radiometer, Aircraft 139467, Shot Walnut -----	160

F.37 Measured radiant exposure taken from direct 90° and 160° calorimeters and integrated direct 160° radiometer, Aircraft 139467, Shot Walnut -----	160
F.38 Measured temperature-time history of Fuselage Station 389.125, Aircraft 139467, Shot Walnut -----	161
F.39 Measured temperature-time histories of selected thermocouple locations, Aircraft 139467, Shot Walnut -----	161
G.1 Throttle position, engine speed and fuel flow for Aircraft 139467, Shot Koa -----	163
G.2 Compressor inlet and discharge pressures for Aircraft 139467, Shot Koa -----	163
G.3 Fuel inlet pressure and tailpipe total temperature for Aircraft 139467, Shot Koa -----	164
G.4 Indicated altitude, airspeed and outside-air temperature for Aircraft 139467, Shot Koa -----	164
G.5 Throttle position, engine speed and fuel flow for Aircraft 139467, Shot Yellowwood -----	165
G.6 Compressor inlet and discharge pressures for Aircraft 139467, Shot Yellowwood -----	165
G.7 Fuel inlet pressure and tailpipe total temperature for Aircraft 139467, Shot Yellowwood -----	166
G.8 Indicated altitude, airspeed and outside-air temperature for Aircraft 139467, Shot Yellowwood -----	166
G.9 Throttle position, engine speed and fuel flow for Aircraft 139467, Shot Tobacco -----	167
G.10 Compressor inlet and discharge pressure for Aircraft 139467, Shot Tobacco -----	167
G.11 Fuel inlet pressure and tailpipe total temperature for Aircraft 139467, Shot Tobacco -----	168
G.12 Indicated altitude, airspeed and outside-air temperature for Aircraft 139467, Shot Tobacco -----	168
G.13 Throttle position, engine speed and fuel flow for Aircraft 139467, Shot Rose -----	169
G.14 Compressor inlet and discharge pressures for Aircraft 139467, Shot Rose -----	169
G.15 Fuel inlet pressure and tailpipe total temperature for Aircraft 139467, Shot Rose -----	170
G.16 Indicated altitude, airspeed and outside-air temperature for Aircraft 139467, Shot Rose -----	170

Chapter 1

INTRODUCTION

1.1 OBJECTIVES

The objectives were to: (1) measure the effects input and structural response of the FJ-4 aircraft when subjected in flight to the effects of high-yield nuclear detonations; (2) correlate the data obtained by this project with the data obtained from the FJ-4 participation during Operation Plumbbob; and (3) define and verify the Class D delivery capability of this aircraft.

The above objectives included the following: (1) confirmation of aircraft response parameters for the longer durations of effects characteristic of high-yield nuclear detonations, in order to improve predictions of safe escape criteria; (2) collection of response data for higher overpressures and lower shock- and thermal-incidence angles (lower altitudes) than were practicable in Operation Plumbbob; (3) extension of the Plumbbob study of the transient pressure distributions on the wing in order to better define the effects of shock interactions on the aerodynamic load characteristics; and (4) collection of thermal response data.

1.2 BACKGROUND

Since the firing of the first nuclear device during Operation Trinity (1945), a major problem associated with the use of nuclear weapons has been the formulation and substantiation of methods for predicting their effects. With the concept of delivering nuclear weapons from an airborne carrier, there arose the additional problem of defining the response of aircraft structures to the effects of such weapons so that safe delivery techniques could be developed. Since it was not possible to accurately simulate these problems in laboratories, full-scale nuclear-test programs were established to provide the basic data necessary for methods development.

The FJ-4B aircraft has been designated by the Navy to deliver nuclear weapons. Since no aircraft of this series were available for testing purposes, two FJ-4's were modified by the addition of FJ-4B control surfaces and utilized instead. This modification provided structural similarity of the two models.

Operation Hardtack was the latest in a series of nuclear tests and was the second test series in which FJ-4 aircraft participated. During Operation Plumbbob, conducted in 1957, two FJ-4 aircraft participated to obtain blast-gust response data for swept-wing aircraft and thermal-response data for both thin-skin and aluminum-honeycomb-sandwich materials. Since Operation Plumbbob was a comparatively low-yield test series and since participation was limited to medium altitudes because of the topography of the Nevada Test Site (NTS), the response data obtained was limited to high-incidence angle and low-magnitude effects as reported in Reference 1. Project 5.3 of Operation Hardtack was specifically planned to extend the response investigations started during Operation Plumbbob to include lower incidence angles and higher magnitudes of effects; this will now permit a more reliable prediction of the escape criteria and delivery capability of the FJ-4B for high-yield weapons.

1.3 THEORY

Those phenomena which imposed critical limitations on positioning the FJ-4 aircraft were: (1) radiant exposure; (2) nuclear radiation; (3) overpressure; and (4) material velocity behind the shock wave.

It should be noted that the problems of establishing safe escape requirements for aircraft in the combat delivery of nuclear weapons are basically the same as the problems associated with the safe positioning of aircraft in nuclear tests, although the safety margins may differ.

1.3.1 Thermal Effects. During Operation Plumbbob, a maximum allowable temperature limit of 350° F for all structures in the FJ-4 aircraft was assumed. Upon the completion of active participation of FJ-4 aircraft in Operation Plumbbob, a critical review of the thermal-effects problem, and particularly the 350° F limit, was conducted by North American Aviation, Inc., (NAA), Columbus, Ohio. This review consisted of extensive laboratory testing of honeycomb-sandwich materials and analytical studies of conventional structure. This review resulted in raising the operational limit for conventional structure to 450° F and the limit for aluminum-bonded honeycomb-sandwich material to 400° F with a considerable safety margin before failure. This considerable safety margin available made practicable the establishment of a thin-skin limit of 500° F and a honeycomb limit of 450° F under the controlled conditions of the test operation.

Based on the fixed-temperature-limit concept, and because the temperature rises of both the conventional and honeycomb structures of the FJ-4 were similar in magnitude, both the aileron honeycomb panel and the 0.025-inch 7075 aluminum thin skin at Fuselage Station 390 were determined to be critical surfaces. The aileron panel is a $\frac{3}{16}$ -inch honeycomb sandwich with an outer skin of 0.016-inch 2024 aluminum and is a primary control surface. The 0.025-inch thin skin described above gave the combination of highest operating temperature and largest temperature rise. This was critical in many test conditions.

The thermal response of both types of surfaces could not be determined by a unified method, or by considering one surface as giving a fraction of the response of the other. This was because of the differences in the heat-sink capabilities. For this reason the thermal-effect problem was divided into two phases: radiant exposure and thermal response. The methods used for predicting the magnitudes of radiant exposure and temperature response in both honeycomb and conventional structures are presented in Appendix A.

1.3.2 Nuclear Radiation. The FJ-4 test aircraft restrictions, with respect to nuclear radiation, were on the basis of allowable personnel-dosage limits: 5 rem per event, not to exceed 15 rem over 3 consecutive months, and not to exceed 30 rem in a military career. For purposes of positioning, it was assumed that the cockpit did not provide any shielding for the pilot. The methods used to predict the total nuclear dose received at a point in space are described in Appendix B.

1.3.3 Overpressure Limitations. Studies conducted by NAA for Operation Plumbbob established the canopy as the critical structural component as far as overpressure and underpressure are concerned. The limits established in this study were +3.10 psig overpressure and -1.37 psig underpressure with the internal cockpit pressure limited to combat mission pressure of +2.75 psig maximum (Reference 1). Since it was planned to position the test aircraft for Operation Hardtack at higher overpressures than were experienced during Operation Plumbbob, a review of Operation Plumbbob overpressure limits was made. As a result of this review, a limit of 3.5 psi was authorized for field use. A detailed description of the equations used for overpressure calculations is presented in Appendix C.

1.3.4 Dynamic Response. A comprehensive study was carried out to determine the detailed motions of the FJ-4 aircraft in response to the symmetrical impingement of a high-intensity

blast wave. These motions included not only those of the aircraft in space, but also the transient vibratory motions of the structure. These latter motions served as a basic means of evaluating the stress levels existing throughout the airframe. A summary of the methods used in the establishment of the dynamic response is given in Appendix D.

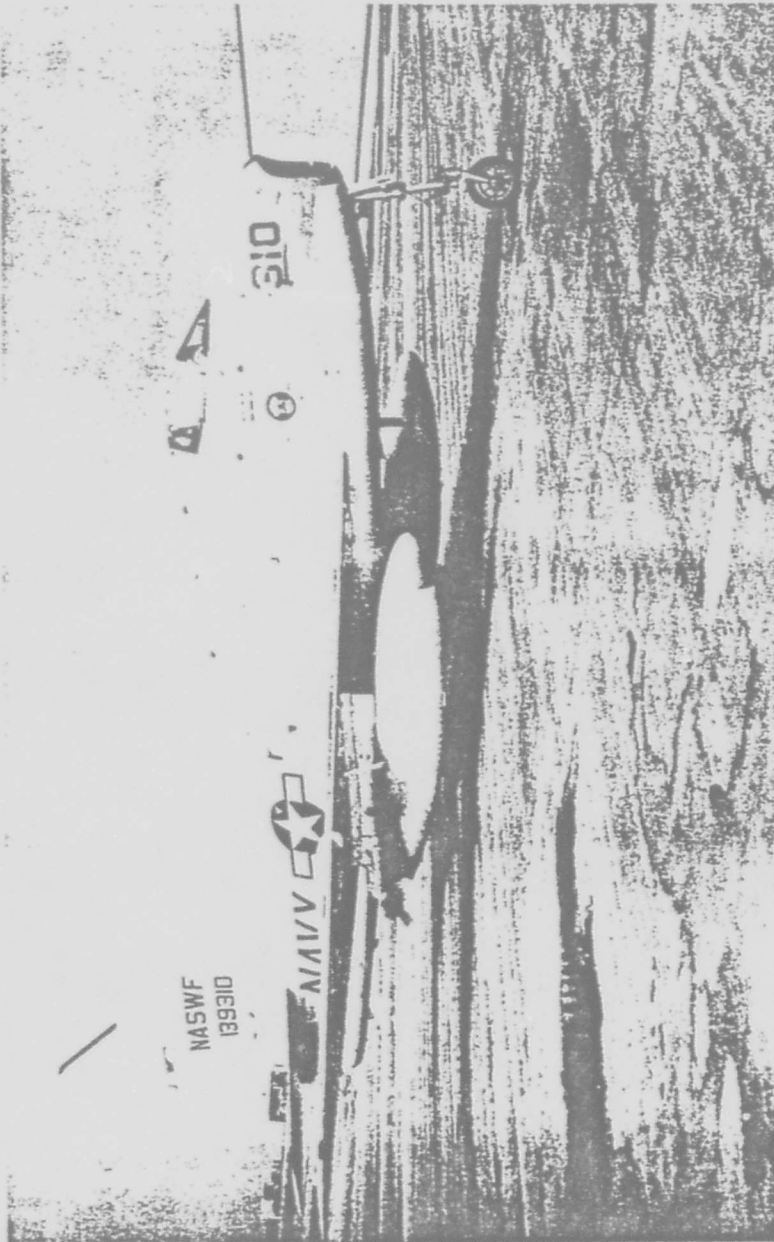


Figure 1.1 FJ-4 aircraft instrumented for Operation Hardtack.

Chapter 2

PROCEDURE

Two instrumented FJ-4 aircraft were provided to the Naval Air Special Weapons Facility (NASWF) for Operation Hardtack. The aircraft bore Bureau of Aeronautics Numbers 139310 and 139467. NAA supplied contract personnel, materials for the maintenance of test-aircraft instrumentation, and analytical effort for assurance of safe positioning, collection of significant data, data reduction, data analysis, and report writing.

2.1 OPERATIONS

Project 5.3 participated in eight shots: Cactus, Butternut, Koa, Yellowwood, Magnolia, Tobacco, Rose, and Walnut. Test-site activity, other than normal maintenance of the test aircraft and their instrumentation, consisted of establishing positions for each shot and the immediate reduction of data recorded. Analysis of the raw data from each shot was used in conjunction with existing methods to review the pretest positioning criteria. For all participations, to insure safety of aircraft and crew, positions were selected on the basis of a maximum possible yield for the device, termed "positioning yield."

The FJ-4 test aircraft were positioned by use of a modified M-33 gun-laying radar. This equipment utilized a plotting board with a pen recorder for tracking. The desired pattern was drawn to scale, and a controller compared the actual aircraft position with the desired position, and transmitted corrections to the pilot by ultra high frequency (UHF) radio. An electric pen recording system (Brush recorder) was installed to provide azimuth, range, and elevation for postshot positioning data. This recording system included a time-zero signal from a blue box circuit, which was activated by first light from the device, and continuous 1-second timing marks. Time of shock arrival used for postshot positioning data was obtained from instrumentation in the aircraft.

A typical FJ-4 participation flight consisted of takeoff at H-48 minutes, pattern entry at H-42 minutes, three orbits around a racetrack pattern approximately 7.6 nautical miles wide and 45 nautical miles long, a final run-in over surface zero from H-5 minutes, and landing at H+10 minutes (Figure 2.1).

2.2 INSTRUMENTATION

Instrumentation of the test aircraft provided for measurement of the following parameters versus time: (1) airspeed and altitude, (2) aircraft attitude and angular velocities, (3) control-surface positions, (4) engine temperatures and pressures, (5) temperature in critical skin panels, (6) wing bending and shear, (7) vertical-fin bending, (8) normal and lateral acceleration, (9) horizontal-stabilizer bending, (10) pressure distribution in the wing, and (11) explosion inputs—thermal, overpressure, and nuclear dose.

Thermocouples, radiometers, calorimeters, strain gages, flight-parameter instruments, and recording equipment were installed accordingly. A detailed description of the instrumentation used is contained in Appendix E.

2.3 DATA REQUIREMENTS AND REDUCTION

2.3.1 Requirements. The thermal parameters needed from the tests were: (1) time histories of irradiance and radiant exposure, and (2) temperature-time histories of critical skin panels on

the wings, flaps, elevator, and fuselage.

The nuclear-radiation parameters needed were: (1) gamma dose, measured with film badges at various locations in the aircraft, and (2) fast-neutron flux, measured by means of sulfur samples.

Free-stream peak-overpressure measurements were necessary for investigation of static-overpressure effects upon structure and for correlation with the calculated overpressures used in determining blast-wave parameters utilized in the dynamic-response analysis.

The structural-response parameters required from the tests were time histories of shear and bending-moment stresses in the wings and the horizontal stabilizer. The dynamic-response parameters, required for analysis and subsequent correlation of theoretical results, were: true airspeed, altitude, angle and rate of pitch, angle of attack, normal acceleration, control position of the elevator and horizontal stabilizer, and quantity of fuel remaining in the tanks.

The data required for the wing-overpressure survey was the variation of chordwise static-pressure distribution during impingement of the blast wave. These incremental pressure distributions were recorded at three spanwise stations on the left wing.

Miscellaneous parameters were recorded for a determination of pilot safety and for a study of weapon effects on engine operation. The following engine parameters were recorded versus time: (1) compressor total inlet pressure and temperature; (2) tailpipe total pressure and temperature; (3) compressor discharge pressure; (4) compressor compartment pressure; and (5) fuel-pump inlet pressure.

2.3.2 Reduction. Reduction of data from the calorimeters and radiometers was accomplished by personnel of the Naval Radiological Defense Laboratory (NRDL). All other data were reduced by contractor personnel.

2.3.3 Correlation. The two main items of interest in the correlation of thermal-effects data from all of the shots were measured radiant exposure and measured maximum temperature rise. Calculated and measured radiant exposures for all of the shots for both the normal and direct radiant-exposure positions were compared. Temperature data was recorded from thermocouples at four fuselage thin skins, two right outer-wing-panel thin skins, and the faceplates of three honeycomb control surfaces (elevator, aileron, and flap). The correlation presented the comparison of the measured temperature-rise data from the above thermocouple locations to three sets of calculated temperature-rise data. The three sets of calculated temperature-rise data were based on: (1) calculated radiant exposure, calculated flyaway factors (1-F), and the calculated combined flyaway and convective cooling factors (1-FH); (2) measured radiant exposure from the 160°-normal calorimeter, calculated (1-F), and calculated (1-FH); and (3) calculated temperature-time histories using measured irradiance from the 160°-normal radiometer.

The measured stability variables, which describe the rigid-body response, were compared directly with the corresponding values calculated by the methods of Appendix D. These variables, consisting of normal-load factor, angle of attack, pitch angle, and pitch rate, were prime factors contributing to the determination of stress levels existing throughout the airframe. This is because the longitudinal motions of the aircraft induce a significant portion of the aerodynamic wing loading.

Shear and bending-moment stresses, recorded by the wing strain gages, were compared with the corresponding values calculated from the dynamic-response analysis. These comparisons, in particular those for the bending-moment stress at the most critical station, Wing Station 17.5, were used to verify the positioning criteria during the test operation.

The dynamic-response analysis utilized a gust representation of the blast wave as the primary excitation function. To achieve a better knowledge of the actual loading, chordwise static-overpressure surveys were made at Wing Stations 82, 141, and 176. Time histories of overpressure, recorded by 14 pressure transducers installed along the chord, were cross-plotted at numerous points in time following arrival of the shock front. This was done at each of the three wing sta-

tions mentioned above. The resultant plots demonstrated the chordwise load distribution as a function of time after shock arrival, and were useful in analyzing the nature of the total load on the wing.

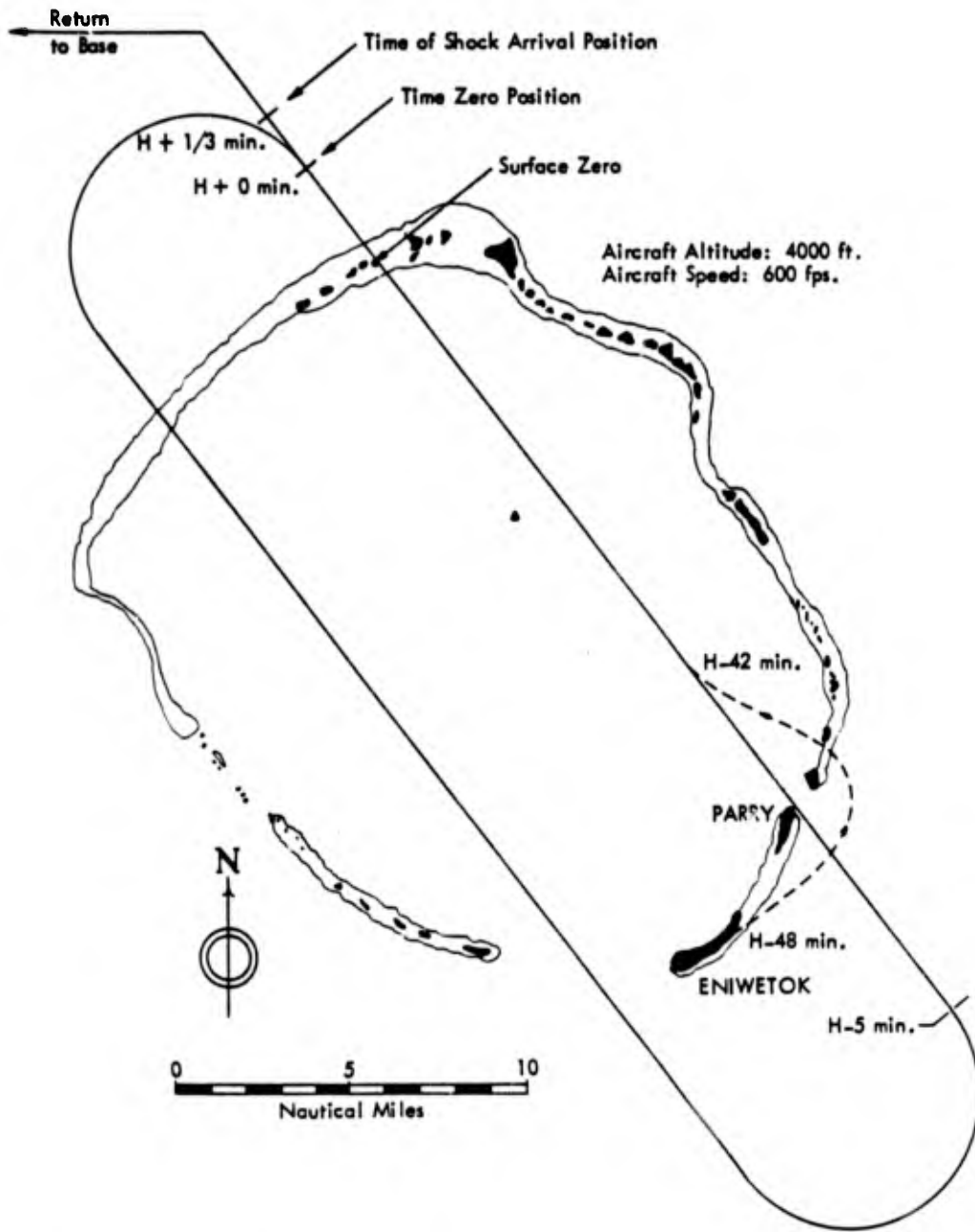


Figure 2.1 Typical FJ-4 test aircraft flight profile, Aircraft 139467, Shot Koa.

Chapter 3

RESULTS

Included in this chapter are: a summary of shot information; positions of the test aircraft for each shot; atmospheric and flight conditions; reduced weapon-effect data for each shot; and comparisons of calculated inputs and responses with observed phenomena. Table 3.1 gives a summary of the shot data. Table 3.2 shows the positions of the test aircraft at time of burst and time of shock arrival. Tables 3.3 and 3.4 provide data on the atmospheric and flight conditions at the time of shot.

3.1 RADIANT EXPOSURE

The measured data required for the analysis of radiant exposure consisted of time histories from calorimeters and radiometers aimed both normal to the under surface of the aircraft and directly at the fireball. Table 3.5 presents the data obtained from both the normal and direct calorimeter as well as some selected calculated values and the readings from the cockpit calorimeter. Figures 3.1, 3.2, 3.5, and 3.6 present the normalized irradiance curves, together with calculated curves, for both the normal and direct 160° radiometers on FJ-4 139310 for Shots Yellowwood and Walnut. These graphs also show the measured and calculated values of peak irradiance and time to peak irradiance. Figures 3.3, 3.4, 3.7, and 3.8 show the measured calorimeter, integrated measured radiometer, and calculated time histories for both the normal and direct instruments on FJ-4 139310 for Shots Yellowwood and Walnut. Additional radiant-exposure data for other than these typical shots are presented in Appendix F.

Figure 3.9 presents the comparison of the significant measured data with calculated effects. Discussion of these results is contained in Section 4.1.

3.2 THERMAL RESPONSE

The data utilized in the thermal-response analysis consisted of time histories of readings from the normal radiometer, the normal calorimeter, the direct 90° calorimeter, and the nine thermocouple locations discussed in Section 2.3.3. The thermal-response analysis and representative temperature-time history comparisons are presented in this section. Table 3.6 presents calculated and measured maximum temperature rises for the nine thermocouple locations for all flight participations during which the measured maximum temperature rises were greater than 10° F. Three values of maximum temperature rise were calculated for each of the nine thermocouple locations for those flight participations in which sufficient data for the five calculations were obtained. The three values of calculated maximum temperature rise are based on: (1) calculated radiant exposure, calculated flyaway factor (1-F), and calculated combined flyaway and convective cooling factor (1-FH); (2) measured radiant exposure from the normal 160° calorimeter, calculated (1-F), and calculated (1-FH); and (3) calculated temperature-time histories using measured irradiance from the normal 160° radiometer.

These three calculated values of maximum temperature rise are listed in Table 3.6 and, with the exception of data for Fuselage Station 210.81, are plotted versus measured maximum temperature rise in Figures 3.10 through 3.12 (Section 4.2).

Figures 3.13 through 3.16 present comparisons of calculated with measured temperature-time histories of the thin-skin thermocouple locations for FJ-4 139310, Shot Yellowwood. All

calculated data presented in temperature-time history comparisons are based on Method 3 of the methods of calculation listed above. Figures 3.17 through 3.19 compare calculated with measured temperature-time histories of the exposed faceplates of the aileron, flap, and elevator honeycomb panels for FJ-4 139310, Shot Yellowwood. Figures 3.20 through 3.23 compare calculated with measured temperature-time histories of the thin-skin thermocouple locations for FJ-4 139310, Shot Walnut. Figure 3.24 presents a comparison of calculated with measured temperature-time histories of the aileron honeycomb-panel faceplate for FJ-4 139310, Shot Walnut. Figures 3.25 and 3.26 present comparisons of calculated with measured temperature-time histories of the faceplates and backplates of the exposed flap and elevator honeycomb panels for FJ-4 139310, Shot Walnut. Figure 3.27 presents the measured temperature-time history of the top surface of the flap and elevator honeycomb panels for FJ-4 139310, Shot Walnut. Calculated and measured time histories of radiant exposure, generalized irradiance, and temperatures are presented in Appendix F for the flight participations listed in Table 3.6 (except for FJ-4 139310, Shots Yellowwood and Walnut).

3.3 THERMAL STRESS

A study was performed and comparisons between calculated and measured thermal stresses were made to investigate the feasibility of calculating thermal-stress increments from a given temperature distribution in the structure. The thermal strains and accompanying redistributed stresses were calculated by means of an IBM 704 program using the methods described in Section A.4.

The results given in Table 3.7 show a correlation between the measured-thermal-stress increments and the calculated-stress increments. The apparent large magnitude of difference between the calculated and measured thermal stresses is due to the fact that the measured thermal stresses were so low that the measurement and input errors in the analysis were of the same order of magnitude as the measured data.

3.4 NUCLEAR RADIATION

The nuclear radiation data obtained consisted of gamma-dose measurements from film badges and fast-neutron-flux measurements from sulfur samples. For the gamma-dose measurements, film badges were located in the aircraft as follows: the pilot wore three badges; three badges were located in a plastic box placed in the cockpit; and three badges were located in a plastic box placed in the ammunition bay. The badges worn by the pilot were randomly placed on his person for each mission. The badges in the boxes were oriented on three different planes with respect to the aircraft—horizontal, athwartships, and fore and aft. Measured gamma dose at these locations and calculated gamma dose based on postshot data are compared in Table 3.8.

Measurements of fast-neutron flux were obtained by placing 1-kg sulfur samples in the ammunition bay and cockpit areas for each shot. The samples were analyzed by the Research Directorate, Air Force Special Weapons Center (AFSWC). Fast-neutron-flux information was obtained from only three samples during the Cactus participation. The other samples were found to have contained a considerable amount of impurities so that determination of the fast-neutron activation was impossible.

3.5 FREE-STREAM PEAK OVERPRESSURE AND TIME OF SHOCK ARRIVAL

Free-stream overpressures were measured at stations on the nose boom and the left side of the fuselage of each aircraft. Maximum measured free-stream overpressures from these stations compared with calculated values are listed in Table 3.9. The measurements made at the nose boom are considered to be most representative of the free-stream overpressure because this location afforded the least amount of interference in the flow. The measured over-

pressures from both the nose-boom stations and the fuselage stations were reduced to correspond to a 1-kt burst in a homogeneous sea-level atmosphere by the use of the scaling equations outlined in Appendix C. These scaled values are shown in Figure 3.28 and Figure 3.29 respectively, for comparison with the free-stream overpressure versus slant-range curve (obtained from Reference 4) for a 1-kt burst in a homogeneous sea-level atmosphere.

The measured time-of-shock-arrival data is compared with calculated data in Table 3.9. The measured data were reduced to correspond to a 1-kt burst in a homogeneous sea-level atmosphere by use of the scaling equations outlined in Appendix C. Figure 3.30 shows these scaled values compared with values obtained from Reference 5 delineating time of shock-front arrival versus slant range for a 1-kt burst in a homogeneous sea-level atmosphere.

3.6 DYNAMIC RESPONSE

Basic flight parameters and representative stresses were measured during the test operation, to determine dynamic response of the aircraft to the blast wave. In addition, the blast-wave free-stream overpressure was measured as an initial means of determining the applied airloads which induce the response.

The values of free-stream peak overpressure behind the shock front (obtained from measurements on the nose boom of each aircraft) are shown in Table 3.9. The corresponding ratios of peak overpressure to ambient pressure at altitude at time of shock arrival are shown in Table 3.10. These ratios were used in computing other blast-wave parameters which were utilized in the dynamic-response analysis. The calculated blast-wave parameters are also shown in Table 3.10.

Table 3.11 itemizes the calculated and measured maximum values of the aircraft stability variables following impingement of the blast wave.

Table 3.12 presents both calculated and measured maximum perturbation values of wing bending-moment stresses, and Table 3.13 presents both calculated and measured maximum perturbation values of wing-shear stresses. The corresponding limit allowables and initial stress levels are also listed.

Figures 3.31 through 3.34 illustrate the dynamic response of the aircraft as a rigid body for the flight of FJ-4 139310 during Shot Magnolia. This response is described by the calculated and measured stability variables as perturbations about their corresponding values that existed prior to shock arrival.

Figures 3.35 through 3.49 illustrate the structural response of the wing for the same flight of FJ-4 139310. This response is described by the calculated and measured variations of shear and bending-moment stresses for selected points in the wing structure.

3.7 WING OVERPRESSURE SURVEY

The survey conducted during the test operation consisted of static overpressure measured at 14 points on the upper and lower surfaces of the chords at Wing Stations 82.2, 141.0 and 175.8. This data was recorded during and after arrival of the shock front.

Figure 3.50 illustrates the locations of all 14 pressure transducers for each of the 3 instrumented wing stations.

Figures 3.51 through 3.53 illustrate the chordwise incremental pressure distributions at intervals of time following shock arrival at the trailing edge of Wing Stations 82.2, 141.0 and 175.8, respectively, for FJ-4 139467, Shot Walnut. Similar data is presented in Figures 3.54 through 3.59 for FJ-4 139467, Shot Tobacco, and FJ-4 139310, Shot Butternut.

Integrated values of the pressure distributions in Figures 3.51 through 3.59 are presented as section-lift time histories in Figures 3.60 through 3.62.

Figure 3.63 illustrates the variation of the diffraction-pulse error function with blast-wave incidence. (The diffraction-pulse error function is the ratio of a theoretical peak-diffraction loading to the corresponding measured value.)

3.8 ENGINE RESPONSE

The J65-W-16A engines installed in the FJ-4 test aircraft were instrumented to obtain data on the response of jet engines to the thermal and blast effects. The operating parameters measured were throttle position, fuel flow, engine speed, compressor inlet and discharge pressures, fuel-system-supply pressure, and tailpipe temperature. The data evidenced similar responses for all shots. The data from Shot Koa, FJ-4 139310, was chosen as representative, and time histories of the operating parameters are shown in Figures 3.64 through 3.66. Time histories of indicated altitude, airspeed and outside-air temperature are also shown in Figure 3.67. Appendix G presents similar data recorded for the other participations.

TABLE 3.2 POSITIONS OF TEST AIRCRAFT AT TIME OF BURST AND TIME OF SHOCK ARRIVAL

Shot	At Time of Burst				At Time of Shock Arrival			
	Altitude Above Sea Level	Horizontal Range	Slant Range	Angle of Incidence Above Horizontal	Altitude Above Sea Level	Horizontal Range	Slant Range	Angle of Incidence Above Horizontal
	ft	ft	ft	deg	ft	ft	ft	deg
Cactus *	4,164	8,102	9,109	27.20	4,214	15,346	15,914	15.35
Cactus †	8,238	4,953	9,612	58.98	8,213	11,415	14,063	35.73
Butternut *	9,106	9,193	12,939	44.73	9,078	17,550	19,759	27.35
Butternut †	14,074	-6,677 †	15,578	64.62	14,014	1,187	14,064	85.15
Koa *	4,114	18,820	19,264	12.33	4,114	30,524	30,800	7.68
Koa †	16,018	17,899	24,020	41.83	15,978	32,682	36,379	26.05
Yellowwood *	3,937	22,130	22,477	10.08	4,044	40,566	40,767	5.70
Yellowwood †	13,060	16,316	20,999	38.67	13,043	39,213	41,325	18.40
Magnolia *	12,037	-5,354 †	13,174	66.02	12,108	-505 †	12,119	87.62
Magnolia †	10,027	3,600	10,654	70.25	10,127	9,075	13,598	48.13
Tobacco *	12,031	3,344	12,487	74.47	12,117	13,296	17,989	42.35
Tobacco †	9,082	8,331	12,324	47.47	9,005	18,234	20,336	26.28
Rose *	4,004	10,742	11,464	20.45	3,954	21,975	22,328	10.22
Rose †	13,059	2,554	13,306	78.93	13,055	12,615	18,154	45.98
Walnut *	3,996	15,855	16,351	14.15	4,054	24,880	25,208	9.25
Walnut †	10,809	12,798	16,752	40.18	10,730	24,726	26,954	23.47

* Aircraft 139467.

† Aircraft 139310.

‡ Short of surface zero.

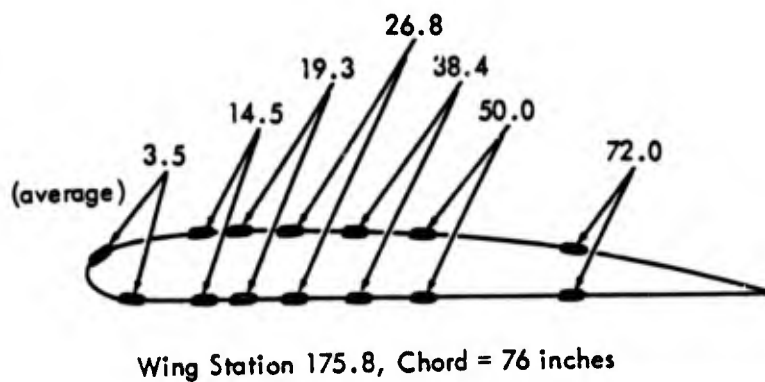
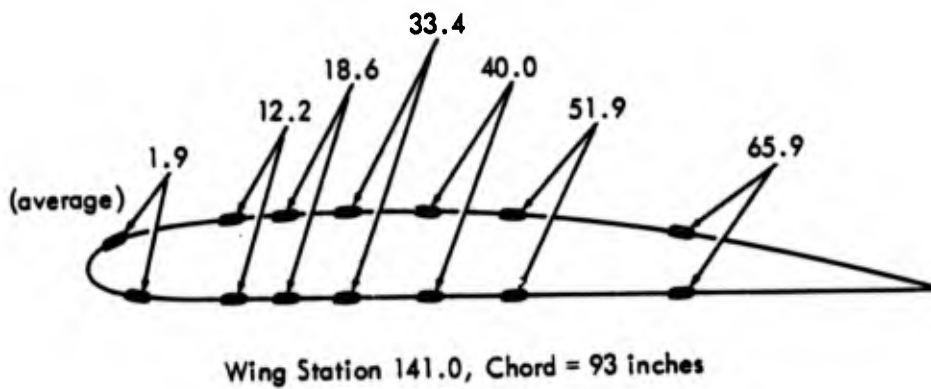
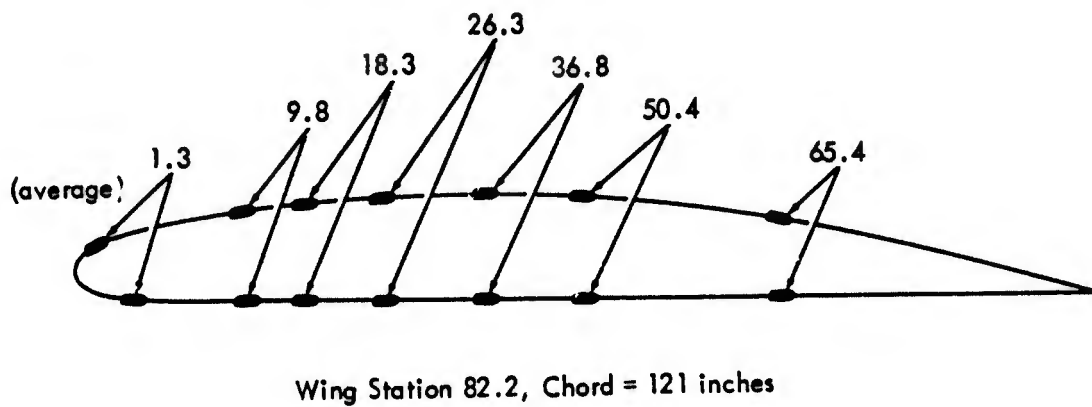
TABLE 3.4 FLIGHT CONDITIONS OF TEST AIRCRAFT AT TIME OF BURST AND TIME OF SHOCK ARRIVAL

NA, not available.

Shot	At Time of Burst				At Time of Shock Arrival			
	True Airspeed	Mach Number	Angle of Pitch, Nose Up	Angle of Attack, Nose Up	True Airspeed	Mach Number	Gross Weight	Angle of Attack, Nose Up
	ft/sec		deg	deg	ft/sec		lb	deg
Cactus *	583	0.519	7.99	NA	583	0.519	19,000	2.82
Cactus †	591	0.530	4.43	4.30	592	0.529	19,000	3.02
Butternut *	566	0.511	NA	NA	564	0.509	19,000	3.39
Butternut †	703	0.641	NA	4.50	706	0.645	19,000	2.50
Koa *	564	0.502	6.74	NA	564	0.502	19,000	3.00
Koa †	554	0.508	NA	5.00	547	0.501	19,000	4.37
Yellowwood *	583	0.519	4.34	NA	578	0.515	19,000	2.83
Yellowwood †	696	0.632	10.40	3.50	699	0.634	18,500	2.42
Magnolia *	579	0.525	5.40	4.00	578	0.524	19,500	3.63
Magnolia †	578	0.519	2.4	5.00	578	0.520	19,000	3.36
Tobacco *	638	0.578	NA	3.60	659	0.597	18,500	2.66
Tobacco †	574	0.515	2.95	3.80	578	0.519	18,500	3.17
Rose *	616	0.544	5.12	4.70	613	0.543	18,000	2.42
Rose †	674	0.614	2.64	3.90	672	0.611	18,000	2.56
Walnut *	578	0.514	7.50	2.00	567	0.506	18,500	2.72
Walnut †	659	0.598	2.70	4.20	655	0.594	18,000	2.53

* Aircraft 139467.

† Aircraft 139310.



All Transducer Locations Given in Units of Percent Chord

Figure 3.50 Pressure gage locations for the wing static-pressure survey.

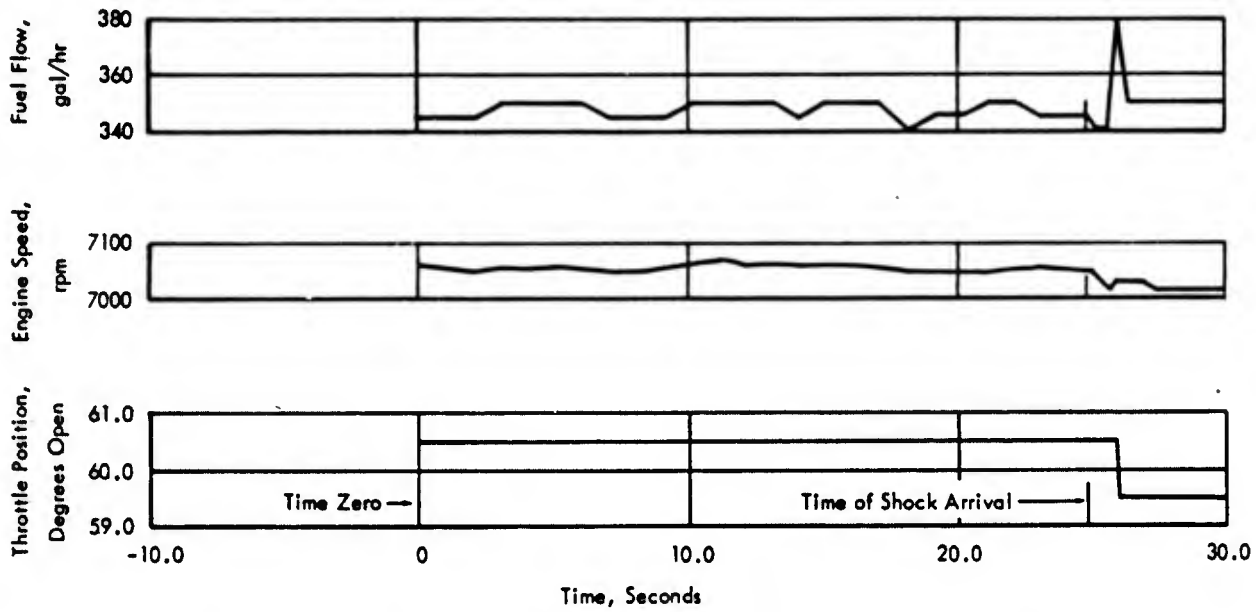


Figure 3.64 Throttle position, engine speed and fuel flow for Aircraft 139310, Shot Koa.

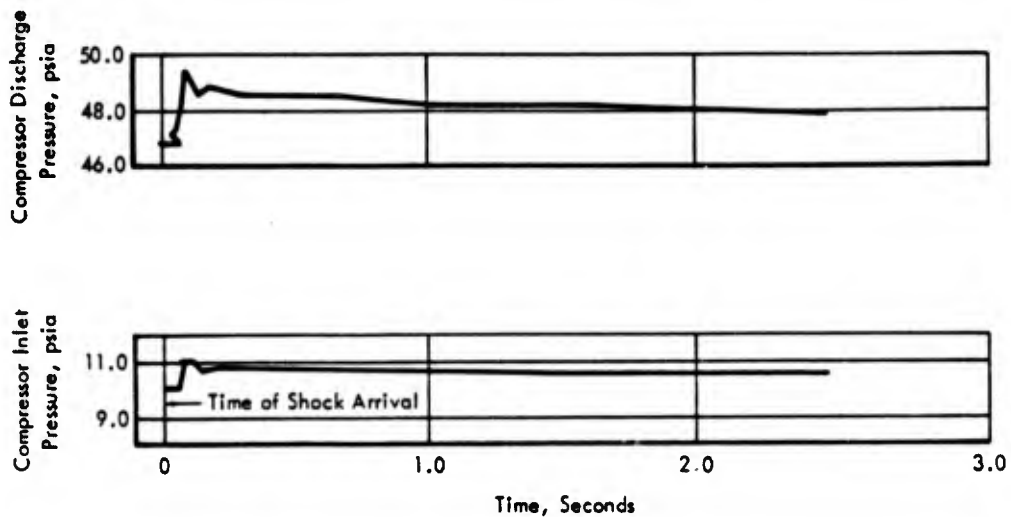


Figure 3.65 Compressor inlet and discharge pressures for Aircraft 139310, Shot Koa.

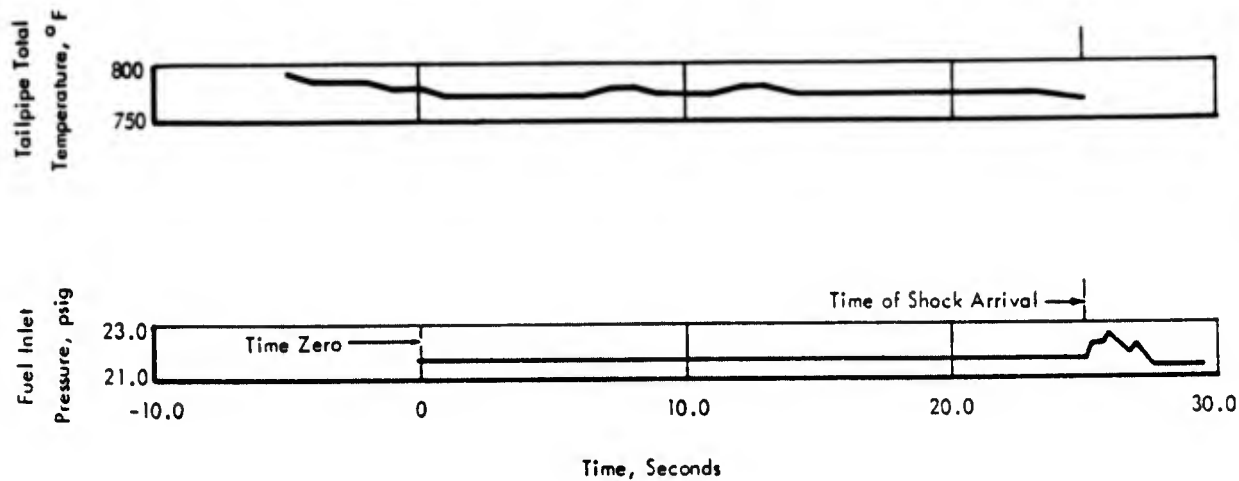


Figure 3.66 Fuel Inlet pressure and tailpipe total temperature for Aircraft 139310, Shot Koa.

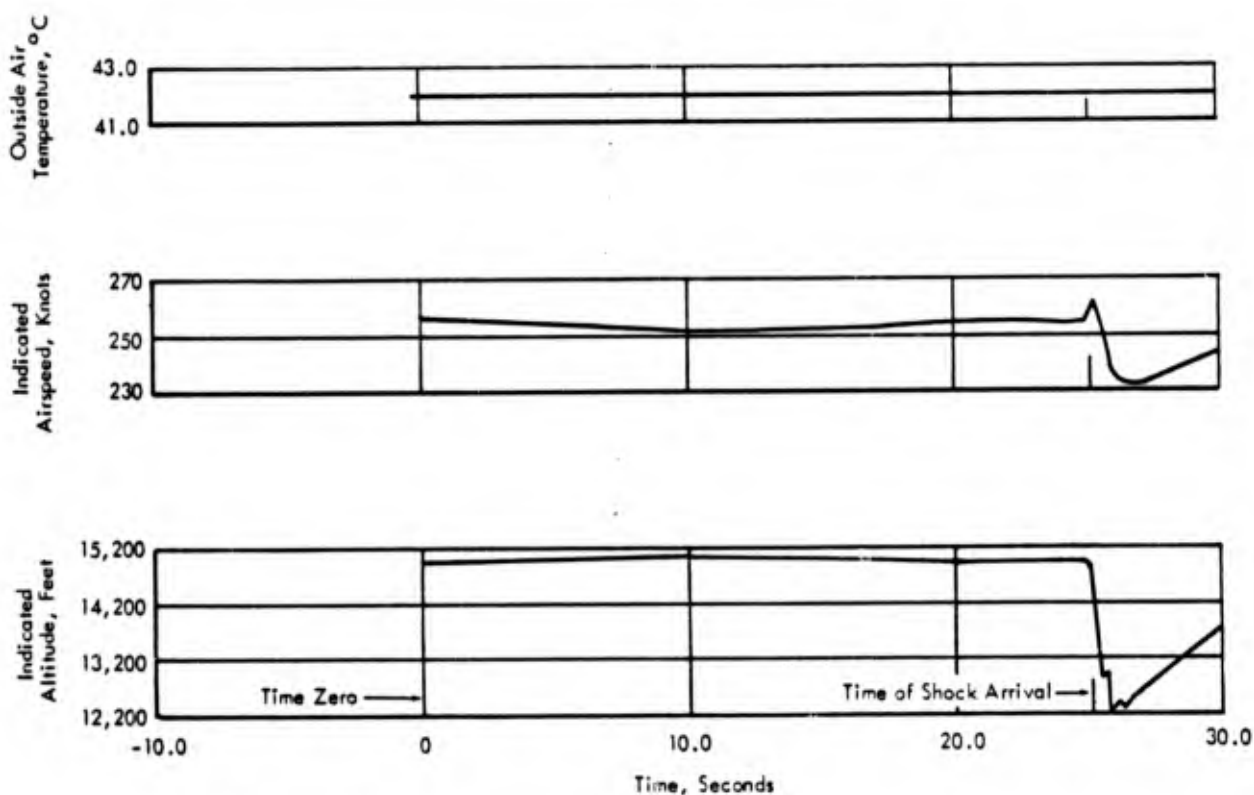


Figure 3.67 Indicated altitude, airspeed and outside-air temperature for Aircraft 139310, Shot Koa.

Chapter 4

DISCUSSION

4.1 RADIANT EXPOSURE

The data used in the analysis of radiant-exposure phenomena was obtained from calorimeters and radiometers supplied by NRDL. These data consisted of time histories of: (1) radiant exposure and irradiance normal to the planform of the aircraft as observed by a 160°-field-of-view calorimeter and a 160° radiometer located in the ammunition bay; (2) radiant exposure and irradiance as viewed by a 160°-field-of-view calorimeter, a 160° radiometer, and a 90° calorimeter aimed directly at the fireball, all located in the aft end of the instrumented wing tank; and (3) radiant exposure in the cockpit as viewed by a 90° calorimeter mounted forward of the glareshield and facing to the right. The data from these instruments, together with selected comparisons to predicted values, are presented in both tabular and graphical form in Chapter 3 and Appendix F.

The following sections present an examination of thermal characteristics and data for each of the events in which FJ-4 aircraft participated, as well as a discussion of the overall significance and correlation of the radiant-exposure data obtained.

Shot Cactus was a low-yield, 17-kt event, used primarily for pilot orientation. The radiant-exposure data obtained was of very low magnitude, 2 cal/cm² and less, and the shot was heavily shielded. Before it was known that shielding was used, the in-field calculations predicted effects an order of magnitude higher than were experienced. Because the effects of mass (shielding) on either total-energy emission or the emission spectrum of a device cannot be predicted by the techniques employed in this report, no attempt was made to correlate the radiant-exposure data from this shot.

Shot Butternut was a _____ barge shot, and was the first event in which the project planned to obtain large-magnitude data. However, the aircraft were positioned primarily for the acquisition of gust-load and dynamic-response information.

One of the characteristics of barge shots is the use of an 18-inch-thick, 6-foot-high concrete shield positioned in a semicircle around the device. In the past, the mass effect of this shield has been negligible, but only because the yields of previous barge shots have been large (the lowest yield having been _____). However, for

Shot Butternut, this mass is felt to be quite significant. This conclusion is based on the fact that the normalized pulses for Shot Butternut (Appendix F) display the long time to peak irradiance and slow decay characteristic of shielded shots. For this reason, the data from Shot Butternut should be treated with caution if used for evaluation of operational or positioning prediction techniques.

Shot Koa was a _____ land shot; however, the device was positioned at the bottom-center of a 20-foot-diameter, 22-foot-high water tank. Although the recordings obtained from both aircraft were of reasonable magnitude, the radical alteration of the spectral properties of the energy emission induced by the water shielding precludes all analysis of thermal effects, especially radiant exposure.

Although Shot Yellowwood detonated at approximately _____ the data obtained by FJ-4 139310 was of sufficient magnitude for accurate correlation. The data from FJ-4 139467, however, was too low to read off the oscillographs.

The normalized pulses presented in Figures 3.1 and 3.2 show slight effects from the concrete shielding, but much less pronounced than were evidenced in Shot Butternut or in the subsequent shot, Magnolia.

Shot Magnolia was a large shot that displayed the same characteristics as Shot Butternut with regard to the effects of the concrete shield surrounding the device. Magnolia data and comparisons with predicted values have been presented in Chapter 3; however, the data should be treated with the same caution as Butternut data.

Shot Tobacco was evidenced. Consequently, the aircraft were positioned at too great a range for significant effects, and no attempt was made to correlate the fractional calorie readings for this shot.

Shot Rose

Again the aircraft received only fractional caloric inputs for which no correlation was accomplished.

Shot Walnut

Heavy cloud cover near the surface, and the fact that the fireball was out of the field of view of the normal 160° instruments, precluded any valid correlation of the data obtained by the low-altitude aircraft, FJ-4 139467. The high-altitude aircraft, however, made a fully successful participation and obtained usable data.

Table 3.5 presents all of the measured data obtained for radiant-exposure correlation as well as calculated values for the significant events. The comparison of these measured values with calculated values (Figure 3.9) shows reasonably good agreement; however, NRDL has advised that the reliability of all instruments is only ± 10 percent when unduplicated, and also that the calibration of the 160°-field-of-view instruments is very questionable when the angle of incidence of the flux to the button is appreciably different from normal.

Included in Table 3.5 are readings from a 90° calorimeter that was mounted inside the cockpit to measure scattered and reflected radiant exposure received inside the canopy. These values show very low magnitude effects in general. However, the data was collected in the absence of heavy cloud cover or heavy precipitation; therefore, the low magnitudes observed are not necessarily indicative of extreme conditions that may arise in more adverse situations.

Most of the data acquired could be considered to be unreliable and/or undesirable due to several deficiencies in the experimental procedure: (1) the lack of duplicate instruments, (2) the use of 160°-field-of-view instruments whose calibration reliability was questionable, and (3) the lack of information on shielding at the time of selection of shots in which to participate. These same deficiencies were also evidenced during Operation Plumbbob and particularly concerned Shots Kepler, Shasta, Diablo, and Smoky. In addition, because of the physical locations of the calorimeters and radiometers on the FJ-4 aircraft, their forward portions became coated with runway dust during takeoff. For fly-into positioning, the radiant exposure received was attenuated by this dust coating. This effect was particularly noted on Shots Boltzmann, Hood, and Doppler in Operation Plumbbob and on Shots Butternut and Magnolia in Operation Hardtack.

Even though much of the radiant-exposure data obtained in both Operations Hardtack and Plumbbob may be subject to question because of various experimental errors, some of the data is particularly worthwhile. First, the Walnut participation provided a

Second, Yellowwood gave excellent data for a hazeless Pacific atmosphere. Finally, the remaining data, from Shots Butternut and Magnolia, demonstrated, by observation of the time histories of the thermal emission, the effect of even small amounts of mass on low-yield devices. Thus, for operational situations, shielding by ground structures should provide an additional margin of safety for the escape of the delivering aircraft if the prediction techniques do not account for shielding.

4.2 THERMAL RESPONSE

A wide range of maximum temperature rise was experienced by the aircraft structures during the tests. In general, however, the maximum temperature rises were low (less than 100° F)

with the exception of the participation of FJ-4 139310 in Shot Walnut, during which maximum temperature rises ranged from _____ No thermal-response analysis was attempted for flight participations during which maximum temperature rises were less than 10° F. These flight participations were: (1) FJ-4 139310, Shot Cactus; (2) FJ-4 139467, Shot Cactus; (3) FJ-4 139467, Shot Yellowwood; (4) FJ-4 139310, Shot Rose; (5) FJ-4 139467, Shot Rose; (6) FJ-4 139310, Shot Tobacco; and (7) FJ-4 139467, Shot Tobacco.

Paint history: Painted 12 March 1957; wash primer MIL-C-8514; lacquer primer MIL-P-7962; gray lacquer MIL-L-19538; white lacquer MIL-L-19537.

The thermal-response analysis consisted of comparisons of calculated with measured maximum temperature rises and temperature-time histories for both thin-skin and honeycomb-panel faceplate thermocouple locations. Three independent values of maximum temperature rise were calculated for each thermocouple location, using the methods outlined in Appendix A. The description of the three values and the flight participations for which they were calculated is presented in Section 3.2. These values of maximum temperature rise were not calculated for the following participations: (1) FJ-4 139310, Shot Koa (because of very low deflections of the normal 160° radiometer); (2) FJ-4 139467, Shot Koa; and (3) FJ-4 139467, Shot Walnut (because of the low angles of incidence, the fireball was out of the field of view of the normal 160° calorimeter and radiometer).

The factors used in the thermal-response analysis, with the exception of the skin-absorption coefficients (Table 3.6), were computed by the methods presented in Appendix A. Because the effect of the mass of the paint on the external surfaces was found to be appreciable in the consideration of heat-sink properties, it was incorporated in the equation for the calculation of the thin-skin and honeycomb-faceplate heat capacities. The heat-capacity equation is given in Section A.3.2 for thin skins and in Section A.3.4 for honeycomb faceplates. The heat capacities used in the thermal-response analysis are given in Tables A.2 and A.4 respectively. Since the comparison of calculated with apparent turbulent-heat-transfer-convection coefficients in Operation Plumbbob (Reference 1) was satisfactory, calculated values were used throughout the thermal-response analysis. The method of calculating the heat-transfer coefficients is given in A.3.6. Based on the discussion in Section 4.1 on radiant-exposure-data correlation, the flyaway factor (1-F) and the combined flyaway and convective cooling factor (1-FH) were computed based on the infinite time scale and were used throughout the thin-skin thermal-response analysis. The methods for computing these factors are given in Equations A.2 and A.8. The values used are presented in Tables A.1 and A.3. The complex derivation of the honeycomb thermal-response prediction method is based on radiant exposure and (1-F) values at ten times the time to maximum irradiance, 10η . The effort required to modify this method to incorporate the infinite time scale was considered unjustified. Therefore, the flyaway factor, cooling factor, and radiant exposure values at 10η were used in the honeycomb thermal-response analysis.

The maximum temperature rises for Fuselage Station 210.81 and the aileron honeycomb faceplate should be nearly equal to that for Fuselage Station 248.155 and the flap honeycomb faceplate, respectively, since the thermal properties and physical dimensions (excluding characteristic length) are identical. However, a consistent discrepancy in the thermal-response data for the former two thermocouple locations is noted in Table 3.6. An investigation of the physical and thermal characteristics of Fuselage Station 210.81 and the aileron honeycomb faceplate thermocouple locations failed to reveal any reasons for the discrepancies. Since the discrepancy in the maximum temperature rise of Fuselage Station 210.81 was unreasonably large, it was assumed that the measured data for this location was in error, and therefore it was omitted from the data comparison in Figures 3.11 through 3.13.

Figure 3.10 presents the comparison of measured with calculated maximum temperature rises of selected thermocouple locations using calculated radiant exposure, calculated (1-F) and calculated (1-FH). Reasonable agreement is shown, considering the many variables involved. Figures 3.11 through 3.13 serve as a reliability check on radiant-exposure and irradiance instrumentation and as a comparison of measured to calculated thermal-response data using measured radiant exposure and irradiance. In general, this data shows acceptable agreement between calculated and measured thermal response.

The temperature-time histories of selected thermocouple locations were computed using the measured irradiance from the normal 160° radiometer. These calculated temperature-time histories are compared with measured temperature-time histories in Chapter 3 and Appendix F. In general, the temperature-time history comparisons are quite satisfactory; however, the times of peak temperature of the calculated temperature-time histories are generally greater than the measured times to peak temperature. It is observed that the measured time to maximum irradiance is generally greater than the calculated time to maximum irradiance. This could be attributed to instrumentation lag. Since the comparison of times to peak temperature is improved if the calculated time to maximum irradiance is used, the time lag in the radiometer data is quite possible.

In general, it is concluded that the acceptable agreement with calculated results evidenced by the significant thermal-response data obtained in Operation Hardtack substantiates the reliability and accuracy of the combined radiant-exposure and thermal-response prediction methods presented in Appendix A.

4.3 THERMAL STRESSES

Comparisons between calculated and measured thermal stresses were made to investigate the feasibility of calculating thermal-stress increments from a given temperature distribution in the structure. The method of measurement and the type of analysis used were chosen to eliminate as many variables as possible. The measured thermal-stress increment was obtained from flight-test data by using the increment in stress readings from the trim condition just prior to each shot to the temperature peak following each shot. Since all structural-element stresses were below the proportional limit and since the principle of super-position holds, thermal effects were considered in the analysis without the effect of flight loads.

The methods used for calculating the thermal-stress increments are presented in Section A.4. Thermal-stress analysis was programmed for an IBM 704 digital computer. By an iterative procedure in this program, the correct modulus of elasticity, the total strain, and the buckling allowable (or effective area) for an element were chosen using the correct temperature, the final stress, and the panel configuration for that element.

The method of analysis included the secondary effects of unequal temperatures and the accompanying unequal thermal expansions, which are: (1) bending in the spanwise and chordwise directions, and (2) loads induced in redundant load paths through several interconnected parts of the structure. For the particular structure used in this study, the bending effects on the thermal-stress increment were of the same magnitude as the final thermal-stress increment. The redundant load effects on the thermal-stress increment were one-fourth to one-tenth the value of the final stress increment.

Three conditions caused uncertainties in the calculated thermal-stress increments: (1) Actual structural-element dimensions differ from nominal dimensions by normal production tolerances so that the actual section properties may be different from the nominal section properties used in the analysis. (2) Structural temperatures over some areas of the structure were not measured, thus estimated temperatures were used in these areas for the analysis. Thermal stresses are quite sensitive (135 psi/°F) to variations in the structural temperature. (3) Mechanical free play in redundant structural load paths tends to relieve thermal strains. Uncertainties concerning the amount of mechanical free play prevent its inclusion in the analysis of thermal stresses.

There were two conditions causing uncertainties in the measured thermal-stress increments: (1) measurement sensitivity or uncertainty (50 to 100 psi, including instrument and reading errors) is approximately of the same order of magnitude as the measured thermal-stress increment; and (2) local gusts over the 4-second interval between measurements cause load changes that cannot be predicted and were not measured in the test.

The flight-test measurements were made by electrical wire resistance strain gages. The horizontal-stabilizer, rear-beam Station 33 bending strain gages, left side (No. 1463) and right side (No. 1464) were used to determine measured thermal-stress increments. (Reference 6 gives the calibration factor.) Locations of these gages are given in Appendix E, Figure E.1. The gages at each location are connected to measure average bending stress, i. e., $\frac{1}{2}(\sigma_{\text{upper}} - \sigma_{\text{lower}})$. The horizontal stabilizer was chosen for correlation because this structure had the highest temperature differential, and therefore the highest thermal stresses (due to the fact that it had thinner skins than any other appropriately instrumented section).

Thermal-stress calculations were made for those shots representing the highest magnitude of radiant-exposure values received by the aircraft

Comparison of calculated with measured thermal-stress increments was accomplished using the calculated-stress increments for the upper and lower beam caps to calculate the average bending stress. These results are compared in Table 3.7. The difference between measured and calculated data is within the expected realm of accuracy, considering the fact that the measured stresses were so low that the measurement and input errors in the analysis were of the same order of magnitude as the measured data. Thus, it is not possible to draw any conclusions from the thermal-stress data obtained.

4.4 NUCLEAR RADIATION

Measured values of gamma-radiation dose are compared with calculated values in Table 3.8. The calculated values were determined by the methods of Appendix B. The values measured in the cockpit and on the pilot's person were significantly lower than those measured in the ammunition bay. This indicates that a significant amount of shielding was afforded the pilot by the aircraft structure.

As shown in Table 3.8, there was considerable scatter in the measured values. For measured values less than 1 r there was poor correlation and, in general, the measured values were somewhat higher than the calculated values. For measured values greater than 1 r the correlation was somewhat better and, in general, only the values from the ammunition bay were unconservative.

Fast-neutron-flux measurements and calculations are also shown in Table 3.8. The measurements were made with 1-kg sulfur samples placed in the cockpit and ammunition bay. The neutron-flux measurements were made primarily as an experimental program to determine the suitability of using sulfur to measure very low levels of fast-neutron flux. The results show that this technique may be used successfully under field-test conditions. Unfortunately, one batch of sulfur samples contained a considerable amount of impurities so that determination of the fast-neutron activation was impossible. Consequently, only three measurements were obtained, all for Shot Cactus.

Because of the very low readings, the results are not accurate enough to determine the relative fast-neutron flux between the cockpit and the ammunition bay with any degree of reliability. The one reliable set of measurements obtained for both areas indicates that the flux in the cockpit area was approximately 40 percent less than in the ammunition-bay area.

4.5 PEAK FREE-STREAM OVERPRESSURE AND TIME OF SHOCK ARRIVAL

Peak free-stream overpressures were measured at locations on the nose boom and the left side of the fuselage of each aircraft. The measured values were compared with calculated values in Table 3.9.

The values measured at the fuselage were consistently higher than those measured at the nose boom. The measurements made at the nose boom are considered to be most representative of the free-stream overpressure, because this location afforded the least amount of interference in the flow.

Using after-the-fact positions of the aircraft, atmospheric conditions at time of shock arrival, and final yields, the measurements from the nose boom and fuselage locations were reduced to correspond to a 1-kt burst in a homogeneous sea-level atmosphere by the scaling equations of Appendix C. These data are compared in Figures 3.29 and 3.30 with the curve of peak free-stream overpressure versus slant range obtained from Reference 4. The reduced measured values from the nose boom are slightly lower than the basic curve for overpressures less than 2 psi. The reduced fuselage-overpressure data for FJ-4 139310 agrees with both the basic curve and the nose-boom data quite well. However, the reduced fuselage-overpressure data for FJ-4 139467 is consistently higher than both the nose-boom data and the basic curve. No explanation for this apparent discrepancy is available.

The data from Operation Hardtack complements the data obtained during Operation Plumbob in that it significantly extends the range over which data was obtained in that operation (Reference 1).

Since the highest measured nose-boom and fuselage overpressures were respectively, compared to the positioning limit of 3.5 psi, no damage from free-stream overpressure effects occurred to the aircraft.

Measured values of time of shock-front arrival are compared in Table 3.9 with corresponding values calculated by Equation C.8. Excellent correlation is shown, with an average deviation from measured values of only 2 percent. The measured values were reduced to correspond to a 1-kt burst in a homogeneous sea-level atmosphere by use of the scaling equations of Appen-

dix C. The reduced values are plotted in Figure 3.30 in comparison with the basic curve (from Reference 5) for a 1-kt burst in a sea-level homogeneous atmosphere. Good correlation is shown, with the measured values only slightly lower than the basic curve.

4.6 DYNAMIC RESPONSE

The dynamic response of the aircraft was of relatively high frequency with respect to the positive phase of the blast wave. Subsequent to blast-wave impingement, an initial positive acceleration, normal to the flight path, and coincident with a nose-down pitching motion, was experienced. The aircraft recovered from this disturbance in a conventional highly damped, short-period, pitching-plunging motion. These rigid-body motions occurred in conjunction with a high level of vibratory structural deformation of the airframe. The resulting dynamic stresses were characterized by very high frequencies with respect to the rigid-body short-period motions. A discussion of these response characteristics is presented in the following paragraphs for both the measured and calculated data of the FJ-4 aircraft participating in Operation Hardtack.

4.6.1 Measured Response. The measured data that described the dynamic response of the aircraft to the blast wave was both reliable and consistent. The reliability of this data may best be demonstrated by the fact that from the 18 recording channels required for adequate analysis of the longitudinal response on 16 flights, only eight traces were considered to be unusable. These figures imply a reliability factor of 97 percent. The consistency of both the rigid-body and structural motions, as recorded for each shot, appear to be very good. Because of this consistency of measured data, the following discussions will deal primarily with the dynamic response of FJ-4 139310 to Shot Magnolia as typical.

4.6.2 Calculated Response. The calculated dynamic-response data presented in Chapter 3 was determined by the method of Appendix D. The atmospheric and flight conditions that determined the parametric values for the analysis were those measured at the time of each flight and presented in Tables 3.3 and 3.4. These measured conditions were used in an attempt to simulate as accurately as possible the response characteristics of the aircraft for each flight. The blast-wave parameters that were used in the response analysis were computed by the methods described in Appendix C from the measured peak free-stream, nose-boom overpressures of Table 3.9.

4.6.3 Correlation of Maximum Responses. The calculated and measured maximum values of the aircraft stability variables after shock arrival are presented in Table 3.11 for all events. The consistency of relative magnitudes between the calculated and measured values for each event is very apparent. Normal-load factor (a direct indication of the blast-wave gust effect) and the perturbation angles of attack and pitch (which indicate the amplitude of rigid-body response) should be associated with the blast-incidence angle and measured (nose-boom) peak overpressure of Tables 3.2 and 3.9, respectively. This comparison indicates that the blast-wave gust effect and rigid-body response are both very nearly proportional to peak overpressure and blast angle.

The relatively high peak overpressure and low blast-incidence angle for the flight of FJ-4 139467 in Shot Walnut introduce a significant nonlinear effect. This nonlinearity is due to an alleviation of airload by the reduction of local dynamic pressure. It is the component of material velocity along the flight path that reduces the resultant airspeed and consequently lowers the dynamic pressure. This load alleviation at low incidence angles is of extreme importance to the establishment of the aircraft's delivery capabilities.

There is a slight degree of inaccuracy inherent in the determination of the peak values of measured normal-load factor as presented in Table 3.11. This recognized deficiency is attributed to the local structural accelerations which were superimposed on the conventional normal-

load factor of the rigid aircraft. These high-order oscillations are illustrated in Figure 3.31. To establish the maximum value of the rigid-aircraft normal-load factor presented in Table 3.11 it was necessary to fair out the local structural effects.

Maximum bending-moment and shear-stress levels, as measured in the wing during the test operation, are listed in Tables 3.12 and 3.13, respectively, with the corresponding values from the theoretical analysis. Although the consistency of relative magnitudes between the calculated and measured values for each event is apparent, there are discrepancies between the computed and measured absolute magnitudes of stress for approximately half of the recorded stresses. The computation of the peak stresses is dependent on the stress distributions associated with each normal mode. These stress distributions are necessary to establish the modal stresses that are used in conjunction with the normal coordinates of the structure to compute the actual stresses throughout the airframe. Because the wing structure is so complex, and the inertial spanwise loading associated with each mode is so discontinuous, it was concluded that an experimental evaluation of the modal stresses would be more accurate and expedient than a theoretical approach. Consequently, a ground-vibration test was conducted on FJ-4 139310 after the test operation to reestablish the normal aircraft modes and to measure the associated modal stresses for the wing. The unconservative values in approximately half the calculated stresses (Tables 3.12 and 3.13) have been attributed to the malfunctioning of the gages subsequent to the rigors encountered during transportation back from the Eniwetok Proving Ground.

As shown in Table 3.12, the most critical portion of the airframe is located at Wing Station 17.5. The stress level at this point is due to bending moment in the wing carry-through structure, which is initially a direct result of the total wing loading. Since the total wing loading directly determines this stress by its integrated value of bending moment, and since the straight-forward design of the carry-through structure lends itself easily to theoretical stress analysis, the modal stress at Wing Station 17.5 may be computed with a high degree of accuracy. Therefore, a calculated value of modal stress was utilized in computing the perturbation stresses of the carry-through structure. The peak stress level at this location occurs at approximately $\frac{1}{10}$ second after shock arrival, coincident with the occurrence of maximum normal-load factor.

The bending-moment stress was measured at Wing Station 17.5 on both the right and left wings. This duplication of gages was made to insure the accuracy of this most critical stress. The average variation from the mean measured stress between the right and left wings was 6.02 percent of the mean measured stress (Table 3.12). This good correlation proves the validity of measured stress levels at this structural point.

Comparison of the calculated stresses with the respective measured values at Wing Station 17.5, demonstrates the high degree of capability of the theoretical analysis to predict this most critical blast-induced stress in the FJ-4 aircraft. The average difference between the mean measured stress and the corresponding calculated value was only 5.88 percent of the mean measured stress.

The horizontal stabilizer stresses recorded during the test operation were found to be much less critical than those of the wing. This characteristic may be attributed to two separate factors. The first factor is that pitching motion of the aircraft has a large aerodynamic alleviating effect on the tail surfaces. As seen by the values of pitch rate in Table 3.11, pitching motion is a characteristic of the aircraft response, and therefore this alleviating effect is significant. The second factor is the difference of the design requirements for the two surfaces. On the FJ-4 aircraft, the horizontal stabilizer was designed on the basis of combined strength and flutter requirements, whereas the wing was designed primarily on the basis of strength requirements. As a result, the tail possesses basically higher strength than the wing, and the percent of allowable stress levels, under similar loading, tend to be lower.

4.6.4 Rigid-Aircraft Response. As the wave front rapidly envelopes the aircraft, the lifting surfaces experience an increased aerodynamic loading because of the material velocity behind the shock front. These transient aerodynamic loads result in a combined plunging and pitching motion of the aircraft. These motions may be characterized by an increased normal-load factor

and a buildup of negative pitch rate. After these parameters have reached their maximum values in response to the gustlike blast wave, the aircraft experiences a highly damped short-period oscillation about the trimmed flight conditions existing prior to shock arrival.

The variation of normal-load factor, as illustrated by Figure 3.31 for FJ-4 139310 during Shot Magnolia, was recorded by two linear accelerometers. These accelerometers were installed in the fuselage at the aircraft center of gravity and near the wheel-well of the wing. The installation in the wing was made in an attempt to eliminate the accelerations caused by structural vibrations. Because of these structural effects, it was difficult to correlate the maximum measured normal acceleration with the corresponding value obtained from the dynamic-response analysis. The wing accelerometer was partially effective in eliminating the local effects but still required fairing to obtain an effective measurement of rigid-aircraft normal-load factor.

The pitching motion of the aircraft caused by the induced loads of the blast wave is illustrated by Figures 3.33 and 3.34. Predictions of the maximum values of both pitch rate and perturbation angle of pitch are in good agreement with the respective measured values. The pitching frequency during the early portion of the response is directly dependent on the nature of the material velocity behind the shock front. The response characteristics associated with this frequency appear to be in good agreement with the in-flight data.

The aircraft angle of attack, as illustrated by Figure 3.32, was based on measurements obtained from free-stream vanes mounted on the forward end of a relatively long nose boom. The recorded signals consisted of aircraft angle of attack caused by plunging, angle of attack caused by the blast wave, and a vibratory signal caused by the structural response of the nose boom. Figure 3.32 presents the plunging portion of the measured signal, to permit comparison with the calculated angle of attack. Isolation of the plunging component was facilitated by fairing out the vibratory nose-boom signal and subtracting the calculated blast-wave component. The computation of the induced angle of attack associated with the blast wave was based on the measured value of peak overpressure from the nose boom.

The positions of all the longitudinal control surfaces were recorded on each flight to detect any extraneous inputs due to pilot reaction. Only the horizontal stabilizer showed measurable control-surface displacements. The aerodynamic loads due to these small displacements of the stabilizer were found to be negligible.

4.6.5 Wing Structural Response. As the blast wave sweeps across the wing, a substantial increase in static and dynamic pressure is experienced on the underside of the lifting surface. This abrupt, increased loading tends to excite the normal vibration modes of the aircraft. These normal modes are seen as complex deformations of the structure vibrating at relatively high frequencies. These motions served as the basic means of evaluating the stress levels existing throughout the structure following blast impingement.

The most critical wing stress experienced by the FJ-4 aircraft was at Wing Station 17.5 of the carry-through structure. Failure at this location would be indicated by compression in the upper member of the boxlike structure, caused by the accumulated bending moment from the normal wing loading. The variation of bending-moment stress, for both the right and left wings at Wing Station 17.5, is illustrated in Figure 3.35 for FJ-4 139310 during Shot Magnolia. Also shown are the corresponding perturbation stress levels as calculated by the dynamic-response analysis.

The bending-moment stress at this critical structural point is caused mainly by excitation of the first normal mode of the aircraft, as seen in Figure 3.35, by the characteristic frequency of approximately 5 cps. This relatively high frequency-stress variation is superimposed on the perturbation stress level induced by the rigid-body motions of the aircraft, and the maximum combination of stress occurs at approximately $\frac{1}{10}$ second following arrival of the shock front. At this time, both contributions to the stress level reach their peak values, resulting in an overstress or dynamic-magnification factor of approximately 1.8. This relatively large dy-

dynamic-magnification factor is due to the discontinuous nature of the material velocity at the shock front.

Additional bending-moment and shear stresses are illustrated in Figures 3.36 through 3.49. Comparisons of the measured with calculated time histories of these outboard-gage readings demonstrate the apparent malfunctioning of their circuits. In nearly every case, the oscillatory frequencies, and consequently the shapes of the measured stresses, agree with the corresponding calculated values; but the magnitudes of the calculated stresses in approximately 50 percent of the cases are too small.

4.6.6 Factors Affecting the Delivery Capability. For maximum store delivery accuracy on a target, the delivery aircraft must be as close to the point of impact as possible at the time of release. Then, during the escape maneuver, the aircraft must be able to withstand the violent shock wave generated by the detonation. Section 4.6.3 mentions two important characteristics of the dynamic response that have a direct bearing on the choice of the optimum mode of delivery. The first of these factors is that the magnitude of response decreases with the blast-incidence angle as a result of the reduced normal component of material velocity. The second factor is that there is a definite alleviation of aerodynamic loading because of the increased horizontal component of material velocity at low blast angles. Both of these effects indicate that a low-angle escape maneuver will enable the aircraft to be as close to the point of impact as is practicable at the time of release.

To fully evaluate the delivery capability of the FJ-4B aircraft, the validity of the dynamic-response analysis had to be proved at conditions of low blast angle and high overpressure. The participation of the FJ-4 aircraft in Operation Hardtack facilitated the acquisition of sufficient nuclear-test data to verify the accuracy of the method of analysis. Since the method of analysis has been proved, it is now possible to determine the optimum modes of delivery for the FJ-4B and future delivery systems.

4.7 WING-PRESSURE SURVEY

A wing static-pressure survey was made on both FJ-4 test aircraft in numerous flights of the operation, in order to obtain a rational method of determining the induced aerodynamic loading on a three-dimensional lifting surface during impingement of a high-intensity blast wave. Pressure transducers measured static overpressure at 14 points on the upper and lower surfaces of Wing Stations 82.2, 141.0 and 175.8 (Figure 3.50).

Although the flat frequency response of the individual pressure gages was relatively high (400 cps), the response of the complete recording circuit was limited by the galvanometers, whose flat frequency response was only 135 cps. As a result of this response limitation, it was necessary to modify each pressure-time history to permit a more realistic representation of the applied pressures. Since nearly every rapid pressure variation appeared as a step change with approximately a 2-msec lag and a 10-percent overshoot, it was possible to fair out the lag characteristics by hand. Extreme care was taken throughout the entire data-reduction process to preserve the inherent accuracy of the original data with respect to magnitude and time sequencing.

Once the instrumentation lag was accounted for, the individual time histories of overpressure were cross plotted with percent chord at consecutive intervals of time following shock arrival at the respective trailing edges of each wing station. These chordwise distributions of incremental pressure are presented in Figures 2.51 through 3.59, for three shots of the operation. In each instance the chordwise traversal of the shock front on both the upper and lower wing surfaces is indicated by a step change of the measured pressure. The precise positioning of the shock on both the upper and lower surfaces was determined by plotting the shock-arrival time for each transducer versus percent chord. In every instance there were two notable features of these plots. First, the shock wave on the lower surface appeared to propagate at its free-stream speed, or, in the plane of the wing the relative speed was the difference between

the undisturbed propagation speed (divided by the cosine of incidence angle) and the aircraft ground speed. The second notable feature of the chordwise pressure plots was that the upper-surface shock wave always traveled at a constant speed less than the corresponding wave on the lower surface.

As shown in Figures 3.51 through 3.59, the traversal of the shock waves across the wing introduce a transient net loading on the surface. The greater portion of this load is due to the positioning of the upper and lower shock waves behind which there is an elevated pressure. In addition to the direct pressure loading associated with the shock displacement, there is a secondary loading due to the distorted flow about the surface. The shock displacement loading vanishes when the upper shock reaches the leading edge, while the flow-distortion loading gradually dies out during the first 200 msec following shock arrival. When these transitory loads diminish, the load distribution on the wing section simulates that of a quasi-steady distribution associated with an increased angle of attack at an elevated ambient pressure.

The pressure distributions of Figures 3.51 through 3.59 were integrated to give the respective section-lift time histories (Figures 3.60 through 3.62) for the first 20 msec following shock arrival at the local trailing edge. Significant of these plots is the triangular pulse of loading which occurs during this initial 20 msec. This nonlinear transient load is not predictable from the incompressible weak-gust theories, and has consequently been the most uncertain quantity of the theoretical blast-analysis problem in the past. The nonlinear effect has been called the diffraction loading and has been attributed to the high-order flow behavior associated with diffraction of the strong shock wave about the lifting surface.

In an effort to predict the diffraction loading as measured by the FJ-4 aircraft during the test series, an analytical method developed by Smiley and Krasnoff (Reference 6) was utilized. The flight and blast conditions of the three previously mentioned flights of the test series were used in the analytical approach to obtain the section-lift time histories presented in Figures 3.60 through 3.62. Comparison of the corresponding measured and analytical loadings indicates good agreement for shape over the entire range of conditions, but there are definite discrepancies in the peak magnitudes of the diffraction pulse. These discrepancies are within the anticipated accuracy of the analytical method of Reference 6, for blast-incidence angles in excess of 20°. Since the apparent error of the analytical method appeared to be a monotonic function of blast-incidence angle, a parameter was defined as the "diffraction-pulse error function." This function is simply the ratio of the analytical peak-diffraction loading to the corresponding measured value and is plotted versus the blast-incidence angle in Figure 3.63. Application of the method of Reference 6 in conjunction with the error function defined above is discussed in Appendix D.

4.8 ENGINE RESPONSE

The J65-W-16A engines in the test aircraft were instrumented to obtain data on the engine response to thermal and blast effects, with particular emphasis upon the effects of the sustained periods of overpressure and underpressure associated with high-yield weapons.

Engine response parameters which were recorded were throttle position, fuel flow, engine speed, compressor inlet and discharge pressures, fuel inlet pressure, and tailpipe temperature. Time histories of these parameters, along with histories of indicated altitude, airspeed, and outside-air temperature, are presented for FJ-4 139310, Shot Koa, in Chapter 3 (Figures 3.64 through 3.67). Additional representative time histories are presented in Appendix G for several of the other participations.

A review of the data revealed rapid increases in pressure level as an indication of shock arrival. The pressure changes were reflected by an increase in compressor inlet pressure and decreases in airspeed and altitude indication. The order of magnitude of these changes were $\frac{1}{2}$ to $1\frac{1}{2}$ psi for compressor inlet pressure with indicated reductions of 1,000 to 2,000 feet in altitude and 5 to 40 knots in airspeed. The data indicate these conditions to be consistent, thereby providing an excellent correlation for engine variations with shock arrival.

The importance of inlet-pressure fluctuation on engine-stall margin is set forth in Reference 7, which deals with investigations conducted by the National Advisory Committee for Aeronautics (NACA). Reference 7 states in brief that if inlet-pressure fluctuations exceed 3 cps, engine performance with regard to stall margin cannot be predicted on steady-state stall limits. Analysis of the data taken during this test series shows that pressure fluctuation did not exceed limits set forth by Reference 7. Therefore, it can be concluded that shock waves of the magnitude experienced will not reduce the J65-W-16A stall margin. In addition, the data indicates that compression ratios are well within those normally experienced over the operating range of the engine.

Variations in engine parameters, such as fuel flow, engine speed, etc., were essentially steady, with only minor changes in outside-air temperature and tailpipe temperature. In several tests fuel-flow fluctuations of approximately 100 gal/hr did exist; however, the variations were not of sufficient magnitude to affect engine speed. Other engine variations existed but these were due to pilot changes of power level to maintain the aircraft in the flight path schedule.

In summation, the data showed only minor magnitude changes that returned to the preshock arrival level without any appreciable oscillation or divergence. It was evident from the data that the engine was most sensitive to pressure changes, the magnitudes of which were nominal. These increases were noted to recover within 5 to 7 seconds and exhibited convergent characteristics.

The data analyzed indicates that operation of the jet engine in the test series showed insignificant engine-performance variations, with recovery immediately attained. The engine environmental-pressure variations were minor in magnitude, with convergent characteristics. Compressor-case differentials were well within the values experienced in general operation of the engine.

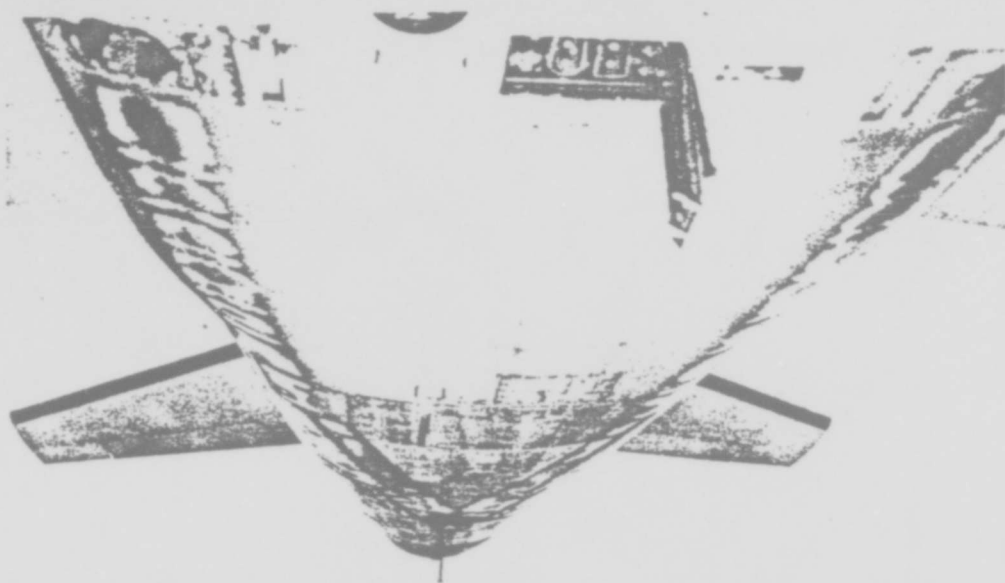


Figure 4.1 Thermal damage on the aft fuselage of Aircraft 139310, Shot Walnut.

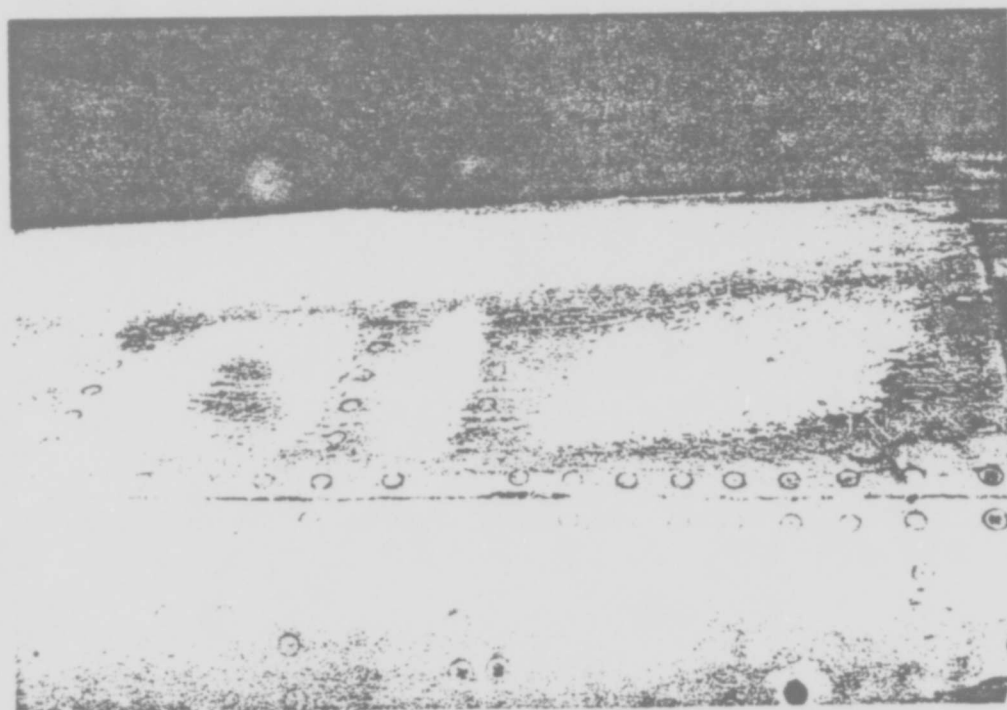


Figure 4.2 Close-up of thermal damage on the aft fuselage of Aircraft 139310; Shot Walnut.

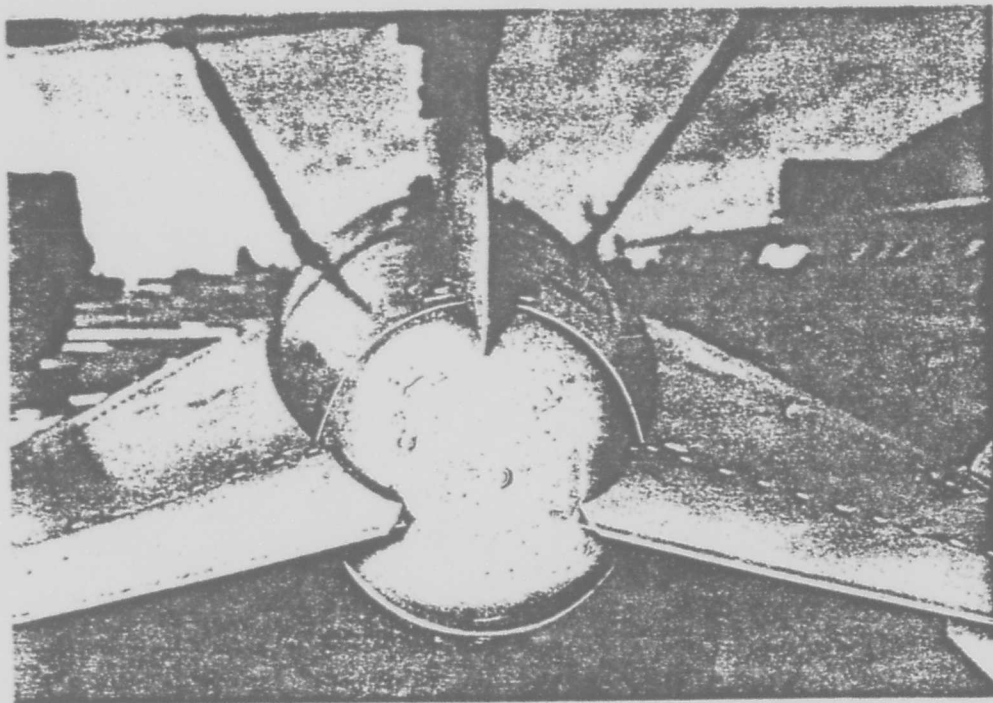


Figure 4.3 Port external fuel drop tank thermal damage, Aircraft 139310, Shot Walnut.

Chapter 5

CONCLUSIONS AND RECOMMENDATIONS

5.1 CONCLUSIONS

Correlation of all the significant radiant-exposure data obtained was quite reasonable.

From the correlation of these results and data obtained during previous testing operations with calculated effects, it is concluded that the theory presented in Appendix A for the various attenuation and other modification terms is a reliable prediction method.

These results provided valuable input to the overall study of radiant exposure, using data from Operation Ivy through Operation Hardtack. In particular, Shot Walnut provided and Shot Yellowwood gave excellent data for a hazeless Pacific atmosphere.

The remaining data, although possibly questionable as to reliability and/or desirability because of various experimental errors, is quite worthwhile in demonstrating the effect of even small amounts of mass on low-yield detonations. It is concluded that shielding by ground structures in operational situations should provide an additional margin of safety for the escape of the delivery aircraft if the prediction techniques do not account for shielding.

The methods used to predict the maximum temperature rise of thin-skins and honeycomb-panel faceplates (Appendix A) are valid for both low- and high-yield weapons.

Gamma-dose measurements from the cockpit were significantly lower than those from the ammunition bay, indicating a significant amount of shielding was afforded the pilot by the aircraft structure.

Comparisons of calculated free-stream peak overpressures and times of shock arrival with their corresponding measured values showed excellent agreement, thus confirming the accuracy of the prediction methods.

The most critical stress in the airframe during blast-wave impingement occurred as bending-moment stress at Wing Station 17.5 of the carry-through structure.

The theoretical dynamic-response analysis has been verified within the range of the test conditions for all 16 flights of the operation. This justifies the use of the method in future delivery-capability studies.

There was a discernible pulse of force on the FJ-4 wing during the first 20 msec following blast-wave impingement. This was indicated by the wing-pressure survey, which demonstrated a lag of the shock front on the upper wing surface behind the corresponding front on the lower surface. This was caused by the diffraction of the shock front about the trailing edge.

The data obtained showed engine-performance variations, but no detrimental effects were experienced. The engine environmental-pressure variations were minor in magnitude, with convergent characteristics. Compressor-case differentials were well within the values experienced in the general operation of the engine. It is therefore concluded that no engine structural damage or adverse operational effects will occur in the vicinity of low- or high-yield nuclear detonations for aircraft positions limited by other criteria.

In conjunction with the data obtained from Operation Plumbbob, thermal, blast, and structural response data has been obtained over a sufficiently wide range of yields and incidence angles to permit subsequent definition of the Class D delivery capability of the FJ-4B aircraft.

The correlations obtained justify the use of the present weapon-effect and structural-response prediction methods in future delivery-capability studies of similar aircraft.

5.2 RECOMMENDATIONS

Future planning for further airborne measurements of radiant exposure in full-scale nuclear testing should incorporate the following considerations: (1) use of 90°-field-of-view instruments only, (2) duplication of each measuring instrument to avoid inadvertent introduction of individual instrument error, (3) specification of planned or possible shielding of each event prior to selection for participation and avoidance of participation in shielded events when thermal data is of interest, and (4) location of instruments to minimize accumulation of foreign matter on the filters.

Further analysis should be made of the existing thermal data from airborne instruments to determine if the prediction techniques can be simplified within acceptable limits to provide rapid calculational procedures for use in operational delivery-capability studies.

Appendix A

THERMAL-EFFECT THEORY

A.1 COMPUTATIONAL PROCEDURE FOR RADIANT EXPOSURE

An analytical investigation of the airborne thermal measurements taken not only during Operations Hardtack and Plumbbob, but also as far back as Operation Ivy, has resulted in the development of the following methods for predicting radiant exposure on an airborne receiver. A detailed derivation of the equations may be found in Reference 8. It should be noted that although the equations appear to be written in terms of the radiant exposure normal to an actual flat-plate receiver, the prediction of direct exposure is entirely feasible with this method.

$$Q_{TN} = \frac{0.365 W \times 10^{12}}{4 \pi (929) R^2} [K_1' T_1 \sin i_{eff} + \beta T_2 T_3 K_4] (1-F) \quad (A.1)$$

Where: Q_{TN} = total normal radiant exposure, cal/cm²

0.365 W = thermal yield of the device, kt

W = hydrodynamic yield of the device, kt

10¹² = conversion factor from kilotons to calories, cal/kt

4 π R² = inverse-square law factor, ft²

R = slant range from center of burst to receiver, ft

929 = conversion factor from ft² to cm², cm²/ft²

K₁' T₁ sin i_{eff} = incident radiant exposure correction factor, dimensionless

K₁' = geometric correction factor for surface and intermediate bursts, dimensionless

= f₂ + f₁ f₃ gh, if H_b > 0

= gh - ψ, if H_b = 0

f₁ = fraction of total radiant exposure emitted during hemispherical phase of the fireball, dimensionless

= 1, if H_b/W^{1/3} < 177

= 0, if H_b/W^{1/3} > 369

= 6.21 × 10⁶ $\left[\frac{W}{H_b^3} - 2.0 \times 10^{-8} \right]$, if 177 ≤ $\frac{H_b}{W^{1/3}}$ ≤ 369

f₂ = fraction of total radiant exposure emitted during spherical phase of the fireball, dimensionless

= 1 - f₁

f₃ = correction factor for change of apparent color temperature with burst height, dimensionless

= 1.63, if H_b/W^{1/3} ≥ 183

= 3.41 × 10⁻³ $\frac{H_b}{W^{1/3}} + 1$, if H_b/W^{1/3} < 183

gh = fraction of spherical fireball as seen by a flat-plate receiver in space during the hemispherical fireball phase, dimensionless
 $= 0.5 (1 + \sin i^*)$

i^* = angle of elevation of the receiver with respect to the center of the fireball, deg

$$= \sin^{-1} \left[\frac{H_{ac} - H_b}{R} \right]$$

ϕ = correction factor for surface-burst plume, dimensionless

$$= \frac{0.39290 (H_{ac} - R_h)}{\sqrt{(H_{ac} - R_h)^2 + D^2}}, \text{ if } \frac{H_{ac} - R_h}{\sqrt{(H_{ac} - R_h)^2 + D^2}} \geq 0.26724$$

$$= 0.10483, \text{ if } \frac{H_{ac} - R_h}{\sqrt{(H_{ac} - R_h)^2 + D^2}} < 0.26724$$

H_{ac} = height of receiver above ground surface, ft

D = horizontal range between center of burst and receiver, ft

R_h = radius of surface-burst fireball, ft
 $= 302 W^{1/3}$

H_b = height of burst above ground surface, ft

T_1 = transmissivity of the atmosphere on the incident vector path, dimensionless (see Section A.1.1)

$\sin i_{eff}$ = geometric conversion of the incident radiant exposure vector to its component normal to a flat-plate receiver in space, dimensionless

$i_{eff} = i$, if $i \geq 20^\circ$

$= 20^\circ$, if $i \leq 20^\circ$

i = angle subtended by the incident radiant exposure vector and the desired component of that vector, deg

$\beta T_2 T_3 K_4$ = reflected radiant-exposure correction factor, dimensionless

β = albedo of the ground surface, dimensionless (see Section A.1.2)

T_2 = transmissivity of the atmosphere along an arbitrary average path from the burst to the ground surface, dimensionless (see Section A.1.1)

T_3 = transmissivity of the atmosphere along an arbitrary average path from the ground surface to the receiver, dimensionless (see Section A.1.1)

K_4 = ratio of unattenuated reflected radiant exposure to unattenuated incident radiant exposure, dimensionless

$$= f_2 \frac{Q_{RN}}{Q_{I_1}} + f_1 f_3 J \frac{Q_{RN}}{Q_{I_2}}$$

$\frac{Q_{RN}}{Q_{I_1}}$ = ratio of unattenuated reflected radiant exposure normal to a flat-plate receiver in space to the unattenuated incident radiant exposure as seen by a flat-plate receiver in space from a spherical fireball at height H_b above the ground surface, dimensionless

$$= f \left(\frac{H_{ac}}{H_b}, \frac{D}{H_b}, B \right), \text{ (Reference 9)}$$

$\frac{Q_{RN}}{Q_{I_2}}$ = ratio of unattenuated reflected radiant exposure normal to a flat-plate receiver in space to the unattenuated incident radiant exposure as seen by a flat-plate receiver in space from a spherical fireball at height $H_b + R_b$ above the ground surface, dimensionless

$$= f \left(\frac{H_{ac}}{H_b + R_h}, \frac{D}{H_b + R_h}, B \right), \text{ (Reference 9)}$$

B = orientation angle of the flat-plate receiver from the horizontal, deg

$$= A, \text{ if } A \geq 0$$

$$= 180 - |A|, \text{ if } A < 0$$

A = angle of elevation or depression of the flat-plate receiver with respect to a horizontal vector directed away from the burst, deg

J = hemispherical fireball correction factor to convert reflected radiant exposure from a spherical fireball at height $H_b + R_h$ to reflected radiant exposure from a hemispherical fireball at height H_b , dimensionless

$$= \frac{0.50 R^2}{R_h^2 (1 + \sin i^*) [(R/R_h) - \sin i^*]^2}$$

(1-F) = correction factor for motion of the receiver, dimensionless

$$= \frac{\int_0^{\infty} \frac{\sin [i_{eff}(t)] \times T_1(t) \times q(t) \times dt}{R^2(t)} + \beta T_2 T_3 K_4 \int_0^{\infty} \frac{q(t) dt}{R^2(t)}}{\frac{T_1 \sin i_{eff} + \beta T_2 T_3 K_4}{R^2} \int_0^{\infty} q(t) dt} \quad (\text{A.2})$$

t = real time, sec

q(t) = irradiance, (cal/cm²)/sec

Table A.1 presents the values of the primary intermediate parameters used in the calculation of the radiant exposure values presented in Chapter 3.

A.1.1 Transmissivity. The transmissivity of the atmosphere was determined by using the basic Chapman and Seavy technique (Reference 10) with minor modifications to account for various geometries of the burst, receiver, and haze layer. This method of deriving transmissivities incorporates the phenomena of return scattering in the buildup coefficients and therefore precludes the use of a separate scattering term in the basic Q_{TN} equation. Consideration was also given to the fact that reflected radiation must travel a longer path to reach the receiver than incident radiation. An average reflection point was chosen commensurate with the albedo investigation described in the following section and the linear paths to this point from both the burst and the receiver were used to evaluate the attenuation of the reflected radiant exposure. The following sets of equations delineate completely the computational procedures used for determining transmissivities:

T_1 = transmissivity of the atmosphere along the incident vector path, dimensionless

$$= F_v T_{v_1} + F_{ir} T_{h_1} T_{w_1}$$

F_v = fraction of radiation in the visible spectrum ($\lambda < 0.7$ micron), dimensionless

$$= f(T_k) \text{ (Reference 10)}$$

F_{ir} = fraction of radiation in the infrared spectrum ($\lambda > 0.7$ micron), dimensionless

$$= f(T_k) \text{ (Reference 10)}$$

T_k = color temperature of the fireball, °K

$$= 7,000 W^{-0.01}, \text{ if } H_b/W^{1/3} < 177$$

$$= 7,000 W^{-0.03}, \text{ if } H_b/W^{1/3} \geq 177$$

T_{v_1} = transmissivity of the atmosphere in the visible spectrum on the incident vector path, dimensionless

$$= 0.3 \exp \left\{ -\frac{0.0875}{\sin i^*} \left[\exp(-4.57 \times 10^{-5} \tau_1) - \exp(-4.57 \times 10^{-5} \tau_2) \right] \right\}$$

$$\cdot \exp \left\{ \frac{-16.40}{V_{1s} \sin i^*} \left[\exp(-4.57 \times 10^{-5} \tau_3) - \exp(-4.57 \times 10^{-5} \tau_4) \right] \right\}$$

$$+ 0.7, \text{ if } H_{ac} \neq H_b$$

$$= 0.5 \exp \left\{ -4 \times 10^{-6} (R - R_h) \exp[-4.57 \times 10^{-5} (H_{ac} - H_g)] \right\} + 0.5, \\ \text{if } H_{ac} = H_b \text{ and } H_{ac} > H_h$$

$$= 0.5 \exp \left\{ \frac{-7.5 \times 10^{-4} (R - R_h)}{V_{1s}} \left[\exp -4.57 \times 10^{-5} (H_{ac} + H_g) \right] \right\} + 0.5,$$

$$\text{if } H_{ac} = H_b \text{ and } H_{ac} \leq H_h$$

T_{h_1} = transmissivity of haze in infrared spectrum on the incident vector path, dimensionless

$$= 0.3 \exp \left\{ \frac{-16.40}{V_{1s} \sin i^*} \left[\exp(-4.57 \times 10^{-5} \tau_3) - \exp(-4.57 \times 10^{-5} \tau_4) \right] \right\}$$

$$+ 0.7, \text{ if } H_{ac} \neq H_b$$

$$= 1.00, \text{ if } H_{ac} = H_b \text{ and } H_{ac} > H_h$$

$$= T_{v_1}, \text{ if } H_{ac} = H_b \text{ and } H_{ac} \leq H_h$$

$$T_1 = 1.0, \text{ if } H_{ac} \leq H_h \text{ and } H_b' \leq H_h$$

$$= H_b + H_g, \text{ if } H_{ac} \leq H_h \text{ and } H_b' > H_h$$

$$= H_h + H_g, \text{ if } H_{ac} > H_h \text{ and } H_b' \leq H_h$$

$$= H_b' + H_g, \text{ if } H_{ac} > H_h \text{ and } H_b' > H_h$$

$$T_2 = 1.0, \text{ if } H_{ac} \leq H_h \text{ and } H_b' \leq H_h$$

$$= H_b' + H_g, \text{ if } H_{ac} \leq H_h \text{ and } H_b' > H_h$$

$$= H_{ac} + H_g, \text{ if } H_{ac} > H_h$$

$$T_3 = H_{ac} + H_g, \text{ if } H_{ac} \leq H_h \text{ and } H_b' \leq H_h \text{ and } H_{ac} < H_b'$$

$$= H_b' + H_g, \text{ if } H_{ac} \leq H_h \text{ and } H_b' \leq H_h \text{ and } H_{ac} > H_b'$$

$$= H_{ac} + H_g, \text{ if } H_{ac} \leq H_h \text{ and } H_b' > H_h$$

$$= H_b' + H_g, \text{ if } H_{ac} > H_h \text{ and } H_b' \leq H_h$$

$$= 1.00, \text{ if } H_{ac} > H_h \text{ and } H_b' > H_h$$

$$\begin{aligned}
T_i &= H_b' + H_g, \text{ if } H_{ac} \leq H_h \text{ and } H_b' \leq H_h \text{ and } H_{ac} < H_b' \\
&= H_{ac} + H_g, \text{ if } H_{ac} \leq H_h \text{ and } H_b' \leq H_h \text{ and } H_{ac} > H_b' \\
&= H_h + H_g, \text{ if } H_{ac} \leq H_h \text{ and } H_b' > H_h \\
&= H_h + H_g, \text{ if } H_{ac} > H_h \text{ and } H_b' \leq H_h \\
&= 1.00, \text{ if } H_{ac} > H_h \text{ and } H_b' > H_h
\end{aligned}$$

H_{ac} = altitude of aircraft above ground, ft

$$H_b' = H_b + \frac{R_h \sin i^*}{2}$$

H_b = altitude of burst above ground, ft

H_h = altitude of top of haze layer above ground, ft

H_g = elevation of ground above MSL, ft

V_{is} = visibility of atmosphere at ground surface, statute miles

T_{w1} = transmissivity of water vapor in infrared spectrum on incident vector path, dimensionless

$$= f(A_1, T_k) \text{ (Reference 10)}$$

A_1 = water-vapor path on incident vector path, mm H_g

$$= \frac{2.30 P_0}{\sin |i^*|} \left| 10^{-\frac{(H_b' + H_g) \times 10^{-3}}{16.4}} - 10^{-\frac{(H_{ac} + H_g) \times 10^{-3}}{16.4}} \right|, \text{ if } H_{ac} = H_b$$

$$= 3.25 P_0 (R - R_h) \left[10^{-\frac{(H_{ac} + H_g) \times 10^{-3}}{16.4}} \right], \text{ if } H_{ac} = H_b$$

P_0 = water-vapor pressure at sea level, mm

$T_2 T_3$ = total transmissivity of reflected radiant exposure, dimensionless

$$= F_v T_{v2} T_{v3} + F_{ir} T_{h2} T_{h3} T_{w2-3}$$

T_{v2} = fractional transmission due to scattering in the visible region from burst to average reflection point, dimensionless

$$= 0.3 \exp \{ -0.0875 \csc \alpha [\exp (-4.57 \times 10^{-5} T_5) - \exp (-4.57 \times 10^{-5} T_6)] \}$$

$$\cdot \exp \left\{ \frac{-16.4 \csc \alpha}{V_{is}} \left[\exp (-4.57 \times 10^{-5} T_7) - \exp (-4.57 \times 10^{-5} T_8) \right] \right\}$$

$$+ 0.7, \text{ if } H_b/W^{1/3} \geq 177$$

$$= 1.00, \text{ if } H_b/W^{1/3} < 177$$

T_{v3} = fractional transmission due to scattering in the visible region from average reflection point to the receiver, dimensionless

$$= 0.3 \exp \{ -0.0875 \csc \alpha [\exp (-4.57 \times 10^{-5} T_9) - \exp (-4.57 \times 10^{-5} T_{10})] \}$$

$$\cdot \exp \left\{ \frac{-16.4 \csc \alpha}{V_{is}} \left[\exp (-4.57 \times 10^{-5} T_{11}) - \exp (-4.57 \times 10^{-5} T_{12}) \right] \right\}$$

$$+ 0.7$$

T_{h2} = fractional transmission due to scattering in the haze layer from burst to average reflection point, dimensionless

$$= 0.3 \exp \left\{ \frac{-16.4 \csc \alpha}{V_{1s}} \left[\exp(-4.57 \times 10^{-5} T_7) - \exp(-4.57 \times 10^{-5} T_8) \right] \right\}$$

$$+ 0.7, \text{ if } H_b/W^{1/3} \geq 177$$

$$= 1.00, \text{ if } H_b/W^{1/3} < 177$$

$$T_6 = 1.0, \text{ if } H_b' \leq H_h$$

$$= H_h + H_g, \text{ if } H_b' > H_h$$

$$T_8 = 1.0, \text{ if } H_b' \leq H_h$$

$$= H_b' + H_g, \text{ if } H_b' > H_h$$

$$T_7 = H_g, \text{ for all cases}$$

$$T_9 = H_b' + H_g, \text{ if } H_b' \leq H_h$$

$$= H_h + H_g, \text{ if } H_b' > H_h$$

T_{h_3} = fractional transmission due to scattering in the haze layer from average reflection point to receiver, dimensionless

$$= 0.3 \exp \left\{ \frac{-16.4 \csc \alpha}{V_{1s}} \left[\exp(-4.57 \times 10^{-5} T_{11}) - \exp(-4.57 \times 10^{-5} T_{12}) \right] \right\}$$

$$+ 0.7$$

$$T_9 = 1.0, \text{ if } H_{ac} \leq H_h$$

$$= H_h + H_g, \text{ if } H_{ac} > H_h$$

$$T_{10} = 1.0, \text{ if } H_{ac} \leq H_h$$

$$= H_{ac} + H_g, \text{ if } H_{ac} > H_h$$

$$T_{11} = H_g, \text{ for all cases}$$

$$T_{12} = H_{ac} + H_g, \text{ if } H_{ac} \leq H_h$$

$$= H_h + H_g, \text{ if } H_{ac} > H_h$$

$T_{W_{2-3}}$ = fractional transmission in infrared region due to water-vapor absorption over the entire path from burst to average reflection point to receiver, dimensionless

$$= f(\Lambda_{2-3}, T_k)$$

$$\Lambda_{2-3} = 2.3 P_0 \left(10^{\frac{-(H_b'' + H_g) \times 10^{-3}}{16.4}} - 10^{\frac{-(H_{ac} + H_g) \times 10^{-3}}{16.4}} \right) \csc \alpha$$

$$H_b'' = H_b - \frac{R_s \sin \alpha}{2}, \text{ if } H_b/W^{1/3} \geq 177$$

$$= R_h \tan \alpha, \text{ if } H_b/W^{1/3} < 177$$

$$R_s = \text{radius of airburst fireball, ft}$$

$$= 240 W^{1/3}$$

$$R_h = \text{radius of surface-burst fireball, ft}$$

$$= 302 W^{1/3}$$

$$\alpha = \tan^{-1} \left\{ (H_b + H_{ac})/D \right\}, \text{ if } H_b/W^{1/3} \geq 177$$

$$= \tan^{-1} \left\{ H_{ac}/(D - 1.5 R_h) \right\}, \text{ if } H_b/W^{1/3} < 177$$

A.1.2 Albedo. The reflectivity of the ground surface admittedly varies from point to point on an arbitrarily large plane below the burst; however, the specification of varying albedo for different portions of the reflecting plane is a monumental task at best. Consequently, constant values of albedo for the entire plane have been reasonably determined and used for different types of surface conditions. At the Nevada Test Site, such a technique should be an excellent approximation. For the Eniwetok Proving Ground, however, the shock wave produces a highly reflective froth on a comparatively highly absorbent water surface. Such a gross change in albedo, especially when it may be strongly variable with yield and burst height, should be adjusted for in the sophisticated methods necessary for test data correlation. The following equation was developed to account for the change in albedo due to shock froth for over-water and water-surface bursts.

β = average albedo at the average reflection point, dimensionless

$$= 0.1 F_4 + 0.7 (1 - F_4)$$

$$= 0.7 - 0.6 F_4$$

0.1 = albedo of unfrothed smooth water, dimensionless

0.7 = albedo of shock-frothed water, dimensionless

F_4 = fraction of energy emitted prior to arrival of the shock wave at the average reflection point, dimensionless

$$= 0.18 + 0.2737 \log \left(\frac{t_{D_r}}{\eta} \right)$$

$$\eta = 0.032 W^{1/2}$$

t_{D_r} = time required for shock wave to reach the average reflection point (D_r), sec

$$= \left(\frac{1}{1.170} \right) \left(\frac{C_{s1}}{C_b} \right) \left[(H_b^2 + D_r^2)^{1/2} - 570 (2W)^{1/3} (p_0/p_b)^{1/3} \right]$$

C_{s1} = speed of sound at sea level, (NACA Standard Atmosphere), ft/sec

C_b = speed of sound at burst altitude, ft/sec

p_0 = pressure at sea level (NACA Standard Atmosphere), psi

p_b = ambient pressure at burst altitude, psi

Implicit in this treatment of water-surface albedo and in the foregoing transmissivity investigation, is the concept of an average reflection point. This concept is necessary to permit reasonable simplification of the reflected radiant-exposure transmission problem and variation of water-surface albedo due to shock-wave effects. For surface bursts, the average reflection point was chosen to be $1\frac{1}{2}$ hemispherical fireball radii from the center of the burst. This same choice applied to over-water bursts whose scaled burst heights ($H_b/W^{1/3}$) are less than 177. For scaled burst heights greater than 177, the reflected flux was assumed to be specular. Consequently, the average reflectance point is specified as:

D_r = horizontal range of average reflection point from ground zero, ft

$$= \frac{H_b D}{H_b + H_{ac}}, \text{ if } H_b > 177$$

$$= 1.5 R_h, \text{ if } H_b \leq 177$$

A more detailed discussion of this investigation is contained in Reference 8.

A.2 COMPUTATIONAL PROCEDURE FOR IRRADIANCE

Equation A.3 was used to calculate the irradiance-time histories.

$$q(t) = \frac{q_{\max}}{4\pi(929)} \times q_n(t_n) \left[\frac{K_1' \sin i_{\text{eff}}(t) \times \exp[R(t)/R_0] \ln T_1}{R(t)^2} + \frac{\beta T_2 T_1 K_4}{R(t)^2} \right] \quad (\text{A.3})$$

Where: $q(t)$ = irradiance at time, t , (cal/cm²)/sec

q_{\max} = peak power, cal/sec

$$= 4.85 W^{1/2}$$

W = hydrodynamic yield of the device considered, kt

$R(t)$ = slant range from the center of the burst to the test aircraft at time t , ft

$$= \sqrt{(H_{\text{ac}} - H_b)^2 + [D + V_{\text{ac}} \times (t/\eta) \times \eta]^2}, \text{ for level flight}$$

H_{ac} = altitude of test aircraft, ft

H_b = altitude of burst, ft

D = horizontal distance of test aircraft from burst at time zero, ft

V_{ac} = true ground speed, ft/sec

R_0 = slant range from the center of the burst to the test aircraft at time zero, ft

i_{eff} = i where $i \geq 20^\circ$

= 20° where $i \leq 20^\circ$

i = angle of incidence of flux to the plane of the surface to be considered, deg

$q_n(t_n)$ = generalized thermal pulse

t_n = normalized time, dimensionless

$$= t/\eta$$

t = time, sec

η = time to maximum irradiance, sec

$$= 0.032 \times W^{1/2}$$

929 = conversion factor, cm²/ft²

β = ground albedo

All other factors are discussed in detail in Section A.1.

It was assumed that only slant range, effective incidence angle, and q_n were time-dependent variables for the duration of the thermal pulse. Consequently, the remaining variables were evaluated as parameters for the position of the test aircraft at time zero. The primary parameters and their values were previously discussed in Section A.1.

An IBM 704 Fortran program was compiled to calculate $q(t)$, using Equation A.3. The computational procedure involved arbitrarily selecting values of t_n and computing $q(t)$. The number of calculated values of $q(t)$ is dependent upon the number of points from the q_n versus t_n curve which are loaded into the program as a table. The program also performs a stepwise trapezoidal integration to provide a calculated radiant-exposure time history.

A.3 THERMAL RESPONSE

The thermal-response analysis was divided into four parts: (1) temperature-time history of thin skins, (2) maximum temperature rise of thin skins, (3) temperature-time history of honeycomb-panel faceplates, and (4) maximum temperature rise of honeycomb-panel faceplates. Each of these areas involved a different method of computation. These methods are presented in Paragraphs A.3.1 through A.3.4.

A.3.1 Temperature-Time History of a Thin Skin. Based on the assumptions that the skin is a thin plate with an adiabatic wall at the inner surface and that heat flow along the skin is negligible, a simple heat-

balance equation around the skin can be written in the form:

$$\text{Heat In} = \text{Heat loss by convection} + \text{heat loss by radiation} + \text{gain in storage}$$

or:

$$q(t) + q_i = h_s (T - T_{bl}) + (7.52 \times 10^{-5}) \sigma \epsilon T^4 + G (dT/dt) \quad (\text{A.4})$$

Where:

$q(t)$ = irradiance at time, t , (cal/cm²)/sec

q_i = heating rate from internal source, (cal/cm²)/sec

h_s = turbulent-heat-transfer coefficient, (cal/cm²)/sec-°F, (see Equation A.9)

T = temperature of skin at time, t , °Ra

T_{bl} = boundary-layer temperature, °Ra

7.52×10^{-5} = factor for conversion of the radiation loss term from Btu/hr-ft² to (cal/cm²)/sec

σ = Stefan-Boltzmann constant

ϵ = emissivity for reradiation in the infrared spectrum

G = skin and paint heat capacity, cal/cm²-°F, (see Section A.3.2)

Since the heating rate from an internal source can be expressed as,

$$q_i = h_s (T_0 - T_{bl}), \text{ cal/cm}^2$$

Where: T_0 = temperature of skin at time zero, °Ra

Then

$$q(t) = h_s (T - T_0) + (7.52 \times 10^{-5}) \sigma \epsilon T^4 + G (dT/dt) \quad (\text{A.5})$$

Since no algebraic relationship exists for $q(t)$, Equation A.5 is solved for T versus t by the method of finite differences in the following manner:

Assume:

$$\frac{dT}{dt} = \frac{T_n - T_{n-1}}{t_n - t_{n-1}} = \frac{T_n - T_{n-1}}{\Delta t}$$

$$T = \frac{T_n + T_{n-1}}{2}$$

$$T^4 = (T_{n-1})^4$$

Where: T_n = temperature at t_n , °Ra

T_{n-1} = temperature at t_{n-1} , °Ra

$$t_{n-1} = t_n - \Delta t$$

The above assumptions linearize Equation A.5. Substituting these relations into Equation A.5, the finite difference Equation A.6 for T_n is established.

$$T_n = \frac{\left[\frac{\gamma}{2} (q_n + q_{n-1}) + h_s \left(T_0 - \frac{T_{n-1}}{2} \right) - (7.52 \times 10^{-5}) \sigma \epsilon (T_{n-1})^4 \right] 2 \Delta t + 2G T_{n-1}}{2G + h_s \Delta t} \quad (\text{A.6})$$

Where: T_n = temperature of skin at time t_n , °Ra

q_n = irradiance at time t_n , (cal/cm²)/sec

q_{n-1} = irradiance at time t_{n-1} , (cal/cm²)/sec

γ = skin-absorption coefficient, dimensionless

T_0 = initial temperature of the skin, °Ra

An IBM 704 Fortran program was written to solve Equation A.6. Computational procedure involves the loading of the physical and thermal properties of the skin considered and selected values of $q(t)$ from the thermal pulse as input data. The program then computes the temperature-time history of the thin skin under consideration.

A.3.2 Thin-Skin Maximum Temperature Rise. Since the conventional skin-stringer structure at the selected thermocouple locations in Table 3.6 satisfied the thin-skin criteria in Reference 11, the maximum temperature rise was calculated by Equation A.7.

$$\Delta T_m = \frac{Q_{TN} \times \gamma \times (1-FH)}{G \times (1-F)}, \text{ } ^\circ\text{F} \quad (\text{A.7})$$

Where: ΔT_m = maximum temperature rise, °F

Q_{TN} = radiant exposure from Equation A.1, cal/cm²

γ = skin-absorption coefficient, dimensionless

$G = \rho_s C_{p_s} b_s + \rho_p C_{p_p} b_p$, cal/cm²·°F

ρ_s = skin density, gm/cm³

C_{p_s} = specific heat of skin material, cal/gm·°F

b_s = skin thickness, cm

ρ_p = paint density, gm/cm³

C_{p_p} = specific heat of paint material, cal/gm·°F

b_p = paint thickness, cm

(1-F) = flyaway factor for horizontal flight (see Equation A.2)

(1-FH) = combined convective cooling and flyaway factor (see Section A.3.5)

Table A.2 lists the factors used in the calculation of G . The ratio (1-FH)/(1-F) is used since it was determined that the flyaway and convective cooling effects are interdependent, and (1-F) is divided into Q_{TN} to cancel the (1-F) incorporated in Equation A.1 for calculated values and to cancel the (1-F) inherent in measured radiant exposure. The (1-FH) and (1-F) factors computed for the thermal-response analysis are presented in Tables A.3 and A.4 respectively.

A.3.3 Honeycomb-Panel Temperature-Time Histories. Since a honeycomb panel cannot be considered mathematically as a homogeneous skin due to its heat-sink properties, an analysis was conducted to parametrically represent the thermal response of the honeycomb-panel faceplates. This parametric study necessitated the computation of temperature-time histories of the honeycomb-panel components. The computation of these temperature-time histories was based on the following assumptions:

1. The heat transfer through the air in the core by conduction, convection, and radiation is negligible. (This is reasonable considering the temperature ranges and gradients involved.)
2. The temperature gradient across the core is a straight-line gradient. (This is also reasonable considering the small depth of the panel.)
3. The variation in thermal properties of both the aluminum material and adhesive HT-424 over the temperature range under consideration is negligible.
4. The core is a homogeneous layer with an equivalent thermal conductivity (see Section A.3.4).

Using these assumptions, the temperature-time histories were calculated with an IBM 704 one-dimensional heat-transfer program. A heat balance was written around each of the following elements: (1) faceplate, (2) faceplate adhesive, (3) core, (4) backplate adhesive, and (5) backplate. This resulted in five

simultaneous equations for each increment of time. Loading the physical and thermal properties of the individual components and irradiance versus time as input data, the program computed the temperature-time history of each element. A detailed derivation of the honeycomb-response equations is presented in Reference 12.

A.3.4 Honeycomb Faceplate Maximum Temperature Rise. Since a honeycomb panel is a complex structure with a built-in heat sink, the effects of flyaway and convective cooling on its thermal response are significantly different from the effects on the thermal response of thin skins. As pointed out in Section A.3.3 and derived in Reference 12, accurate time-dependent solutions of honeycomb-thermal response have been accomplished using a finite-difference type of solution in an IBM 704 heat-transfer program. These time-dependent solutions are both costly and time consuming; therefore, the derivation of a time-independent solution was imperative. This was accomplished by conducting a dimensional analysis for the determination of the important parameters and using the results of various time-dependent solutions to determine the effect of these parameters on the thermal response of honeycomb panels. The result of this analysis is presented in Figure A.3 as $(1-FH)_{10\eta}$ versus τ' and $(1-F)_{10\eta}$, then

$$\Delta T_m = \frac{\gamma \times Q_{TN}/10\eta (1-FH)_{10\eta}}{G \times (1-F)_{10\eta}}$$

Where: ΔT_m = faceplate maximum temperature rise, °F

$Q_{TN}/10\eta$ = normal radiant exposure at 10 times the time to maximum irradiance, 10η , cal/cm²

γ = skin absorptivity

$(1-FH)_{10\eta}$ = combined flyaway and convective cooling factor for honeycomb panels

$(1-F)_{10\eta}$ = flyaway factor at 10 times the time to peak irradiance, 10η

τ' = honeycomb thermal-response parameter

$$= 0.10 \ln \left(\frac{h_s X_c}{k_c} \right) + 0.03 \ln \left(\frac{G}{G_c} \right) + 0.275 \ln \left(\frac{G}{h_s \eta} \right)$$

h_s = turbulent-heat-transfer coefficient, cal/cm²-sec-°F (see Section A.3.6)

X_c = depth of core, cm

k_c = equivalent thermal conductivity of the core, cal-cm/cm²-sec-°F

$$= \frac{\rho_c}{\rho_{al}} k_{al}$$

ρ_c = density of core, gm/cm³

ρ_{al} = density of core material, gm/cm³

k_{al} = thermal conductivity of core material, cal-cm/cm²-sec-°F

G = heat capacity of paint, faceplate, and adhesive layer, cal/cm²-°F

$$= \rho_p C_{p_p} b_p + \rho_s C_{p_s} b_s + \rho_g C_{p_g} b_g$$

ρ_g = density of adhesive, gm/cm³

C_{p_g} = specific heat of adhesive, cal/gm-°F

b_g = thickness of adhesive, cm

G_c = core heat capacity, cal/cm²-°F

$$= \rho_c C_{p_c} X_c$$

C_{p_c} = specific heat of core material, cal/gm-°F

η = time to maximum irradiance, sec

Figure A.3 is reliable for use in predicting the thermal response of the FJ-4B aileron, flap, and elevator honeycomb panels for yields ranging from 10 kt to 15 Mt with 10-percent maximum deviation. Figure A.2 presents the honeycomb thermal-response parameter, r' , versus h_g and η for the aileron and flap honeycomb panels. Figure A.3 presents r' versus h_g and η for the elevator honeycomb panel. The parameters used in the computation of Figures A.2 and A.3 are presented in Table A.5.

A detailed derivation of Figure A.1 is given in Reference 12.

A.3.5 Combined Flyaway and Convective Cooling Factor, (1-FH). The combined flyaway and convective cooling factor for thin skin based on the infinite time value of radiant exposure was calculated by Equation A.8

$$(1-FH) = \frac{\Delta T_m}{\Delta T_{ref}} \quad (A.8)$$

Where: ΔT_m = maximum temperature rise (Equation A.6), °F

$$= T_m - T_0$$

ΔT_{ref} = maximum temperature rise with no flyaway or convective cooling, °F

$$= \frac{Q_{TN}}{G(1-F)}$$

Q_{TN} = radiant exposure, cal/cm², Equation A.1

G = skin and paint heat capacity, cal/cm²-°F

(1-F) = flyaway factor, Equation A.2

The calculation of maximum temperature rise in Equation A.6 was accomplished using the calculated irradiance from Equation A.3.

A.3.6 Turbulent-Heat-Transfer Coefficient. The equation used to obtain the external convection heat-transfer coefficients is presented below:

$$h_g = 0.00803 (K/L) R_e^{0.8} P_r^{0.33} \quad (A.9)$$

Where: h_g = turbulent-heat-transfer coefficient, cal/cm²-sec-°F

K = thermal conductivity, Btu-ft/ft²-sec-°F

L = characteristic length, ft

$R_e = (\rho V L)/\mu$ = Reynolds Number

ρ = density, slugs/ft³

V = velocity, ft/sec

μ = absolute viscosity, lb-sec/ft²

$P_r = (C_p \mu)/K$ = Prandtl Number

C_p = specific heat, Btu/lb-°F

Since all of the above properties are based on the temperature of the boundary layer, the following equation is used to calculate this reference temperature, T^* .

$$T^* = 0.5 [T_a + T_{bl} + 0.162 (V_{ac}/100)^2] \quad (A.10)$$

Where: T_a = free-stream static temperature, °Ra

T_{bl} = turbulent-boundary-layer temperature, °Ra

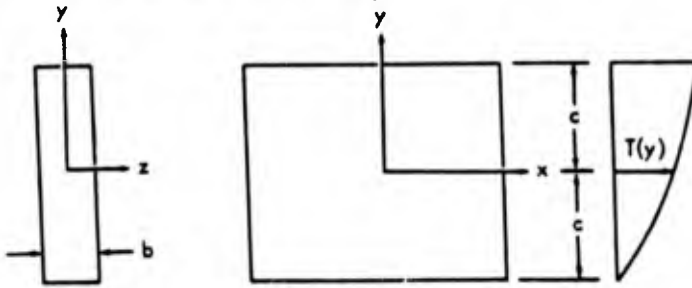
$$= T_a + 0.746 (V_{ac}/100)^2$$

V_{ac} = true airspeed, ft/sec

A.4 THERMAL-STRESS THEORY

Thermal stresses were computed by means of a general equation (A.19) which was derived by an expansion of information obtained from Reference 13 as follows:

Assume a one-dimensional temperature distribution $T(y)$.



With the assumed temperature distribution $T(y)$ and the plate fully restrained with no buckling the stress distribution becomes

$$f_x = \alpha E T(y) \quad (A.11)$$

Where: α = coefficient of thermal expansion
 E = modulus of elasticity

If we free the plate of end restraints but not bending, a relief stress is realized. This relief stress is superposed on the full restraint stresses. The total tensile load P_x may be written as

$$P_x = \int_{-c}^c \alpha E T(y) b dy$$

The resultant relief stress becomes

$$(f_x)_t = (P_x/A) = (1/A) \int_{-c}^c \alpha E T(y) dA \quad (A.12)$$

Where: A = total area of section, $dA = b dy$.

Because the temperature distribution is unsymmetrical the tensile forces have a resultant moment. Thus, when the plate is unrestrained in bending an unbalance relief moment results

$$M_z = \int_{-c}^c \alpha E T(y) b y dy$$

The resulting relief stress becomes

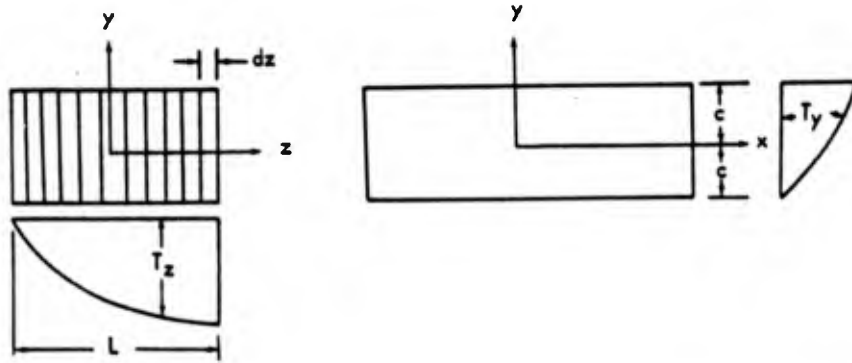
$$(f_x)_b(z) = \frac{M_z y}{I_z} = \frac{y}{I_z} \int_{-c}^c \alpha E T(y) y dA \quad (A.13)$$

Where: y = distance to element center of gravity.

The one-dimensional thermal-stress equation is formed by combining Equations A.11, A.12, and A.13 as follows:

$$f_x = -\alpha E T(y) + \frac{1}{A} \int_{-c}^c \alpha E T(y) dA + \frac{y}{I_z} \int_{-c}^c \alpha E T(y) y dA \quad (A.14)$$

In the practical situation a two-dimensional temperature distribution will exist. For the case of the two-dimensional temperature the dimension b will be considered as dz and several more of the one-dimensional sections can be added to simulate the two-dimensional problem.



Considering the two-dimensional temperature distribution, $T(y,z)$, the thermal-stress Equation A.14 now becomes:

$$f_x = -\alpha E T(y,z) + \frac{1}{A} \int_{-c}^c \int_{-1/2 L}^{1/2 L} \alpha E T(y,z) dydz + \frac{y}{I_z} \int_{-c}^c \int_{-1/2 L}^{1/2 L} \alpha E T(y,z) y dydz \quad (\text{A.15})$$

In this two-dimensional case the unbalanced thermal moment M_y about the y axis must also be considered.

$$M_y = \int_{-c}^c \int_{-1/2 L}^{1/2 L} \alpha E T(y,z) z dydz$$

The resulting relief stress becomes

$$(f_x)_b(y) = \frac{M_y z}{I_y} = \frac{z}{I_y} \int_{-c}^c \int_{-1/2 L}^{1/2 L} \alpha E T(y,z) z dydz \quad (\text{A.16})$$

The stress from the external bending moment M_y and M_z can be expressed as follows:

$$f_x = \frac{M_y z}{I_y} + \frac{M_z y}{I_z} \quad (\text{A.17})$$

Thus, by combining Equations A.15, A.16, and A.17, the final stress equation becomes:

$$f_x = -\alpha E T(y,z) + \frac{1}{A} \int_{-c}^c \int_{-1/2 L}^{1/2 L} \alpha E T(y,z) dydz + \frac{y}{I_z} \int_{-c}^c \int_{-1/2 L}^{1/2 L} \alpha E T(y,z) y dydz + \frac{z}{I_y} \int_{-c}^c \int_{-1/2 L}^{1/2 L} \alpha E T(y,z) z dydz + \frac{M_y z}{I_y} + \frac{M_z y}{I_z} \quad (\text{A.18})$$

For the use of numerical integration, Equation A.18 becomes:

$$f_x = -\alpha E T(y,z) + \frac{1}{A} \sum \alpha E a T(y,z) + \frac{y}{I_z} \sum \alpha E a y T(y,z) + \frac{z}{I_y} \sum \alpha E a z T(y,z) + \frac{M_y z}{I_y} + \frac{M_z y}{I_z} \quad (\text{A.19})$$

Where: a = area of small elements in section.

Equation A.19 is modified for stresses above the proportional limit by the use of the Ramberg-Osgood equation as follows:

$$E \text{ becomes } E_S = \frac{E}{1 + \frac{3}{4} (F/F_y)^{n-1}}$$

Where: F = actual stress

F_y = yield stress

n = coefficient dependent on material stress-strain curve

The equation is also modified for buckling by changing the effective area of a buckling element. The following equation is used to modify a :

$$a_{\text{eff}} = a (0.19 + 0.081 \sqrt{F_{\text{CR}}/F})$$

Where: F_{CR} = buckling stress of element.

TABLE A.1 INTERMEDIATE PARAMETERS USED IN CALCULATION OF RADIANT EXPOSURE

Shot	K_1'	T_1	β	$T_2 T_3$	$\frac{Q_{RN}}{Q_I}$	K_4	(1-F)	H_h ft	Visibility statute miles	P_0 mm
Butternut, Normal *	0.5976	0.7118	0.700	0.4604	0.825	0.2804	0.9058	3,000	10	21.4
Butternut, Direct *	0.5976	0.7118	0.700	0.4604	1.060	0.3603	0.9281	3,000	10	21.4
Butternut, Normal †	0.6035	0.7288	0.700	0.4571	1.210	0.3719	1.0586	3,000	10	21.4
Butternut, Direct †	0.5563 †	0.7288	0.700	0.4571	1.350	0.4149	1.0430	3,000	10	21.4
Yellowwood, Normal †	0.5926	0.7210	0.700	0.4798	0.710	0.2478	0.8576	0	—	20.7
Yellowwood, Direct †	0.5926	0.7210	0.700	0.4798	1.000	0.3491	0.8900	0	—	20.7
Magnolia, Normal *	0.6044	0.7429	0.700	0.4670	1.205	0.3725	1.0452	3,000	10	20.0
Magnolia, Direct *	0.6044	0.7429	0.700	0.4670	1.320	0.4080	1.0327	3,000	10	20.0
Magnolia, Normal †	0.6065	0.7513	0.700	0.4770	1.150	0.3679	0.9507	3,000	10	20.0
Magnolia, Direct †	0.6065	0.7513	0.700	0.4770	1.225	0.3919	0.9608	3,000	10	20.0
Walnut, Normal *	0.5194	0.5646	0.700	0.4286	0.330	0.1470	0.6960	3,000	10	21.1
Walnut, Direct *	0.5194	0.5646	0.700	0.4286	0.500	0.2228	0.7445	3,000	10	21.1
Walnut, Normal †	0.6262	0.6669	0.700	0.4534	0.615	0.2480	0.7252	3,000	10	21.1
Walnut, Direct †	0.6262	0.6669	0.700	0.4534	0.770	0.3105	0.7734	3,000	10	21.1

* Aircraft 139467.

† Aircraft 139310.

† Includes a 0.922 factor to correct for gross positioning error.

TABLE A.2 PARAMETER VALUES USED IN CALCULATION OF HEAT CAPACITY, G,
FOR THIN SKINS

	Fuselage Station 210.81	Fuselage Station 248.155	Fuselage Station 33.625	Fuselage Station 389.125	Wing Station 170.0	Wing Station 223.75
Skin material	2024 T4	2024 T4	2024 T4	7075 T6	7075 T6	7075 T6
ρ_s , gm/cm ³	2.77	2.77	2.77	2.77	2.77	2.77
C_{p_s} , cal/gm-°F	0.128	0.128	0.128	0.128	0.128	0.128
b_s , cm	0.0813	0.0813	0.0635	0.0635	0.1626	0.1016
Paint	White MIL-L- 19537	White MIL-L- 19537	White MIL-L- 19537	White MIL-L- 19537	Blue MIL-L- 7178	White MIL-L- 19537
ρ_p , gm/cm ³	1.553	1.553	1.553	1.553	1.610	1.553
C_{p_p} , cal/gm-°F	0.183	0.183	0.183	0.183	0.178	0.183
b_p , cm	0.00508	0.00508	0.00508	0.00508	0.00508	0.00508
G , cal/cm ² -°F	0.0302	0.0302	0.0239	0.0239	0.0591	0.0374

TABLE A.3 COMBINED FLYAWAY AND CONVECTIVE COOLING FACTORS
FOR SELECTED THERMOCOUPLE LOCATIONS

NA, data not available.

Shot	Fuselage Station 210.81	Fuselage Station 248.155	Fuselage Station 333.625	Fuselage Station 389.125	Wing Station 170.0	Wing Station 223.75
Butternut *	0.639	NA	0.628	0.632	NA	NA
Butternut †	0.758	NA	0.740	NA	NA	NA
Koa *	0.437	0.439	0.424	0.430	NA	NA
Koa †	0.502	0.505	NA	0.494	0.533	0.486
Yellowwood †	0.554	0.557	0.541	0.545	0.590	0.539
Magnolia *	0.739	NA	0.724	0.730	NA	NA
Magnolia †	0.687	0.690	0.675	0.679	0.718	0.673
Walnut *	0.437	0.440	0.424	0.429	NA	NA
Walnut †	0.443	0.446	0.431	0.438	0.471	0.428

* Aircraft 139467.

† Aircraft 139310.

TABLE A.4 FLYAWAY FACTORS USED IN THE THERMAL-RESPONSE ANALYSIS

Shot	$(1-F)_{\infty}$	$(1-F)_{10\tau}$
Butternut *	0.906	0.929
Butternut †	1.059	1.044
Koa *	0.761	0.803
Koa †	0.812	0.850
Yellowwood †	0.858	0.889
Magnolia *	1.045	1.034
Magnolia †	0.951	0.964
Walnut *	0.696	0.787
Walnut †	0.725	0.769

* Aircraft 139467. † Aircraft 139310.

TABLE A.5 VALUES USED IN CALCULATION OF HONEYCOMB THERMAL-RESPONSE PARAMETER

Item	Aileron	Flap	Elevator
Faceplate material, aluminum	2024 T4	2024 T4	2024 T4
Faceplate density, gm/cc	2.77	2.77	2.77
Faceplate specific heat, cal/gm-°F	0.128	0.128	0.128
Faceplate thickness, cm	0.0406	0.0406	0.0406
Paint material	MIL-L-19537	MIL-L-19537	MIL-L-19537
Paint density, gm/cc	1.553	1.553	1.553
Paint specific heat, cal/cm-°F	0.183	0.183	0.183
Paint thickness, cm	0.00508	0.00508	0.00508
Adhesive material	HT-424	HT-424	HT-424
Adhesive density, gm/cc	1.395	1.395	1.395
Adhesive specific heat, cal/gm-°F	0.139	0.139	0.139
Adhesive thickness, cm	0.0203	0.0203	0.0203
Total faceplate heat capacity, G, cal/cm ² -°F	0.0198	0.0198	0.0198
Core material, aluminum	5052-H39	5052-H39	5052-H39
Core material density, gm/cc	2.66	2.66	2.66
Core size, inches	1/4 × 0.001	1/4 × 0.001	1/8 × 0.001
Core density, gm/cc	0.0369	0.0369	0.0722
Core thermal conductivity, cal-cm/cm ² -sec-°F	0.00261	0.00261	0.00510
Core specific heat, cal/gm-°F	0.128	0.128	0.128
Core depth, cm	0.391	0.391	0.391
Core heat capacity, G _C , cal/cm ² -°F	0.00184	0.00184	0.00360
Backplate thickness, cm	0.0203	0.0254	0.0203

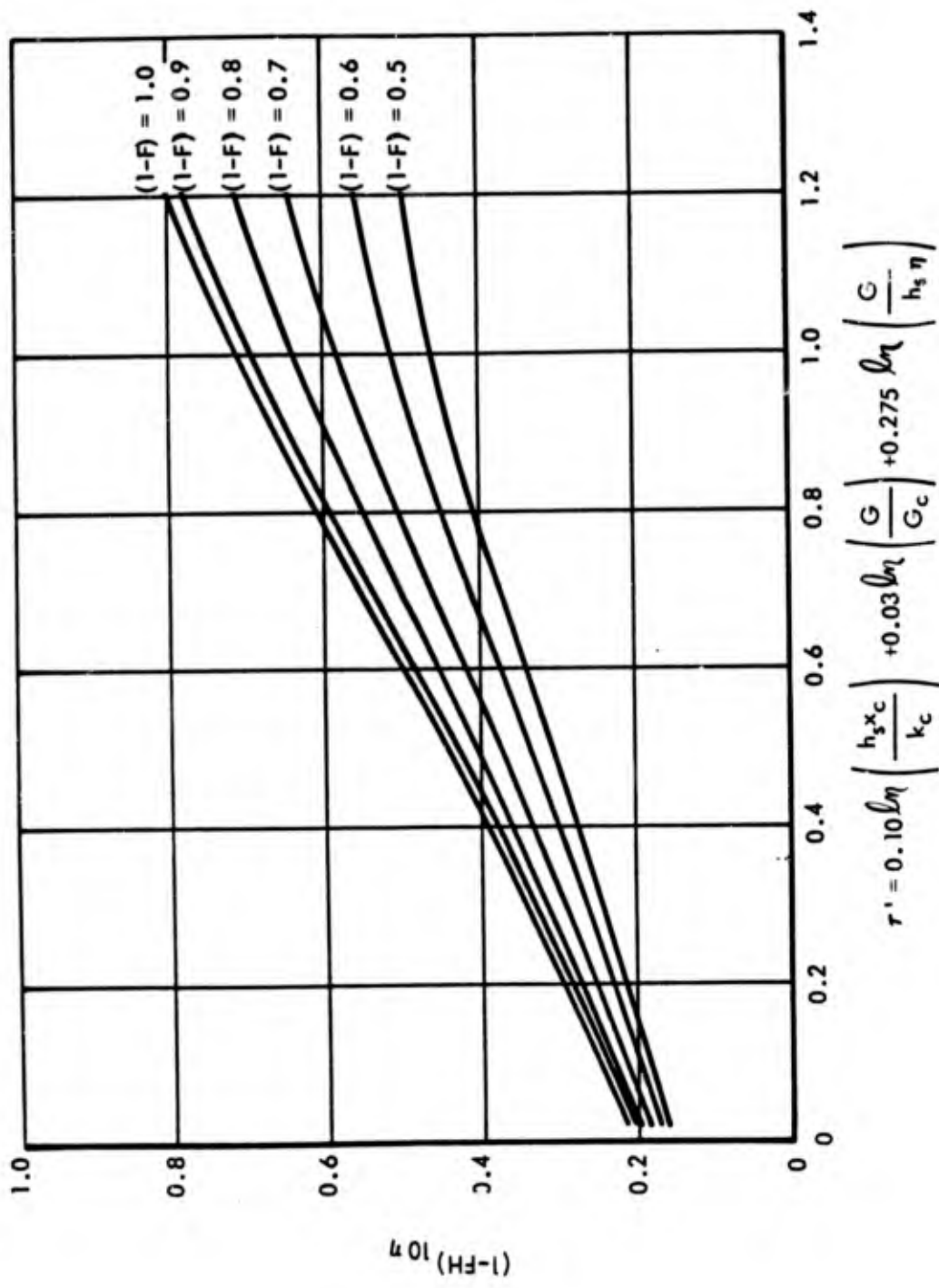


Figure A.1 Combined effect of flyaway and convective cooling on honeycomb faceplate temperature rises.

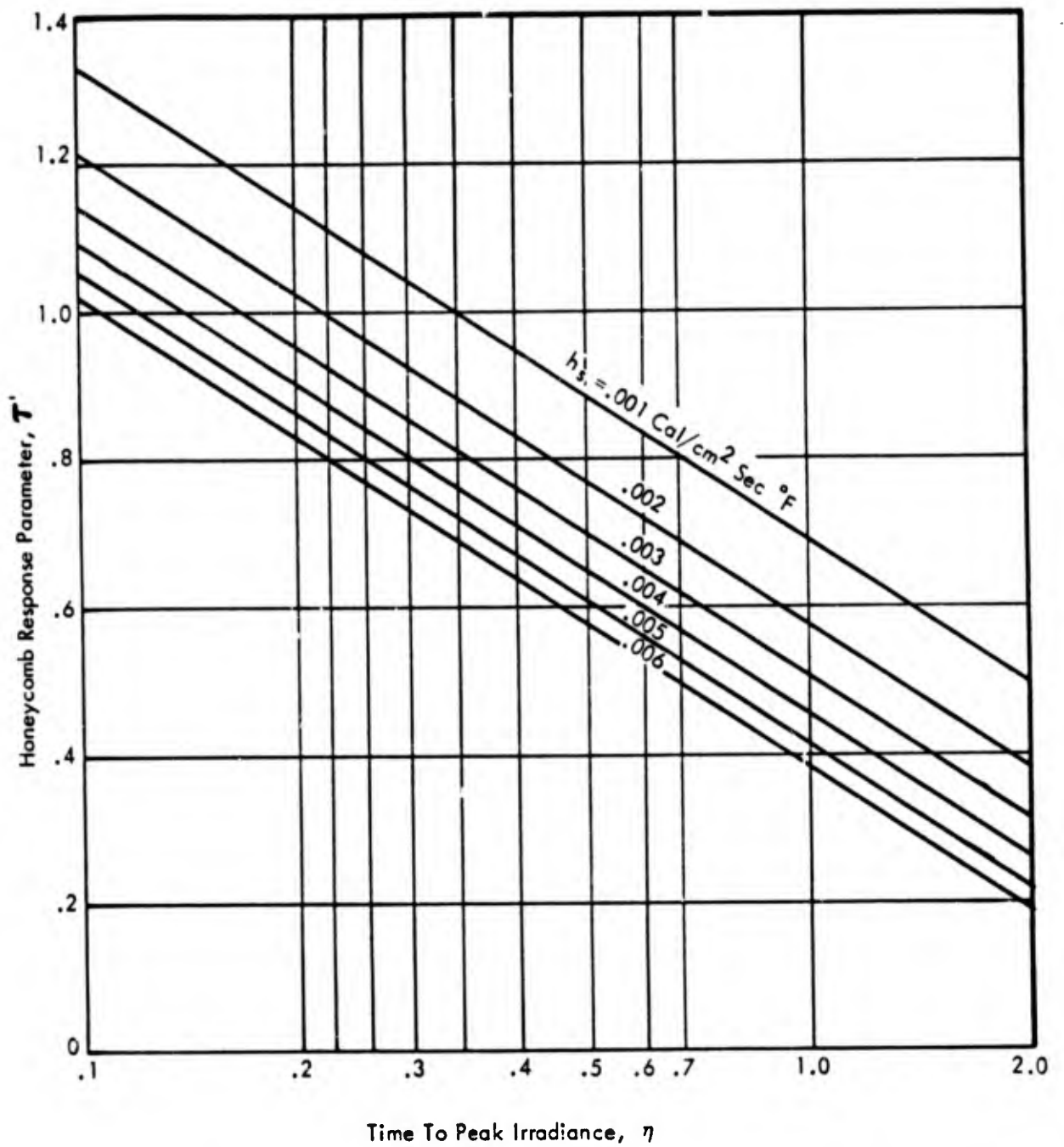


Figure A.2 Thermal-response parameter for aileron and flap honeycomb panels as a function of h_s and η .

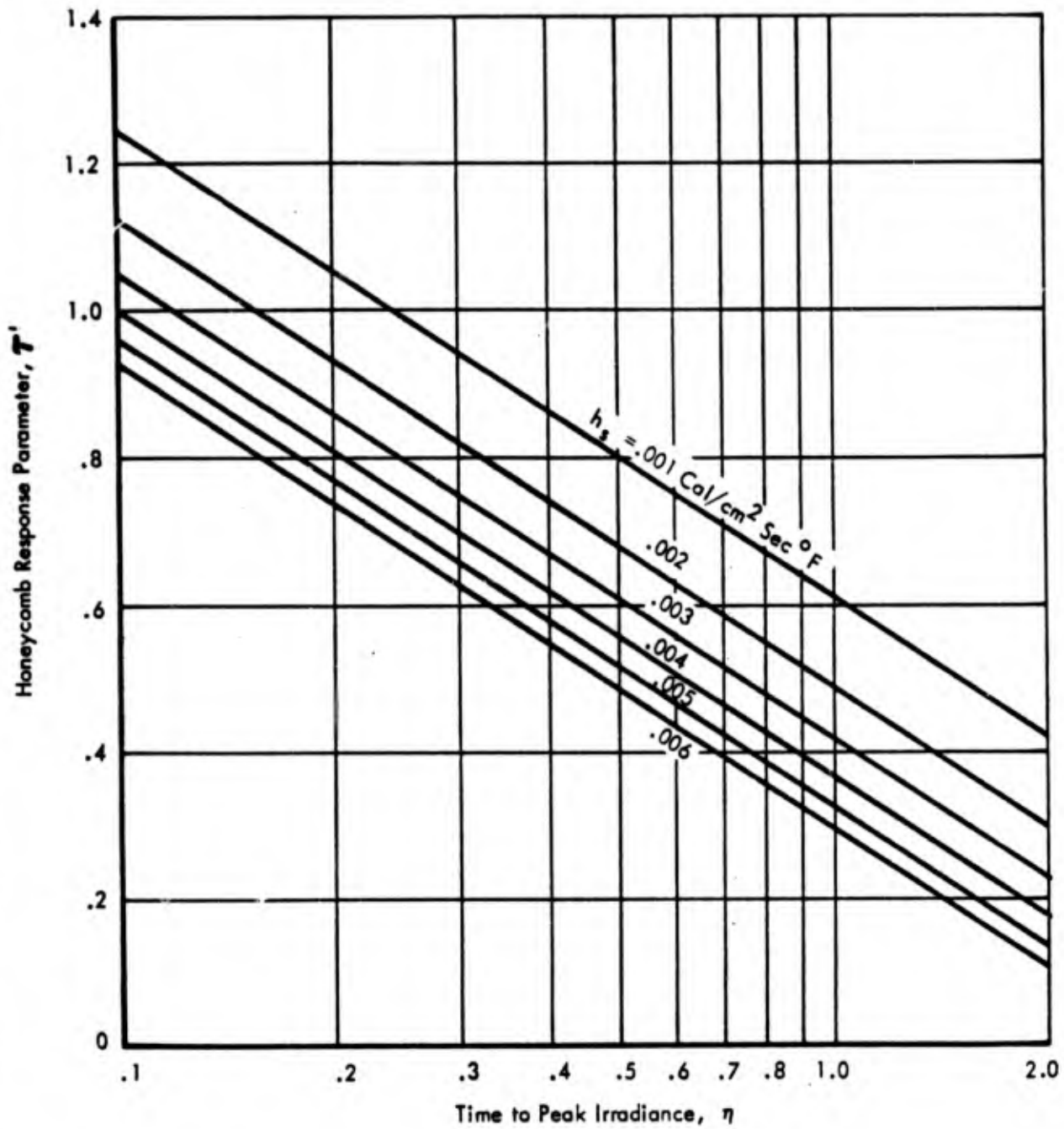


Figure A.3 Thermal-response parameter for elevator honeycomb panel as a function of h_s and η .

Appendix B

NUCLEAR-RADIATION THEORY

B.1 TOTAL NUCLEAR DOSE

The total nuclear dose was computed as the sum of the gamma dose and the neutron dose by the following methods:

$$D_T = D_\gamma + 1.25 W D_n \quad (\text{B.1})$$

Where: D_T = total nuclear dose, rem

D_γ = gamma dose, r

= $f(R_{ac}, \sigma_r, W)$, Reference 5

R_{ac} = slant range from aircraft to burst, yds

σ_r = relative air density between aircraft and burst

W = radiochemical yield, kt

D_n = 1-kt neutron dose, rem

= $f(R_{ac}, \sigma_r)$, Reference 5

B.2 RELATIVE AIR DENSITY

The relative air density was computed using the following relationships (Reference 5):

$$\sigma_r = \frac{P_b - P_{ac}}{H_{ac} - H_b} \quad (25.8) \quad (\text{B.2})$$

Where: σ_r = relative air density

P_b = atmospheric pressure at burst altitude, mb

P_{ac} = atmospheric pressure at receiver altitude, mb

H_{ac} = altitude of receiver, ft

H_b = altitude of burst, ft

Appendix C

BLAST-PARAMETER THEORY

C.1 FREE-STREAM OVERPRESSURE

C.1.1 Free-Stream Peak Overpressure. The method used for computing free-stream peak overpressure is given below. For the surface bursts of Operation Hardtack the effective yield has been assumed to be twice the actual yield. The equations that follow can be used either to find the overpressure at a receiver in space, given the yield, the distances and altitude to the point in question, or to find the slant range from the receiver to the burst point, given the yield, overpressure, and altitude of the receiver.

$$R_1 = \frac{R}{(2W)^{1/3} (p_0/p_{ac})^{1/3}} \quad (C.1)$$

$$\Delta p_1 = f(R_1) \quad (C.2)$$

$$\Delta p = \Delta p_1 (p_{ac}/p_0) \quad (C.3)$$

Where: R_1 = slant range for a 1-kt burst in a homogeneous sea-level atmosphere, ft
 R = slant range to the receiver, ft
 W = yield of weapon, kt
 p_0 = standard atmospheric pressure at sea level, psi
 p_{ac} = ambient atmospheric pressure at receiver altitude, psi
 Δp_1 = peak overpressure for a 1-kt burst in a homogeneous sea-level atmosphere, psi
 Δp = peak overpressure at the receiver altitude, psi

The functional relationship of Equation C.2 is presented in graphical form in Figure 3.29. The 1-kt sea-level overpressures represented are 0.90 of the values obtained from Figure I-14 of Reference 5. An analytical representation for the curve of Figure 3.29, which is an excellent fit for $10^3 \text{ ft} \leq R_1 \leq 10^4 \text{ ft}$, is

$$\Delta p_1 = (3.566/\log_{10} R_1)^{10.6} \quad (C.4)$$

C.1.2 Time History of Overpressure. The time history of free-stream overpressure can be represented by the following expression (Reference 14):

$$\Delta p(t) = \Delta p (1 - t/t^+) e^{-\alpha t/t^+} \quad (C.5)$$

Where: $\Delta p(t)$ = overpressure at time t , psi
 Δp = peak overpressure at receiver altitude, psi
 t = time after shock arrival, sec
 t^+ = positive phase duration, sec
 α = exponential decay parameter, dimensionless

The exponential decay parameter α varies with the ratio of overpressure to pressure at receiver altitude. There is, however, considerable scatter in experimentally determined α 's (References 14 and 15). It was recommended in Reference 14 that an average value of $\alpha = 1/2$ be used. That the average value of $1/2$ is a fairly good representation of α for the early portion of the overpressure decay (near $t/t^+ = 0$) in the range of the test data was confirmed by analysis of the overpressure time histories obtained in Operation Hardtack (Reference 15).

C.2 TIME OF SHOCK ARRIVAL

Utilizing the following scaling laws

$$R = R_1 (2W)^{1/3} (p_0/p_{ac})^{1/3} \quad (C.6)$$

and

$$t_s = t_{s1} (c_0/c_{ac}) (2W)^{1/3} (p_0/p_{ac})^{1/3} \quad (C.7)$$

an equation for the time of arrival of the shock front was derived from an analytical expression for the time of shock arrival versus slant-range curve for a 1-kt burst in a homogeneous sea-level atmosphere from Reference 5. This equation is

$$t_s = \frac{R - 570 (2W)^{1/3} (p_0/p_{ac})^{1/3}}{1,140/(c_0/c_{ac})} \quad (C.8)$$

Where: t_s = time it takes for the shock front to intercept the receiver, sec
 t_{s1} = time of arrival of shock front for a 1-kt burst in a homogeneous sea-level atmosphere, sec
 c_0 = standard velocity of sound at sea level, ft/sec
 c_{ac} = ambient velocity of sound at receiver altitude, ft/sec

Other symbols have been defined in Section C.1.

C.3 SHOCK-FRONT-PROPAGATION VELOCITY

The velocity of propagation of the shock front was computed by the following equation (Reference 5):

$$U = c_{ac} [1 + \frac{5}{7} (\Delta p/p_{ac})]^{1/2} \quad (C.9)$$

where U is the shock-front-propagation velocity in ft/sec and the other symbols are as defined in Sections C.1 and C.2.

C.4 PARTICLE VELOCITY BEHIND THE SHOCK FRONT

C.4.1 Peak Particle Velocity. Peak particle velocity behind the shock front was calculated using the following Rankine-Hugoniot equation from Reference 5:

$$u_m = \frac{\frac{5}{7} c_{ac} \Delta p/p_{ac}}{(1 + \frac{5}{7} \Delta p/p_{ac})^{1/2}} \quad (C.10)$$

where u_m is the peak particle velocity behind the shock front in ft/sec, and the other symbols are as defined in Sections C.2 and C.3.

C.4.2 Time History of Particle Velocity. References 5 and 14 indicate that material velocity decays from its peak value in the same manner that overpressure decays. From Section C.1.2

$$u(t) = u_m (1 - t/t^+) e^{-t/2t^+} \quad (C.11)$$

Where: $u(t)$ = material velocity at time t , ft/sec
 u_m = peak material velocity, ft/sec
 t = time after shock arrival, sec
 t^+ = positive-phase duration, sec

C.5 DENSITY BEHIND THE SHOCK FRONT

C.5.1 Peak Density Behind the Shock Front. The peak density behind the shock front was calculated using the following Rankine-Hugoniot equation from Reference 5:

$$\rho_m = \rho_{ac} \frac{1 + \frac{5}{7} (\Delta p/p_{ac})}{1 + \frac{1}{7} (\Delta p/p_{ac})} \quad (C.12)$$

Where: ρ_m = peak density behind the shock front, slugs/ft³
 ρ_{ac} = ambient density at receiver altitude, slugs/ft³

C.5.2 Time History of Density Behind the Shock Front. Reference 14 indicates that overdensity decay behind the shock front may be represented in the same form as overpressure decay. From Section C.1.2

$$\Delta\rho(t) = \Delta\rho_m (1 - t/t^+) e^{-t/2t^+} \quad (C.13)$$

Where: $\Delta\rho(t) = \rho(t) - \rho_{ac}$ = overdensity behind the shock front at time t after shock arrival, slugs/ft³

$\rho(t)$ = density behind the shock front at time t , slugs/ft³

$\Delta\rho_m = \rho_m - \rho_{ac}$ = peak overdensity, slugs/ft³

C.6 POSITIVE-PHASE DURATION

The positive-phase duration, t^+ , used in the previous equations was determined by the scaling law of Equation C.7 and the 1-kt sea-level positive-phase duration versus range curve of Reference 5.

$$t^+ = t_1^+ (c_0/c_{ac}) (2W)^{1/3} (p_0/p_{ac})^{1/3} \quad (C.14)$$

Where: t^+ = time duration of positive phase, sec

t_1^+ = time duration of positive phase for a 1-kt burst in a homogeneous sea-level atmosphere, sec

and other symbols are as defined in Sections C.1 and C.2. The 1-kt sea-level duration of positive phase, t_1^+ , as a function of scaled range, R_1 , is presented in Figure C.1 (from Reference 5).

C.7 TIME HISTORIES FOR A MOVING RECEIVER

In order to account for the motion of the test aircraft, Equations C.5, C.11, and C.13 were modified by substituting λt for t/t^+ .

$$\lambda = (1 - V_g \cos \beta / U) / t^+ \quad (C.15)$$

Where: V_g = aircraft ground speed, ft/sec

β = shock-wave impingement angle (the angle between the line of flight and the shock-front path), deg

and other symbols were previously defined.

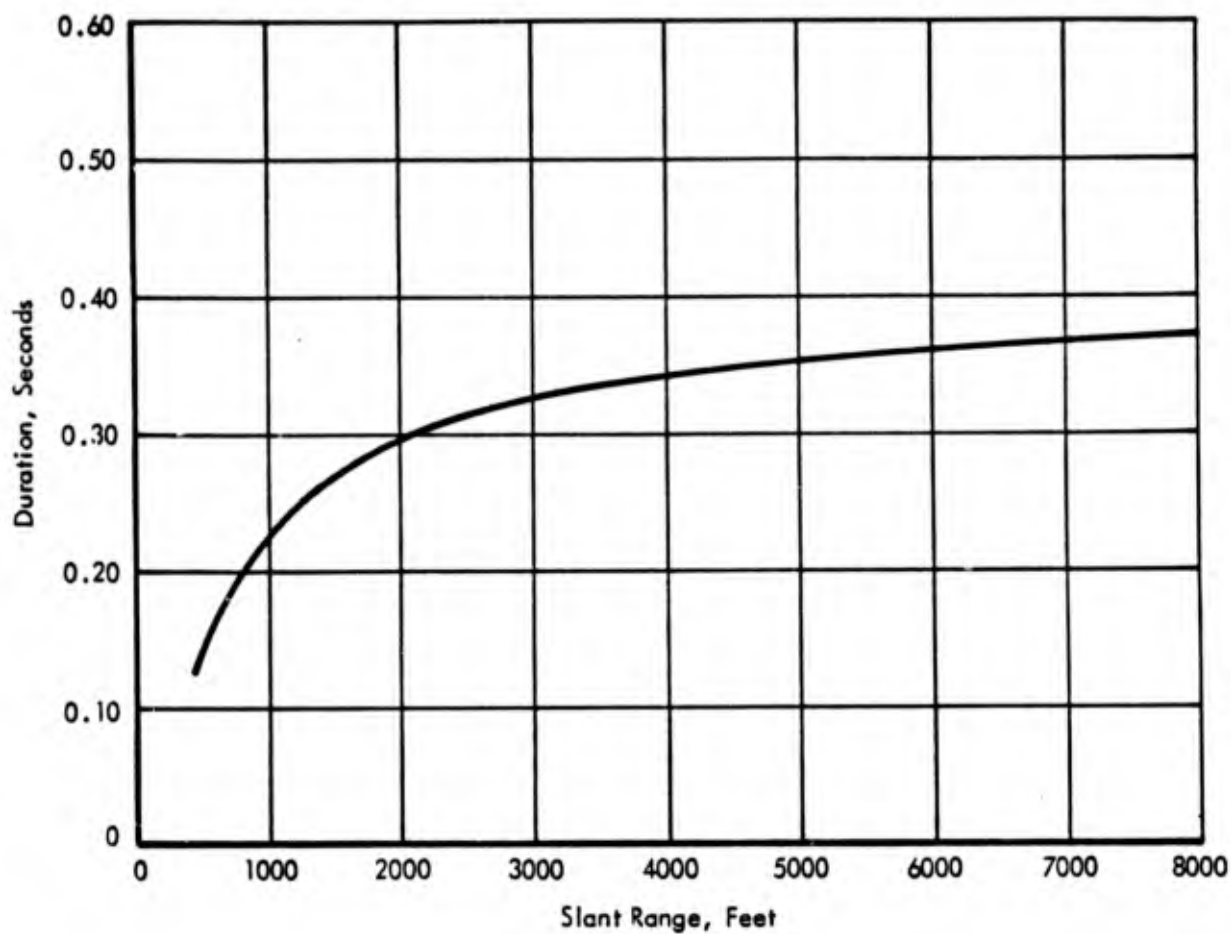


Figure C.1 Free-air duration of positive phase versus slant range for a 1-kt burst in a homogeneous sea-level atmosphere.

Appendix D

DYNAMIC-RESPONSE THEORY

D.1 BASIC CONSIDERATIONS

The purpose of this section is to describe the basic considerations involved in the establishment of the equations that were used to analyze an elastic aircraft in response to a blast wave. As the wave front rapidly envelops the aircraft, the sudden pressure rise and associated material velocity cause dynamic loads of extremely short rise time to be developed. Also, these loads are of sufficient intensity to cause a significant excitation of structural vibrations in combination with deviations in flight path and attitude. Therefore, the problem is in the form of a special type of gust-loading condition in conjunction with a secondary effect due to diffraction of the shock front about the lifting surfaces.

The analysis for this problem represented the dynamic system as two rigid-body degrees of freedom, plunging and pitching, plus three flexural degrees of freedom, the first three symmetrical aircraft vibration modes. The plunging and pitching modes were represented in the form of conventional, longitudinal-stability equations in order that these rigid-body motions could properly influence the structural equations. These structural equations were derived by the application of Lagrange's equations to the normal aircraft vibration modes.

The formulation of the forces which act on the aeroelastic system treat each applied force as arising from several independent causes. These causes can be categorized as follows: (1) blast-wave conditions; (2) rigid-aircraft motions; and (3) structural deformations and velocities. Each of the forces was allowed to act on the entire structure in each of its five degrees of freedom. The manner in which the forces were computed, due to each of these causes, will be individually discussed in the following section.

D.2 DETAILED FORMULATIONS

Each term of the dynamic-response equations, as illustrated below, will be discussed in the following paragraphs.

Plunging Equation:

$$M V_I (\dot{\theta} + \dot{\alpha}) = F_M + F_B$$

Pitching Equation:

$$I \ddot{\theta} = M_M + M_B$$

Structural Equations: ($i = 1, 2, 3$)

$$M_i (\ddot{\xi}_i + g_i \omega_i \dot{\xi}_i + \omega_i^2 \xi_i) = \Xi_{iM} + \Xi_{iB}$$

The fundamental approach, as utilized in the formulation of the dynamic-response equations, is outlined in Reference 16 as a representation of an unrestrained elastic aircraft in terms of normal coordinates by means of Lagrange's equation. The left-hand terms of the plunging and pitching equations, respectively, represent the total aircraft inertial forces acting normal to the flight path and inertial moments acting about the center of gravity. These terms depend directly upon the aircraft-mass characteristics and inertial speed as functions of the rigid-aircraft accelerations. The terms on the left-hand side of the structural equations represent the inertial, damping and elastic properties of the airframe. The first term describes the inertial effect of the generalized mass and is based on the total kinetic energy contained in each normal mode. The second term represents an approximation to a dissipative force as a means of removing energy from the system to simulate structural damping. Treatment of this term is discussed in References 16 and 17. The last term on the left-hand side of the structural equations represents the

effective, elastic, restoring force of the modal system and is based on the total strain energy contained in each normal mode.

The first term on the right-hand side of each equation represents the total effective loading associated with each degree of freedom as induced by both the rigid and flexural motions of the aircraft. The rigid-motion forces, in the plunging and pitching equations, are introduced by the use of experimentally determined longitudinal-stability derivatives. Consequently, the rigid motions are separately treated as angle of attack, angle-of-attack rate, and angle-of-pitch rate. The rigid motions enter the structural equations in a manner which is identical to the treatment of the flexural motions. For these rigid-motion effects, and the influences of the structural deformations and rates, effective angles-of-attack and center-of-pressure are computed from two-dimensional quasi-steady theory as spanwise functions of each lifting surface. These twist distributions are then incorporated in a three-dimensional subsonic Weissinger program which utilizes the Prandtl-Glauert correction for compressibility effects. The resulting load distributions, in conjunction with the chordwise centers of pressure, are then integrated across each lifting surface to permit the linear dependence of each force and moment on the rigid-body and structural coordinates.

The second term on the right-hand side of each equation represents the forces induced by the impinging blast wave. These loadings are treated in two parts: first, the loading induced by the gust field behind the shock front; and second, the loading due to the diffraction of the shock front about the lifting surfaces. The gust loading is attributed entirely to the material velocity behind the shock front. This velocity is considered to have an exponential time history as discussed in Appendix C. The resultant airspeed, as seen by the moving aircraft, depends on the peak material velocity (u_m), initial airspeed (V_0), ground speed (V_g), blast-incidence angle (β), shock-front propagation speed (U), and the characteristic positive phase of the blast wave (t^+). An analytical representation of the resultant airspeed may be written as,

$$V = [V_0^2 + U^2 - 2 V_0 U \cos \beta]^{1/2}$$

Where: $U = u_m (1 - \lambda t) \exp^{-\lambda t/2}$

$$\lambda = (1 - V_g \cos \beta / U) / t^+$$

To briefly describe the development of the gust loading, consider first a typical streamwise section of a lifting surface which experiences impingement of the blast wave. It is known that the quasi-steady circulation (T) is proportional to the product of local angle of attack (α) times the resultant airspeed, which may be written as,

$$T \sim V \alpha \cong U \sin \beta$$

The unsteady two-dimensional lift (l) is then computed from the quasi-steady circulation by use of a superposition integral in conjunction with a Wagner function (ϕ) modified for the effects of compressibility.

$$l \sim V [T \phi(0) - \int_0^S T(S - S') \phi(S') dS']$$

The space-time variable (S) is the number of semichords traveled by the flow as measured relative to the lifting surface, and is therefore influenced by the material velocity. Since exponential representations of the circulation and Wagner function may be used, the integral can be evaluated in analytical form. This permits the analytical formulation of a nondimensional expression (Ψ) for the two-dimensional lift, which is based on the conditions existing immediately behind the shock front. Therefore, this nondimensional lift incorporates the effects of both blast-wave profile and circulatory lift lag.

The next step in the development of the gust loading is to account for the three-dimensional effects of continuous shock impingement on a swept-back lifting surface. This entails the formulation of the quasi-steady load differential (dL), which acts on an infinitesimal streamwise strip of the surface and is proportional to the local chord (c) and section lift-curve slope (C_{l_α}). This infinitesimal portion of the lift represents the load due to a step-function product of the squared resultant airspeed times angle of attack existing immediately behind the shock front.

$$dL \sim c C_{l_\alpha} V(0) u_m \sin \beta [1(t)]$$

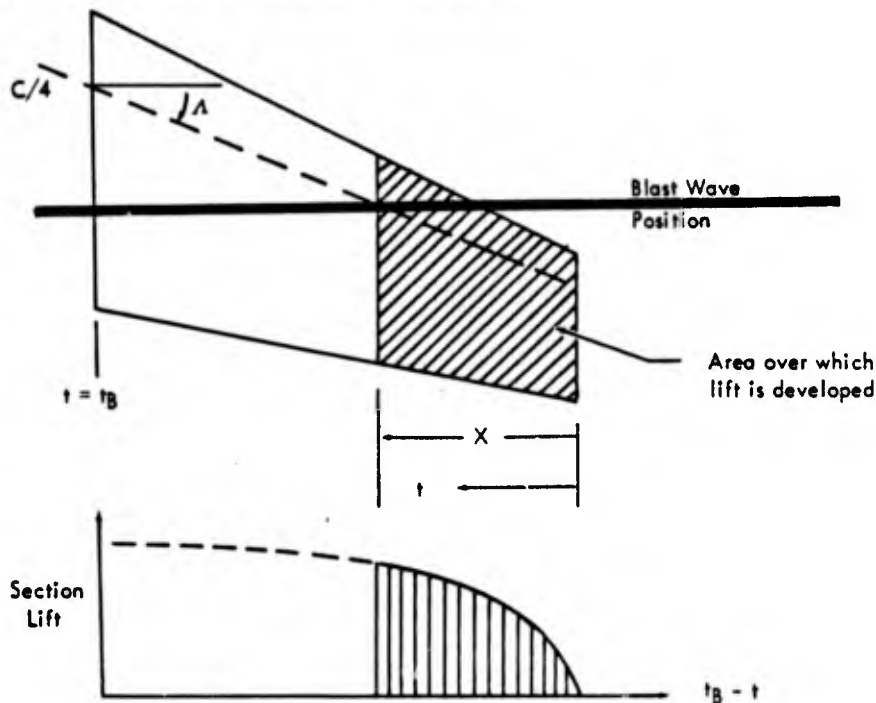
Where: $V(0) = [V_0^2 + u_m^2 - 2 V_0 u_m \cos \beta]^{1/2}$

It is therefore possible to determine the resultant lift as a function of time following initial blast impingement by integration of the lift differential from the tip to the point of intersection of the instantaneous blast-wave position and the quarter-chord line.

$$L \sim V(O) u_m \sin \beta \int_0^x c C_{l\alpha} dt$$

Where: $x = t \left[\frac{(U/\cos \beta) - V_g}{\tan \Lambda} \right]$

This loading configuration may be graphically illustrated as,



Once the integral has been evaluated for the limits of time corresponding to the blast-wave traversal of the surface, it is then operated on by the previously used superposition integral in conjunction with the non-dimensionalized lift expression, ψ .

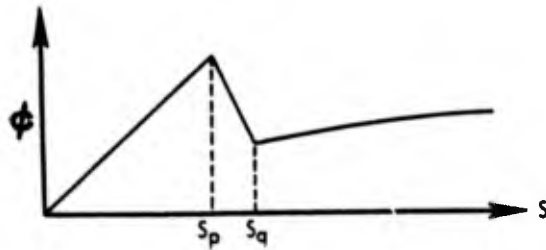
$$L_G = L(t) \psi(O) - \int_0^t L(t-t') \psi'(t') dt'$$

The solution of this final integral (which represents the blast-induced gust loading) incorporates the effects of blast-wave profile, continuous blast impingement, lag in circulatory lift, finite span and compressibility.

The shock-diffraction loading is formulated in a manner similar to the one used in deriving the gust loads above. The only difference appears in the final superposition integral where the non-dimensionalized lift expression, ψ , is replaced by a corresponding non-dimensional expression, Δ , for the two-dimensional shock-diffraction load which is based on an analytical method described in Reference 6;

$$L_D = L(t) \Delta(O) - \int_0^t L(t-t') \Delta'(t') dt'$$

The method of Reference 6 is essentially a semiempirical procedure for establishing the lift-growth function (ϕ) for times during the period of blast-wave impingement. Once the lift-growth function is determined, it need only be multiplied by the quasi-steady value of lift to produce the required three-dimensional section lift. This lift-growth function has the following characteristics:



The analytical representation of this function is written as

$$\phi = \frac{2}{\pi} \frac{\sqrt{1 - M_e^2}}{M_e} (S/S_p) \quad (0 \leq S \leq S_p)$$

$$\phi = \frac{2}{\pi} \frac{\sqrt{1 - M_e^2}}{M_e} \left[1 - \left(\frac{1 - M_e}{2 M_e} \right) (S - S_p) \right] \quad (S_p \leq S \leq S_q)$$

$$\phi = \phi(S) \quad (S_q \leq S)$$

where M_e is an effective Mach number determined by the free-stream Mach number (M_0) and the average lift curve slope ($C_{l_{\alpha, \theta}}$) for the entire planform.

$$M_e = \sqrt{1 + \left(\frac{2 \tau}{M_0 C_{l_{\alpha, \theta}}} \right)^2}$$

The time of peak loading, S_p , corresponds to the arrival of the lower-surface shock wave at the leading edge.

By applying the diffraction-pulse error function (ϵ) as illustrated in Figure 3.63 and making appropriate simplifications to the functionality of the lift-growth relation, the following expression is determined:

$$\phi_{\Delta} = \frac{2}{\epsilon \pi} \frac{\sqrt{1 - M_e^2}}{M_e} (S - S_p) \quad (0 \leq S \leq S_p)$$

$$\phi_{\Delta} = \frac{2}{\epsilon \pi} \frac{\sqrt{1 - M_e^2}}{M_e} \left[1 - \left(\frac{1 - M_e}{2 M_e} \right) (S - S_p) \right] \quad (S_p \leq S \leq S_q)$$

$$\phi_{\Delta} = \phi(O) \quad (S_q \leq S)$$

From this relation the nondimensional expression for the two-dimensional shock-diffraction load was obtained as

$$\Delta(t) = \bar{p}(O) \nabla(O) [\phi_{\Delta}(S) - \phi(O)]$$

where \bar{p} and ∇ are the nondimensional values of density and airspeed immediately behind the undisturbed shock front.

The total loading due to the blast wave is then represented by the sum of the blast-induced gust loading, L_G , and the load associated with the shock-front diffraction about the lifting surfaces, L_D .

Appendix E

INSTRUMENTATION AND SPECIAL EQUIPMENT

E.1 INSTRUMENTATION

Four Model FJ-4 aircraft were instrumented for Operation Hardtack. Two were instrumented with only positioning equipment for use by NASWF during preoperational training. The other two were completely instrumented for the collection of weapon-effect data in Operation Hardtack.

The FJ-4 139292 was fitted only with the X-band beacon and power supply for the preoperational training period. FJ-4 139293 had, in addition, the first prototype RCX-3 converter. The test Aircraft 139310 and 139467 were fully outfitted with positioning equipment as previously described and were further instrumented for the collection of weapon-effect data.

To insure positive radar lock-on by the modified M-33 gun-laying radars, an X-band beacon installation was used. This consisted of a Bendix Aviation, Pacific Division, RBX-2 X-band transmitter-receiver and RPX-1 power supply. In addition, a new component, the RCX-3 superhetrodyne converter, developed by Bendix Pacific, was installed to increase the overall sensitivity of the beacon system by approximately 60 percent.

E.1.1 Primary Instrumentation. The nose compartment, right and left gun bays, and all ammunition bays were used for instrumentation equipment installation. A Type II, 200-gallon wing tank was used for oscillograph and related equipment installation. Two CEC 26-channel oscillographs were mounted in the nose. Two similar oscillographs were mounted in the right wing tank, and a 12-hole photorecorder was installed in the right gun bay.

Figures E.1 through E.4 and their accompanying legends, and Tables E.1 through E.3, show the installation of most of the instrumentation. Tables E.4 through E.6 present the instruments or parameters recorded by the indicated equipment. Because of the limited number of recording channels available for each mission, all data could not be recorded at the same time. For missions during which it was desirable to obtain complete blast-effects data, some thermal data could not be recorded, and vice versa. Tables E.4 through E.6 indicate which instrumentation was recorded for each type of mission.

For all instrumentation except calorimeters and radiometers the calibration curves and constants have been published in Reference 18. Calibration of all the calorimeters and radiometers was accomplished by NRDL.

E.1.2 Comments and Miscellaneous Instrumentation. The following is a list of items of miscellaneous instrumentation and comments concerning the instrumentation in general.

1. Two VDR-5 (16-mm) cameras were installed in the dorsal fairing to photograph left-wing and empennage flexure. Painted stations and flood lighting on the wing and marker lights on the leading edges of the vertical and horizontal stabilizers provided reference indications for observing motions of these structures. The VDR-5 cameras were set for 200 frames/sec.
2. One VDR-5 camera was installed in the tail section of the right wing tank to photograph the fireball. This camera was set for 200 frames/sec.
3. Flood lighting was provided for instrument-panel illumination, controllable from a switch separate from the standard lighting.
4. Strain gages, thermocouples and associated wiring were duplicated wherever possible. Also strain-gage bridges were temperature-compensated wherever possible.
5. Oscillograph paper speed was 28.0 in/sec and the photorecorder speed was 8 frames/sec.
6. A photocell of proper intensity to give a time-zero indication was installed in the fuselage to multiplex with the galvanometer in the voltage-monitor 12-volt power supply.
7. A single record switch was installed to start all recording devices, to close the overpressure valves, and to switch the fuel-quantity indication from the cockpit to the photorecorder.

8. Correlation for the reference galvanometers in the nose oscillographs was provided by the photorecorder unit pulses, and wing-tank VDR-5 camera pulses. Correlation for the tank oscillograph galvanometers was provided by the photorecorder unit pulses and the VDR-5 camera pulses.

9. Ballast was kept to a minimum consistent with the safe center-of-gravity range. All flights were made with the left wing tank mounted and usable. A float switch was provided in the tank to stop any fuel transfer from it automatically and, also, to light an indicator when the weight symmetry level was reached. A switch mounted in the left shroud permitted the pilot to override this automatic cutoff.

10. The left wing tank only was releasable by the normal electrical system; however, the manual emergency release could drop both the left wing fuel tank and the right wing instrumentation tank.

11. In order to maintain uniform or flat frequency response (± 2 percent) from zero to 67 percent of the galvanometer natural frequency, damping networks were provided to obtain 64 percent of critical damping.

12. The galvanometers (Consolidated Electrodynamics Corporation 7-342) used for both the wing-pressure survey transducers and the free-stream overpressure transducers had an undamped natural frequency of 225 cps and a flat frequency response of 135 cps.

E.2 SPECIAL EQUIPMENT

Two items of special equipment were installed on the FJ-4 test aircraft which were not a part of the instrumentation for data collection.

E.2.1 Rotating Navigation Light. A rotating navigation light was installed on each aircraft in order to facilitate the optical acquisition of the aircraft by the M-33 radar crew during predawn hours. This light was a Grimes Manufacturing Company G5790B-A mounted flush on the bottom of the aircraft at Fuselage Station 221, 9 inches to right of centerline, with only the red reflector protruding.

E.2.2 Thermal-Radiation Closure. North American Aviation was required to provide a thermal closure or curtain for the Operation Hardtack FJ-4 aircraft, so that the total radiant exposure inside the cockpit for any shot would not exceed 0.5 cal/cm^2 . The test aircraft were subsequently outfitted with curtains made of aluminized flameproofed cotton duck, Minnesota Mining and Manufacturing Company, Type 81. This curtain was made in three parts: (1) a fixed aft curtain, (2) the canopy hood, and (3) a folding windshield curtain. A double thickness of the curtain material was laced in place aft of the pilot's headrest to form the fixed aft curtain. The canopy hood was constructed of a single thickness of the curtain material with stiffening wires sewn in to prevent sagging. This hood traveled on two aluminum tracks, one aft of the pilot's headrest to overlap the hood with the fixed aft curtain, and one at the forward edge of the movable canopy. An exterior view of the fixed aft curtain and collapsible canopy hood is shown in Figure E.5. The hood was manually operated by the pilot, by use of a curved handle fitted to the edge of the curtain. Actuation of the hood is shown in Figure E.6. In the open position, the hood was collapsed on the left side of the canopy. The windshield curtain was constructed of a single thickness of the curtain material fastened to the instrument panel with aluminum rods sewn into the upper edge. In the open position, this curtain was collapsed on the top of the instrument panel. When closed, the curtain was held in position by spring clips on the upper part of the windshield. An interior view of the windshield curtain in the closed position is shown in Figure E.7. Although not necessarily suitable for operational use, the curtain material provided the protection required.

TABLE E.1 LEGEND FOR FIGURE E.1 FOR STRAIN-GAGE INSTALLATIONS

Number	Approximate Location of Strain Gages	Number	Approximate Location of Strain Gages
1	Fuselage Station 250, left upper longeron	31	Wing Station 153, left
2	Fuselage Station 250, left upper longeron	32	Wing Station 119, left
3	Fuselage Station 250, left upper longeron	33	Rear Spar Station 87
4	Fuselage Station 250, right upper longeron	34	Wing Station 104, left
5	Fuselage Station 250, right upper longeron	35	Wing Rear Spar Station 51, left
6	Fuselage Station 250, right upper longeron	36	Wing Rear Spar Station 63, left
7	Fuselage Station 334.5	37	Wing Rear Spar Station 55, left
8	Fuselage Station 334.5	38	Wing Rear Spar Station 67, left
9	Vertical Stabilizer Station 15.5	39	Wing Station 48, left
10	Vertical Stabilizer Station 46	40	Wing Station 50, left
11	Vertical Stabilizer Station 75	41	Wing Station 40, left
12	Vertical Stabilizer Station 46	42	Fuselage Station 212 Buttock Plane 17.5, left
13	Vertical Stabilizer Station 75	43	Fuselage Station 212 Buttock Plane 17.5, left
14	Vertical Stabilizer Station 89.187	44	Flap Torque Tube, left
15	Vertical Stabilizer Station 93.500	45	Flap Torque Tube, right
16	Vertical Fin Cap	46	Wing Station 36, right
17	Vertical Fin Cap	47	Wing Rear Spar Station 63, right
18	Rudder Hinge Moment	48	Wing Rear Spar Station 51, right
19	Horizontal Stabilizer Station 31, left	49	Wing Rear Spar Station 81, right
20	Horizontal Stabilizer Station 33.750, left	50	Wing Rear Spar Station 91.4, right
21	Horizontal Stabilizer Station 60, left	51	Wing Rear Spar Station 55, right
22	Horizontal Stabilizer Station 31, right	52	Wing Rear Spar Station 66.5, right
23	Horizontal Stabilizer Station 33.750, right	53	Wing Station 11, right
24	Horizontal Stabilizer Hinge Moment	54	Aileron Actuator, right
25	Elevator Hinge Moment	55	Wing Station 173, right
26	Wing Station 173, left	56	Inboard Elevator Hinge, right
27	Aileron Actuator, left	57	Wing Station 63.000 on 21.125-percent chord
28		58	Wing Station 111.000 on 34.750-percent chord
29		59	Wing Station 111.000 on 10.000-percent chord
30		60	Wing Station 131.000 on 41.000-percent chord

TABLE E.2 LEGEND FOR FIGURE E.1 FOR THERMOCOUPLE LOCATIONS

Number	Approximate Location
1	Fuselage Station 81.3
2	Fuselage Station 210
3	Fuselage Station 248.625
4	Fuselage Station 313
5	Fuselage Station 333
6	Fuselage Station 389.375
7	Rudder (Water Plane 69.735)
8	Rudder (Water Plane 69.735)
9	Elevator Station 45.875
10	Elevator Station 45.875
11	Right Flap, Canted Station 59.2
12	Right Flap, Canted Station 59.2
13	Right Wing, Rear Spar Station 87.250
14	Right Wing, Rear Spar Station 138
15	Right Wing, Rear Spar Station 133
16	Wing Station 222, right
17	Wing Station 222, right
18	Aileron Inside Lower, right
19	Blue Panel Wing Station 170
20	Radome
21	Right Flap, Canted Station 59.2
22	Elevator Canted Station 45.875

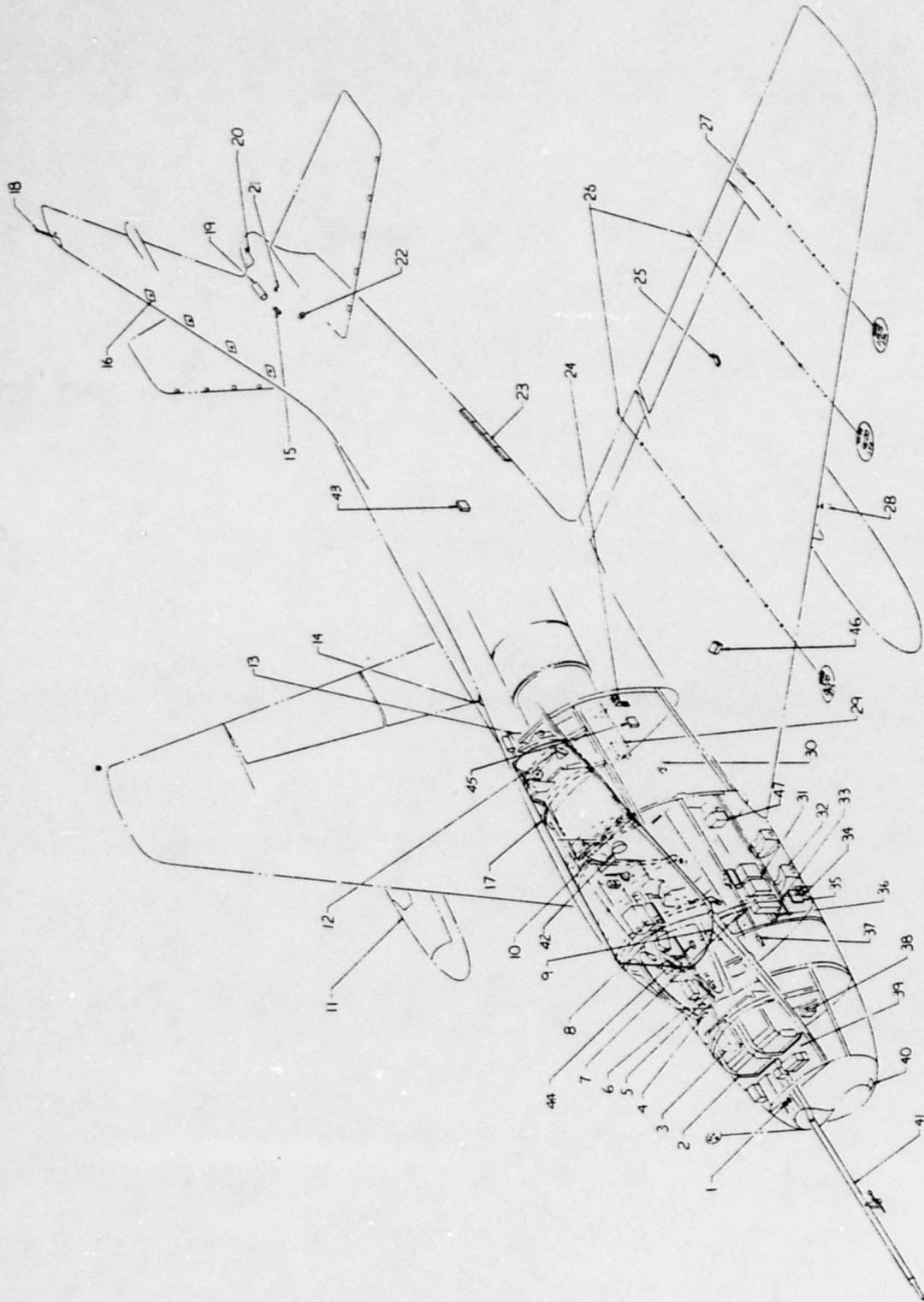


Figure E.2 Perspective instrumentation drawing of FJ-4 aircraft showing miscellaneous installations.

TABLE E.3 LEGEND FOR FIGURE E.2 FOR MISCELLANEOUS INSTALLATIONS

Number	Instrumentation
1	Calorimeter and Radiometer Installation
2	Nose Computer Installation
3	Magnetic Power Supply
4	Station 65 Vertical Gyro
5	Duct Installation of Inverter Cooling
6	Instrument Installation, Right Gun Bay Inverter and Electrical Disconnect Panel
7	Instrument Installation, Doelcam Gyro
8	Instrument Installation, Right Gun Bay
9	Instrument Installation, Power Distribution Unit
10	Electrical Provisions in Forward Fuselage Cell
11	Wing Tank, Modified Type II
12	Instrument Installation, Wing Flex Lights
13	Instrument Installation, Wing and Empennage Flex Camera
14	Instrument Installation, X-Band Beacon Equipment
15	Transmitter Installation, Rudder Position
16	Light Installation, Vertical and Horizontal Stabilizer
17	Hood Installation, Pilot's Thermal Protection
18	Fin Cap X-Band Antenna
19	Converter Installation, Fuselage Station 384.5
20	Antenna, L-Band Recessed Stub APX-6
21	Transmitter Installation, Elevator Twist Inboard
22	Transmitter Installation, Horizontal Stabilizer Position
23	Ballast Installation, Speed Brake Wells
24	Instrument Installation, Accelerometer at Center of Gravity
25	Transmitter Installation, Left and Right Aileron Positions
26	Transducer Installation, Wing-Pressure Survey, Inboard Stations
27	Transducer Installation, Wing-Pressure Survey, Outboard Station
28	Switch Installation, External Fuel Tank Float
29	Panel Assembly Wing Fuel Gauging Relay
30	Capacitor Installation, Forward Fuselage Fuel Cell
32	Ballast Installation, Ammunition Case
33	Instrument Installation, Left Gun Bay
34	Calorimeter and Radiometer Installation, Ammunition Bay Door
35	Ballast Expanded Ammunition Bay
36	Transducer, Fuselage Overpressure Probe
37	Rudder Pedal Force
38	Ballast Assembly and Installation, Gun Stabilizer Mounts
39	Plate Assembly and Installation, Nose Compartment
40	Radome Installation, Dipole Antenna
41	Nose Boom Installation
42	Cockpit Flood Light
43	Fuselage Cooling Transducer
44	Overpressure Transducer
45	Overpressure Transducer
46	Accelerometer Installation at Wheel Well
47	Left Gun Bay Battery

TABLE E.4 RECORDING SUMMARY FOR OSCILLOGRAPHS A AND B

Description of Measurement	Shot-Aircraft-Instrumentation Combinations *	
	FJ-4	FJ-4
	Aircraft 139310	Aircraft 139467
1 Calorimeter, Nose and Up	◇	◇
2 Radiometer, Ammunition Bay	◇	◇
3 Calorimeter, Ammunition Bay	◇	◇
4 Calorimeter, Nose and Right	◇	◇
5 Compressor Inlet Pressure No. 2	◇	◇
6 Temperature, Right Aileron Inside Lower Skin	◇	◇
7 Compressor Inlet Pressure No. 4	◇	◇
8 Overpressure, Upper, 2.416-pct Chord, Wing Station 175.7	CB	◇
9 Overpressure, Lower, 4.5-pct Chord, Wing Station 175.7	CB	◇
10 Overpressure, Upper, 14.5-pct Chord, Wing Station 175.7	CB	◇
11 Overpressure, Lower, 14.5-pct Chord, Wing Station 175.7	CB	◇
12 Overpressure, Upper, 19.3-pct Chord, Wing Station 175.7	CB	◇
13 LH Fuselage Differential Overpressure	—	◇
14 Overpressure, Lower, 19.3-pct Chord, Wing Station 175.7	CB	◇
15 Overpressure, Upper, 26.8-pct Chord, Wing Station 175.7	CB	◇
16 Overpressure, Lower, 26.8-pct Chord, Wing Station 175.7	CB	◇
17 Overpressure, Upper, 38.4-pct Chord, Wing Station 175.7	CB	◇
18 Overpressure, Lower, 38.4-pct Chord, Wing Station 175.7	CB	◇
19 Overpressure, Upper, 50-pct Chord, Wing Station 175.7	CB	◇
20 Overpressure, Lower, 50-pct Chord, Wing Station 175.7	CB	◇
21 Overpressure, Upper, 72-pct Chord, Wing Station 175.7	CB	◇
22 Overpressure, Lower, 72-pct Chord, Wing Station 175.7	CB	◇
23 Rate of Roll	CB	◇
24 Rate of Pitch	CB	◇
25 Rate of Yaw	CB	◇
26 Voltage Monitor and Photocell	CB	◇
27 Temperature, Tailpipe	◇	◇
28 Temperature, Right Elevator, Inside Lower Skin	◇	◇
30 Temperature, Wing Station 142, Inner Lower Skin	◇	◇
31 Temperature, Right Elevator, Inside Upper Skin	◇	◇
32 Temperature, Nose Radome	◇	◇
33 Temperature, Compressor Inlet	◇	◇
34 Airspeed	◇	◇
35 Altitude	◇	◇
36 Elevator Position	◇	◇
37 Nose Differential Overpressure	◇	◇
38 Lateral Accelerometer	◇	◇
39 Lateral Accelerometer	◇	◇
40 Skin Temperature, Bottom Centerline, Station 169	◇	◇
41 Horizontal Stabilizer Position	◇	◇
42 Angle of Yaw	◇	◇
43 Normal Accelerometer	◇	◇
44 Angle of Bank	◇	◇
45 Angle of Pitch	◇	◇
46 Skin Temperature, Bottom Centerline, Station 331	◇	◇
47 Stabilizer Actuator Hinge Moment	◇	◇
49 Angle of Attack	◇	◇
49 Compressor Inlet Pressure No. 3	◇	◇
50 Compressor Discharge Pressure	◇	◇
51 Compressor Pressure at Station 250	◇	◇
52 Temperature, Tail Bumper Bungee Door	◇	◇
53 Temperature, Tail Bumper Bungee Door	RW	◇
54 Compressor Pressure at Station 160	◇	◇
55 Normal Accelerometer, Wing, CF1-277	◇	◇
56 Temperature, Rudder Splitter Plate Inside Right Skin	KYMTRW	—
57 Temperature, Inside ARA-25 Antenna Cover	KYMTRW	—
58 Temperature, Right Outer Wing Panel, Lower Skin, Inner Surface	KYMTRW	—
59 Temperature, Blue Panel, Right, Outer Wing	KYMTRW	—
60 Temperature, Right Flap Inside Upper Skin	KYMTRW	—
61 Temperature, Right Aileron Inside Lower Skin	KYMTRW	—
62 Calorimeter, Tank, White Paint	KYMTRW	—
63 Temperature, Wing Station 140, Inner Lower Stiffener	CBK	—
64 Temperature, Right Flap Inside Lower Skin	KYMTRW	—
65 Compressor Pressure No. 1	KYMTRW	—
66 Compressor Pressure No. 2	KYMTRW	—
67 Compressor Pressure No. 5	KYMTRW	—
68 Tailpipe Total Pressure	KYMTRW	—
69 Temperature, Skin, Bottom Centerline, Station 250	KYMTRW	—
70 Temperature, Right Flap Lower Upper Skin Upper Surface	KYMTRW	—
71 Temperature, Right Elevator Lower Upper Skin Upper Surface	KYMTRW	—

* First letter of shot name indicates for which shots instrumentation was active, except ◇ indicates instrumentation active for all shots.

TABLE E.5 RECORDING SUMMARY FOR OSCILLOGRAPHS C AND D

Description of Measurement	Shot-Aircraft-Instrumentation Combinations *	
	FJ-4	FJ-4
	Aircraft 139310	Aircraft 139467
1 Wing Bending, Left Root, Station 17.5	◇	◇
2 Wing Bending, Left Spar, Station 91.4	◇	C
3 Wing Bending, Left Outer Panel Root, Station 173	◇	◇
4 Wing Shear, Left Front Outer Spar, Inboard Station 56.9	◇	◇
5 Wing Shear, Left Rear Spar, Outboard Station 60.4	◇	◇
6 Overpressure, Upper, 0.37-pct Chord, Wing Station 82	CBRW	◇
7 Overpressure, Lower, 2.0-pct Chord, Wing Station 82	CBRW	◇
8 Overpressure, Upper, 9.7-pct Chord, Wing Station 82	CBRW	◇
9 Overpressure, Lower, 9.7-pct Chord, Wing Station 82	CBRW	◇
10 Overpressure, Upper, 18.2-pct Chord, Wing Station 82	CBRW	◇
11 Overpressure, Lower, 18.2-pct Chord, Wing Station 82	CBRW	◇
12 Overpressure, Upper, 26.2-pct Chord, Wing Station 82	CBRW	◇
13 Overpressure, Lower, 26.2-pct Chord, Wing Station 82	CBRW	◇
14 Overpressure, Upper, 36.7-pct Chord, Wing Station 82	CBRW	◇
15 Overpressure, Lower, 36.7-pct Chord, Wing Station 82	CBRW	◇
16 Overpressure, Upper, 30.4-pct Chord, Wing Station 82	CBRW	◇
17 Overpressure, Lower, 30.4-pct Chord, Wing Station 82	CBRW	◇
18 Overpressure, Upper, 65.3-pct Chord, Wing Station 82	CBRW	◇
19 Overpressure, Lower, 65.3-pct Chord, Wing Station 82	CBRW	◇
20 Wing Bending, Right Root, Station 36.5	◇	◇
21 Wing Bending, Left, Station 68, 21.125-pct Chord	◇	◇
22 Wing Bending, Left, Station 111.2, 34.75-pct Chord	◇	◇
23 Wing Bending, Left, Station 111.2, 40-pct Chord	◇	◇
24 Wing Bending, Left, Station 131.1, 41-pct Chord	◇	◇
25 Wing Shear, Left Front Spar Inboard at Station 105	◇	◇
26 Horizontal Stabilizer Bending, Left, Station 33	CBRW	◇
27 Horizontal Stabilizer Bending, Left, Station 60	KYMT	◇
28 Calorimeter, Tank Hot Reference	◇	◇
29 Calorimeter, Tank Internal Reference	◇	◇
30 Radiometer, Tank	◇	◇
31 Wing Shear, Left Front Spar Inboard Station 153	◇	◇
32 Wing Shear, Left Front Spar, Inboard of Butt Plane 48	◇	◇
33 Wing Shear, Left Aft Spar, Inboard of Station 105	◇	◇
34 Wing Bending, Right Root, Station 17.5	◇	◇
35 Wing Bending, Right Outer Wing Panel, Station 173	◇	◇
36 Horizontal Stabilizer Bending, Right, Station 33	◇	◇
37 Wing Bending, Right Rear Spar, Station 91.4	◇	◇
38 Overpressure, Upper, 1.70-pct Chord, Wing Station 141	◇	◇
39 Overpressure, Lower, 1.70-pct Chord, Wing Station 141	◇	◇
40 Overpressure, Upper, 12.5-pct Chord, Wing Station 141	◇	◇
41 Overpressure, Lower, 12.5-pct Chord, Wing Station 141	◇	◇
42 Overpressure, Upper, 17.2-pct Chord, Wing Station 141	◇	◇
43 Overpressure, Lower, 17.2-pct Chord, Wing Station 141	◇	◇
44 Overpressure, Upper, 22.0-pct Chord, Wing Station 141	◇	◇
45 Overpressure, Lower, 22.0-pct Chord, Wing Station 141	◇	◇
46 Overpressure, Upper, 33.9-pct Chord, Wing Station 141	◇	◇
47 Overpressure, Lower, 33.9-pct Chord, Wing Station 141	◇	◇
48 Overpressure, Upper, 51.7-pct Chord, Wing Station 141	◇	◇
49 Overpressure, Lower, 51.7-pct Chord, Wing Station 141	◇	◇
50 Overpressure, Upper, 61.2-pct Chord, Wing Station 141	◇	◇
51 Overpressure, Lower, 61.2-pct Chord, Wing Station 141	◇	◇
52 Voltage Monitor	◇	◇
53 Calorimeter, Cockpit	◇	◇
54 Photocell	KYMT	—
55 RH Fuselage, Differential Overpressure	KYMT	—
56 RH Aileron, Hinge Moment	KYMT	—
57 Fin Bending, Vertical Station 15	KYMT	—
58 RH Flap, Hinge Moment	KYMT	—
59 Horizontal Stabilizer Bending, Left, Station 60	KYMT	—
60 Wing Shear, Left Front Spar, Outboard Station 56.9	KYMT	—
61 Wing Shear, Right Front Spar Web, Inboard Station 56.9	KYMT	—
62 Wing Shear, Right Rear Spar, Outboard Station 60.4	KYMT	—
63 Wing Shear, Right Rear Spar, Inboard Station 60.4	KYMT	—
64 Wing Shear, Right Front Spar, Inboard Station 105	KYMT	—
65 Wing Shear, Right Rear Spar, Inboard Station 105	KYMT	—
66 Wing Shear, Right Front Spar Web, Outboard Station 56.9	KYMT	—
67 Wing Shear, Left Rear Spar, Inboard Station 60.4	KYMT	—

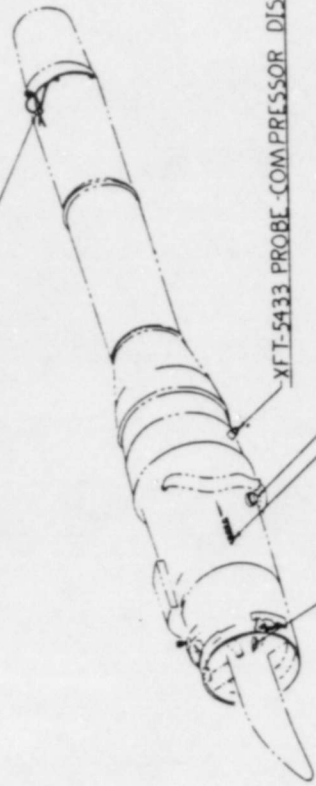
* First letter of shot name indicates for which shots instrumentation was active, except ◇ indicates instrumentation active for all shots.

TABLE E.6 RECORDING SUMMARY FOR PHOTORECORDER

Applies to both test aircraft for all shots.

Number	Description
1	Knotmeter, nose boom
2	Altimeter, nose boom
3	Tachometer (rpm)
4	Left-wing fuel quantity
5	Magnetic compass
6	Outside-air temperature
7	Right-wing fuel quantity
8	Fuel flow
9	Fuel temperature at flow meter
10	Throttle position
11	Fuel counters, fuel used
12	Camera frame counter
13	Clock
14	Fuel inlet pressure

209-75334-201 INSTRUM INSTL-TAIL PIPE TOTAL TEMP & PRESS (REF)

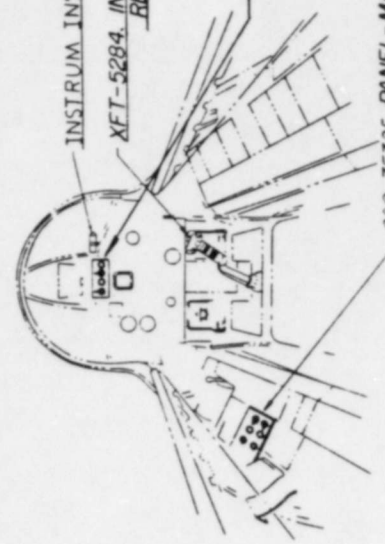


XFT-5433 PROBE-COMPRESSOR DISCHARGE PRESSURE ASSY OF (REF)

209-75510 XMTR INSTR-REVERE FUEL FLOW (INSTRUM)(REF)

209-75733 INSTRUM INSTL-POWER PLAN

XFT-5432 PROBE COMPRESSOR INLET PRESSURE & TEMP ASSY OF (REF)



INSTRUM INSTL-COCKPIT RADIOMETER (REF)

XFT-5284 INSTRUMENTATION STICK & GRIP & INSTRUMENTATION
REMOTE CONTROL (REF)

COCKPIT FLOODLIGHT CONTROL

INSTRUMENTATION RECORD INDICATOR

EMERGENCY DROP TANK FUEL TRANSFER SWITCH

209-75725 PANEL-MASTER INSTRUM CONTROL ASSY & BEACON POWER SWITCH (REF)

Figure E.4 Perspective drawing showing instrumentation of engine and cockpit of FJ-4 aircraft.

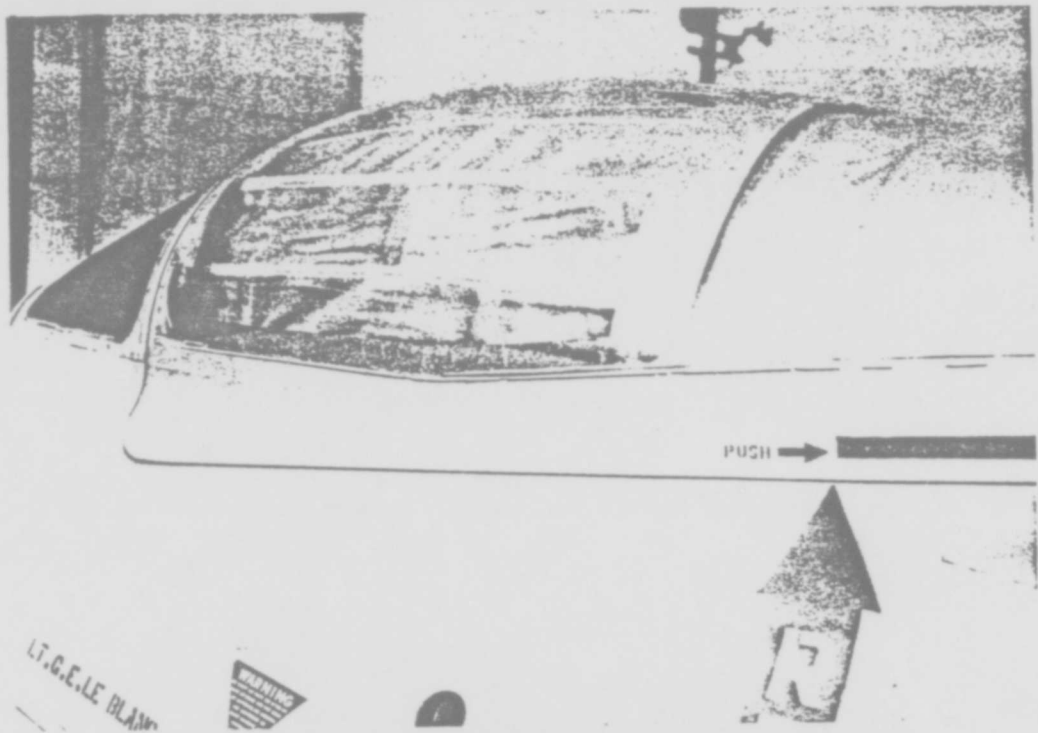


Figure E.5 Exterior view of fixed aft curtain and collapsible canopy hood.



Figure E.6 Actuation of the collapsible canopy hood.

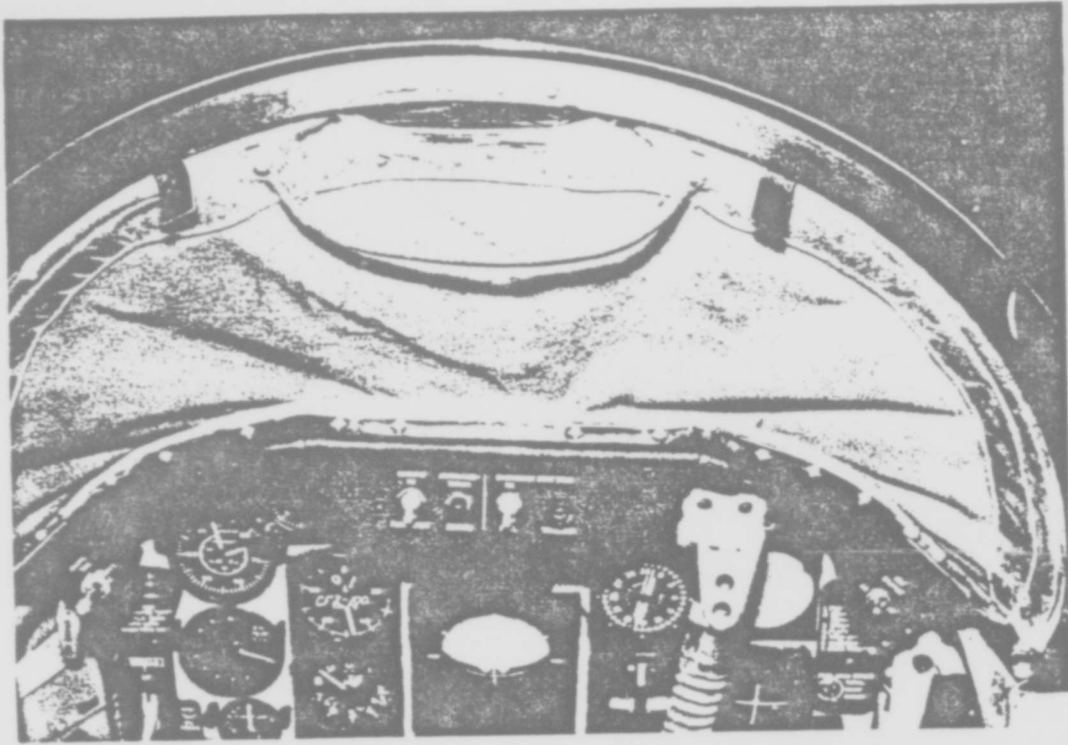


Figure E.7 Interior view of windshield curtain in the closed position.

Appendix F

REDUCED THERMAL DATA

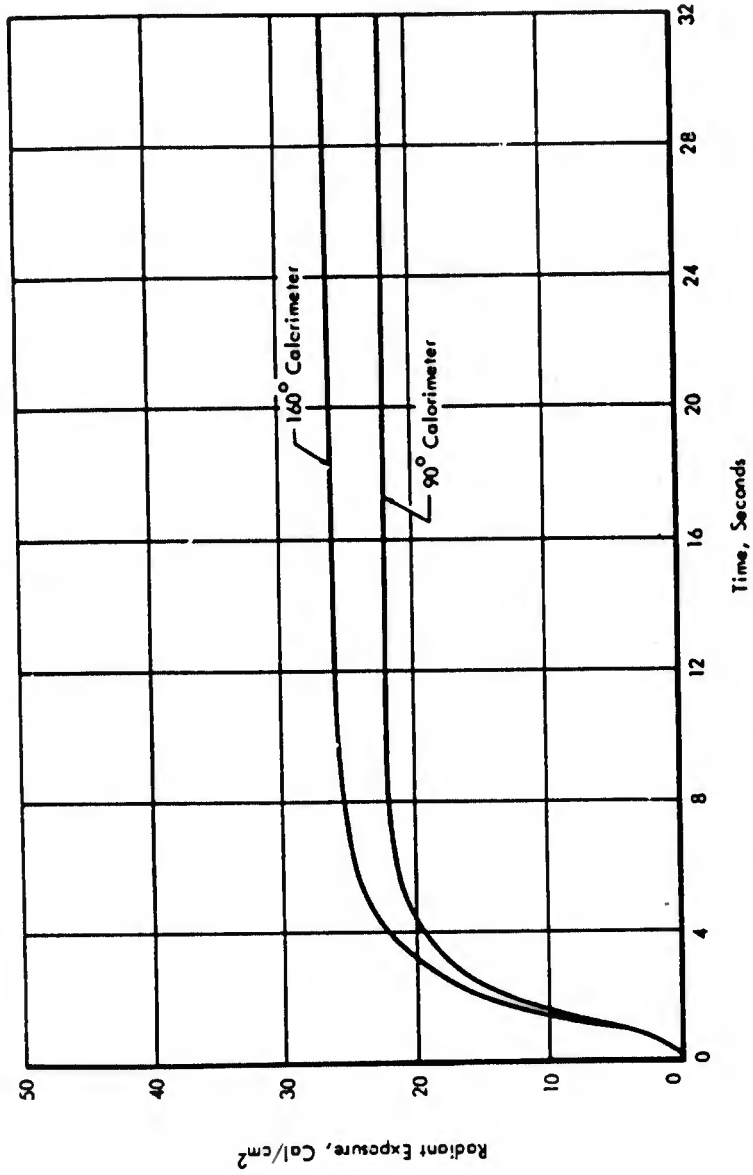


Figure F.13 Measured radiant exposure taken from direct 90° and 160° calorimeters, Aircraft 139467, Shot Koa.

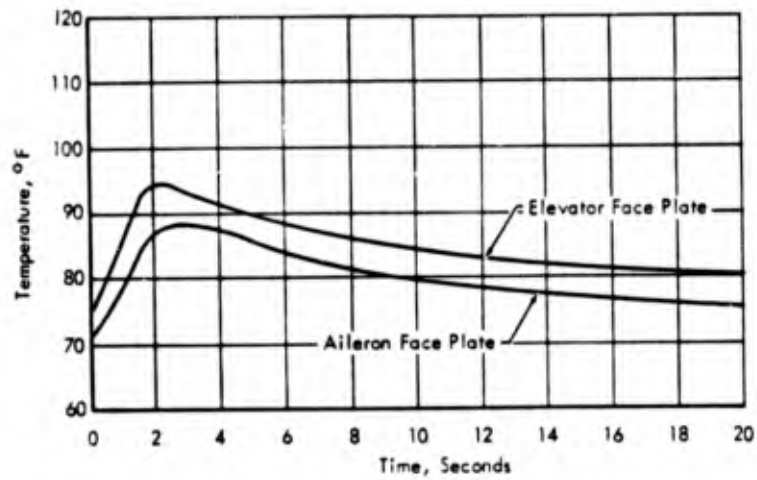
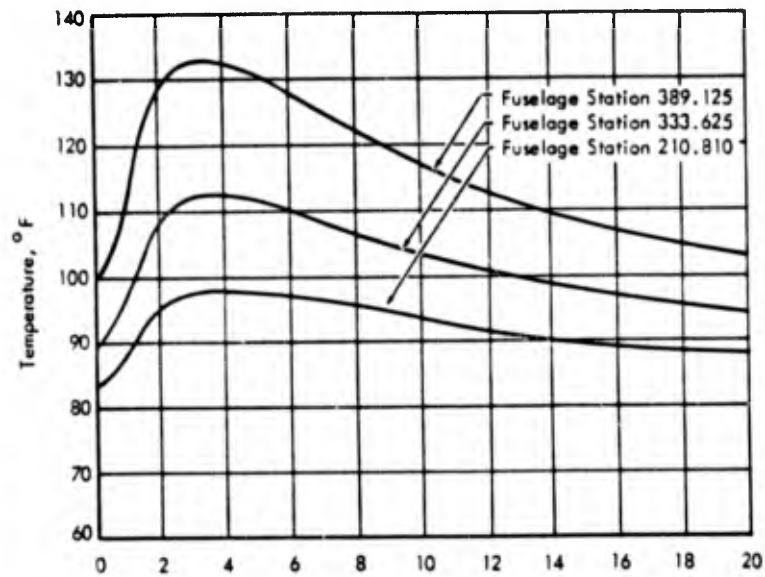


Figure F.14 Measured temperature-time histories of selected thermocouple locations, Aircraft 139467, Shot Koa.

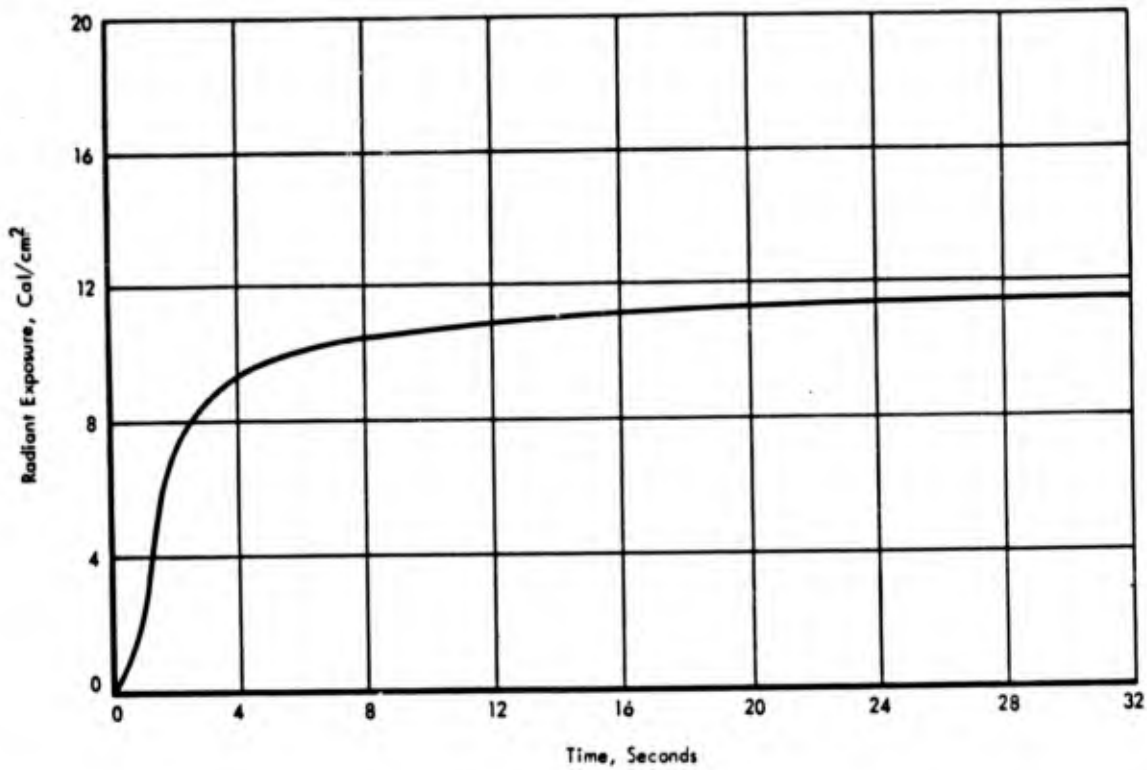


Figure F.15 Measured radiant exposure taken from normal 160° calorimeter, Aircraft 139310, Shot Koa.

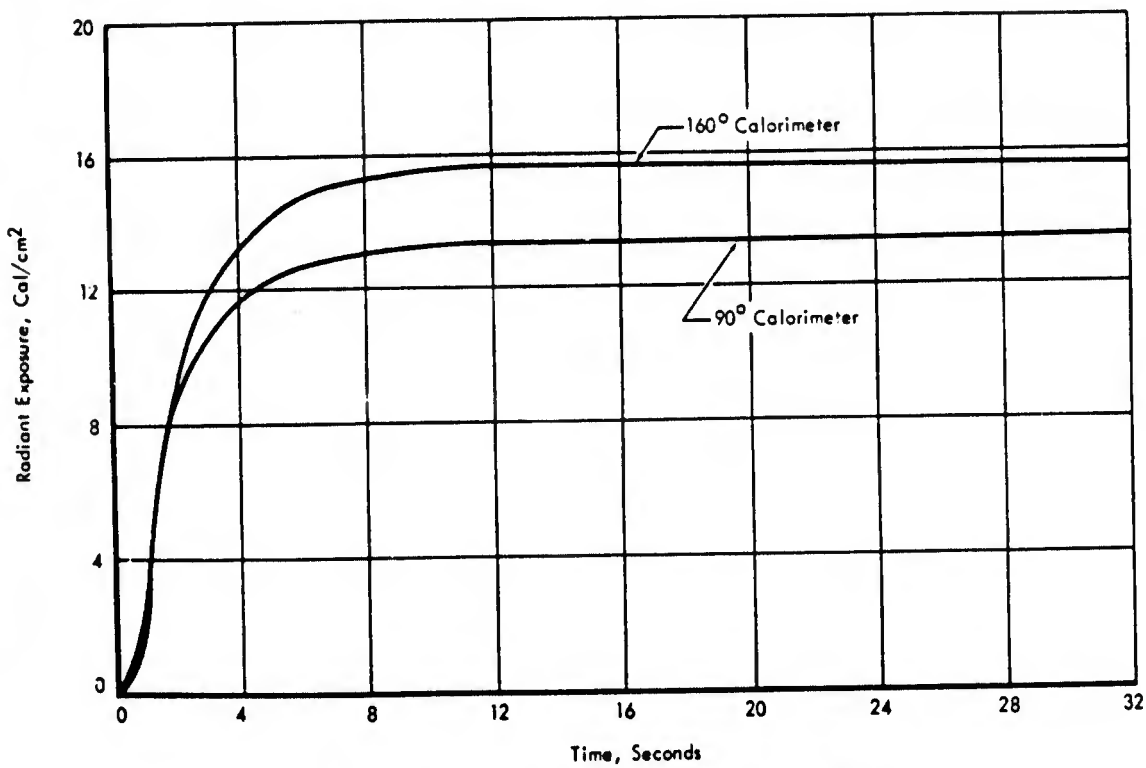


Figure F.16 Measured radiant exposure taken from direct 90° and 160° calorimeters, Aircraft 139310, Shot Koa.

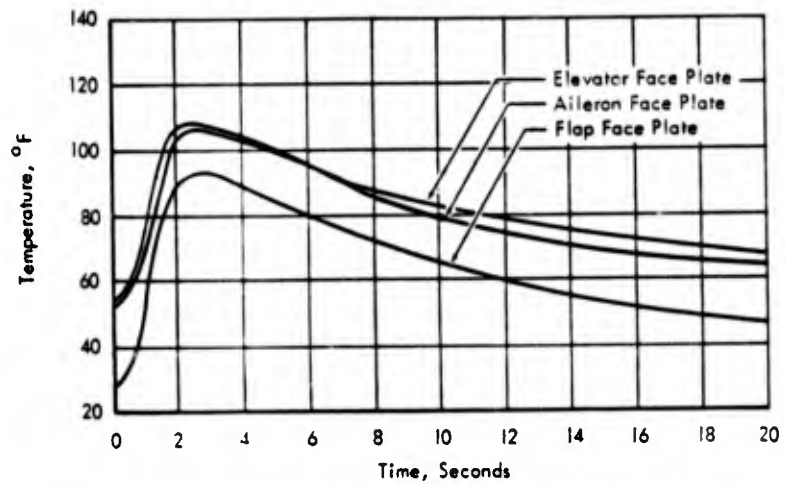
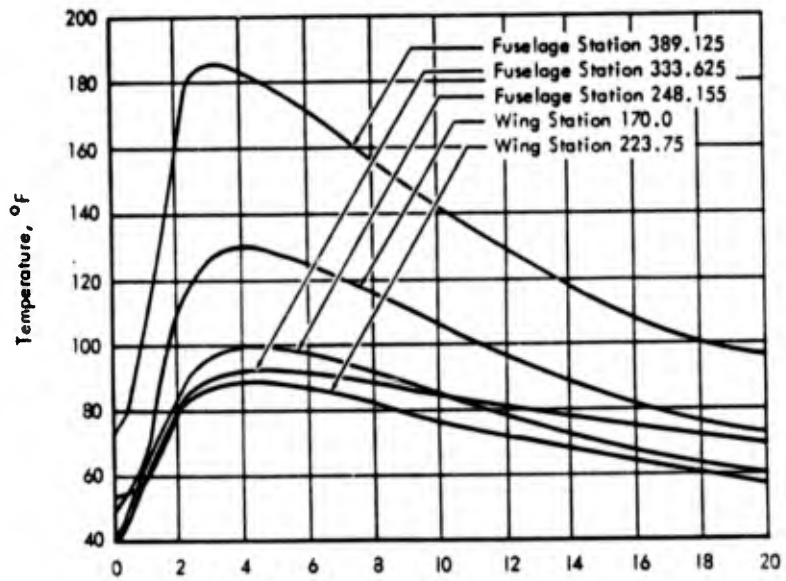


Figure F.17 Measured temperature-time histories of selected thermocouple locations, Aircraft 139310, Shot Koa.

Appendix G

ENGINE-RESPONSE DATA

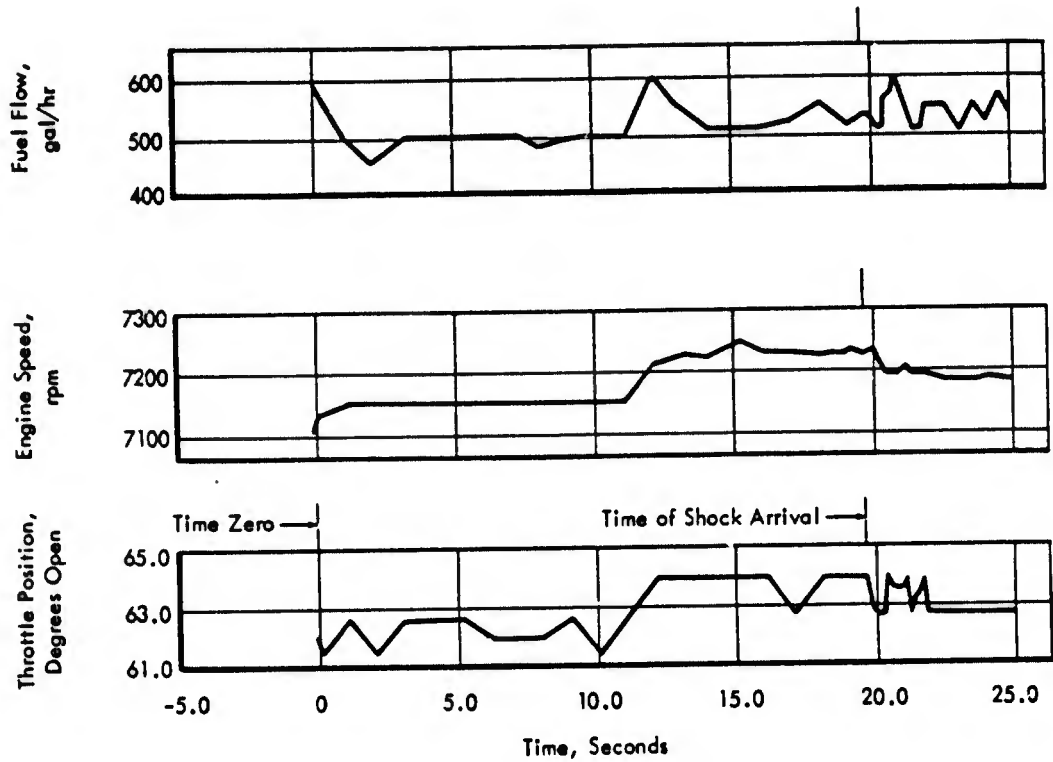


Figure G.1 Throttle position, engine speed and fuel flow for Aircraft 139467, Shot Koa.

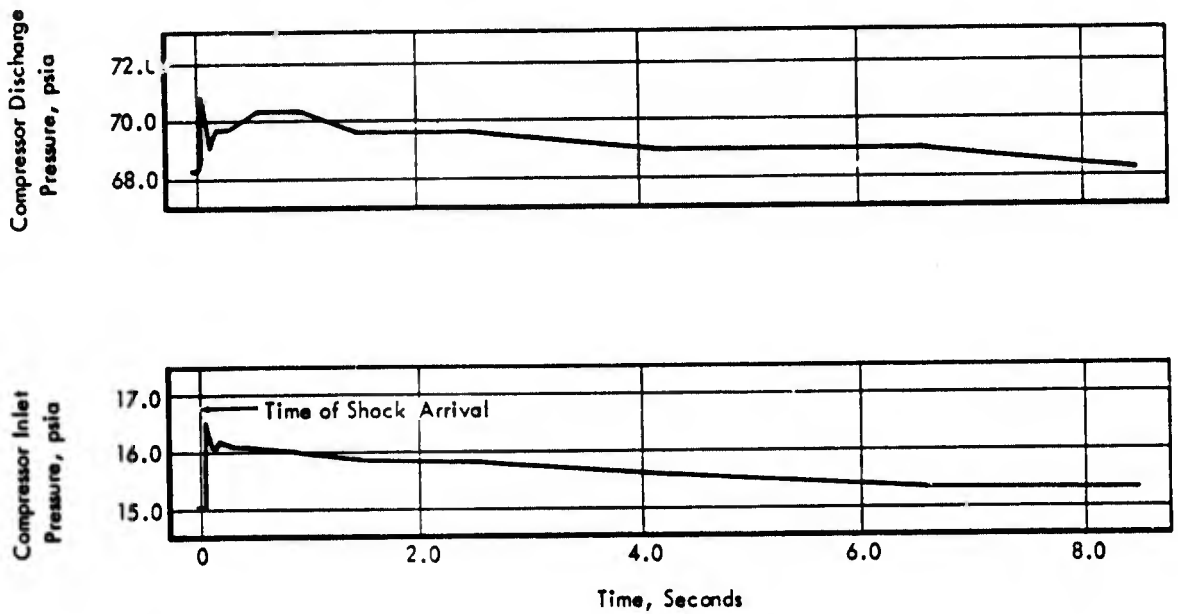


Figure G.2 Compressor inlet and discharge pressures for Aircraft 139467, Shot Koa.

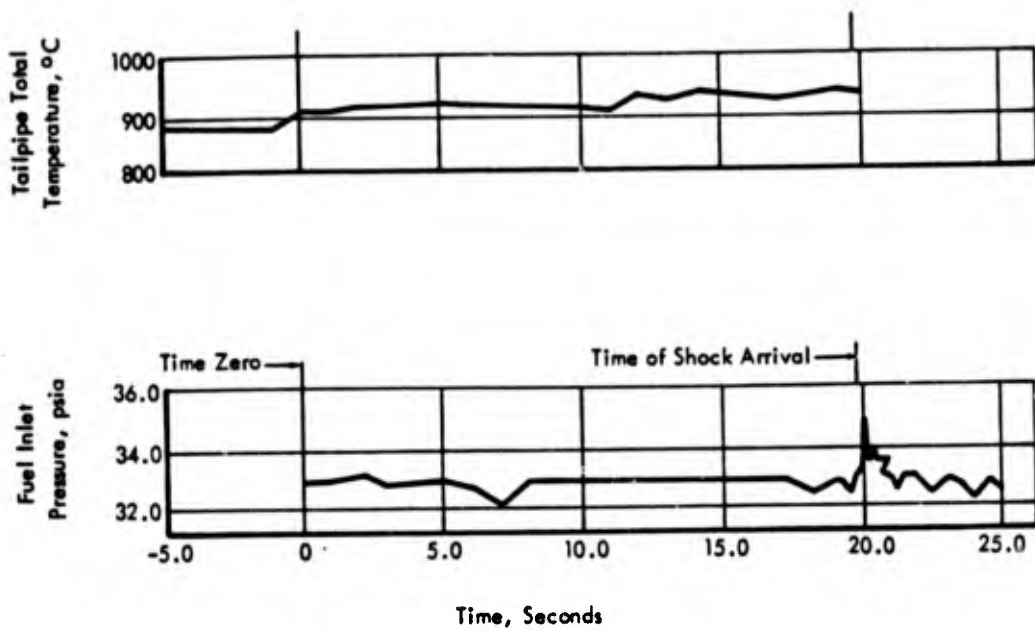


Figure G.3 Fuel inlet pressure and tailpipe total temperature for Aircraft 139467, Shot Koa.

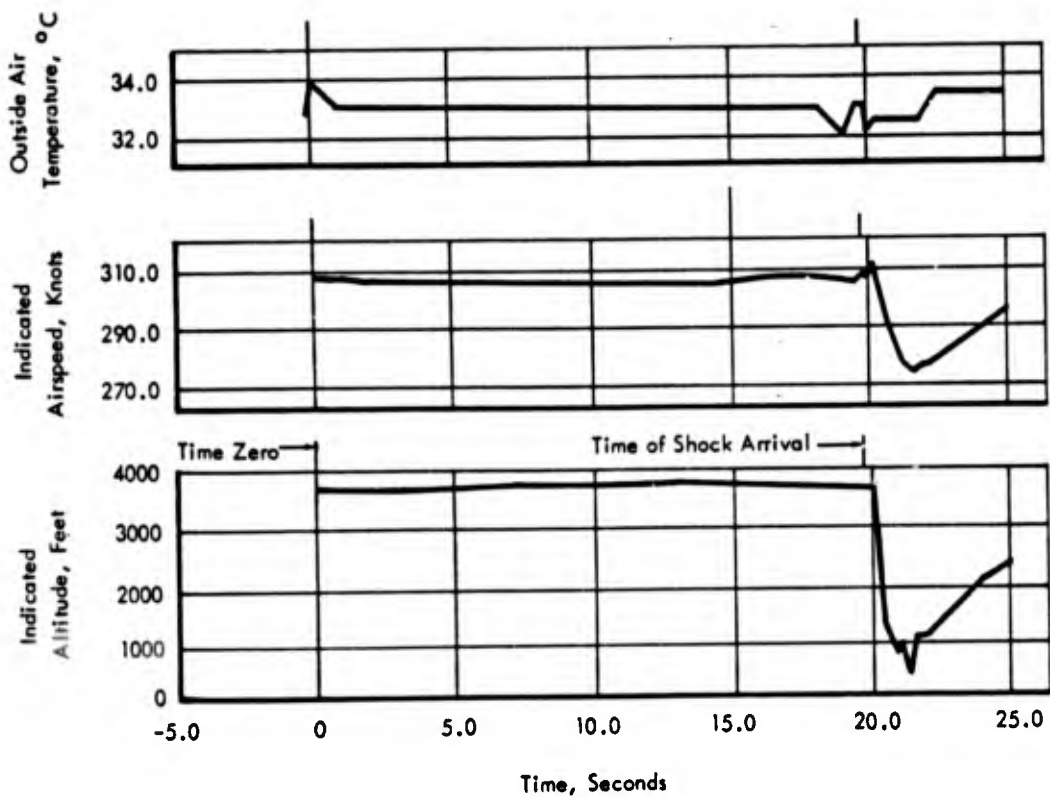


Figure G.4 Indicated altitude, airspeed and outside-air temperature for Aircraft 139467, Shot Koa.

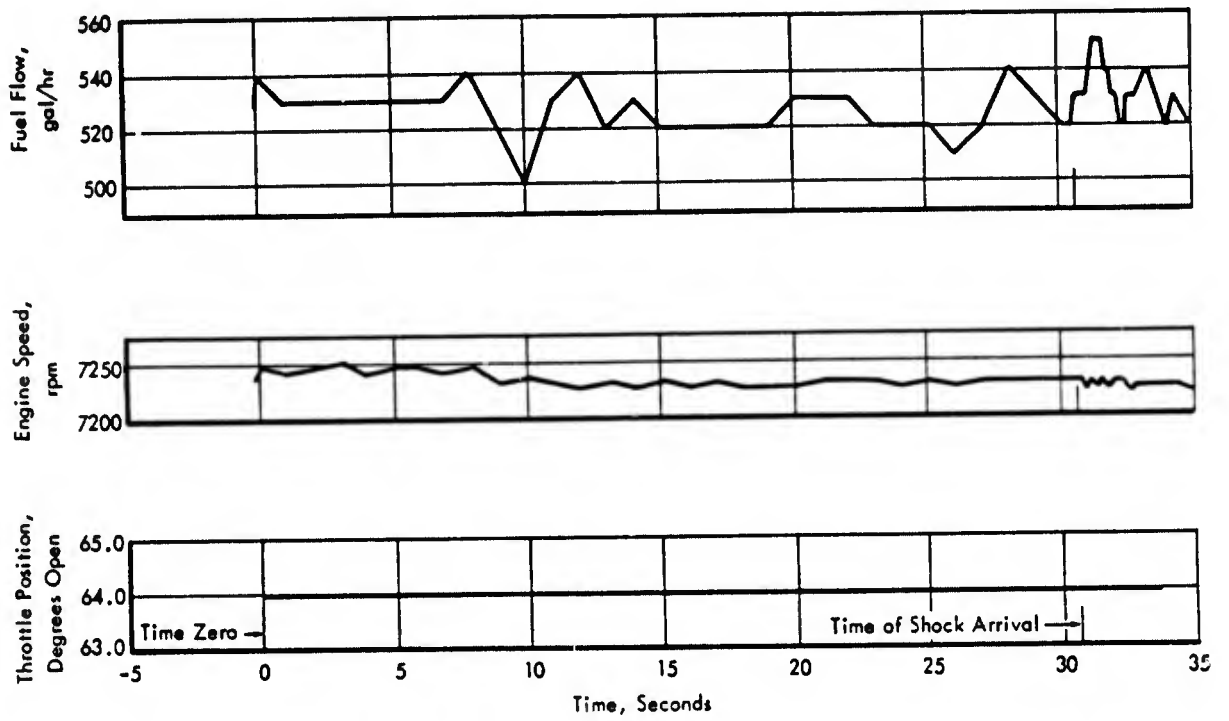


Figure G.5 Throttle position, engine speed and fuel flow for Aircraft 139467, Shot Yellowwood.

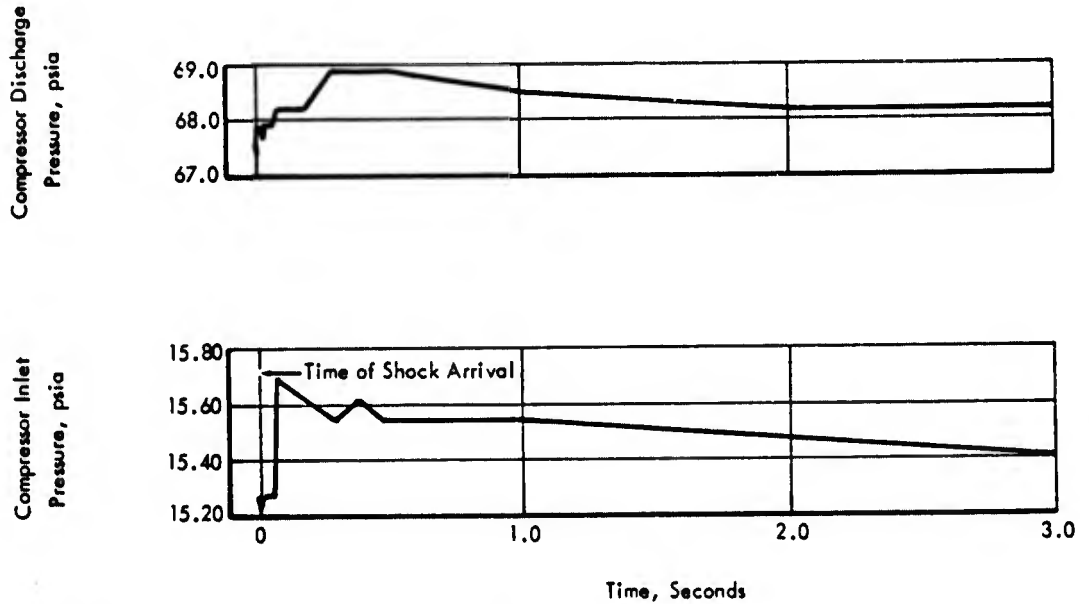


Figure G.6 Compressor inlet and discharge pressures for Aircraft 139467, Shot Yellowwood.

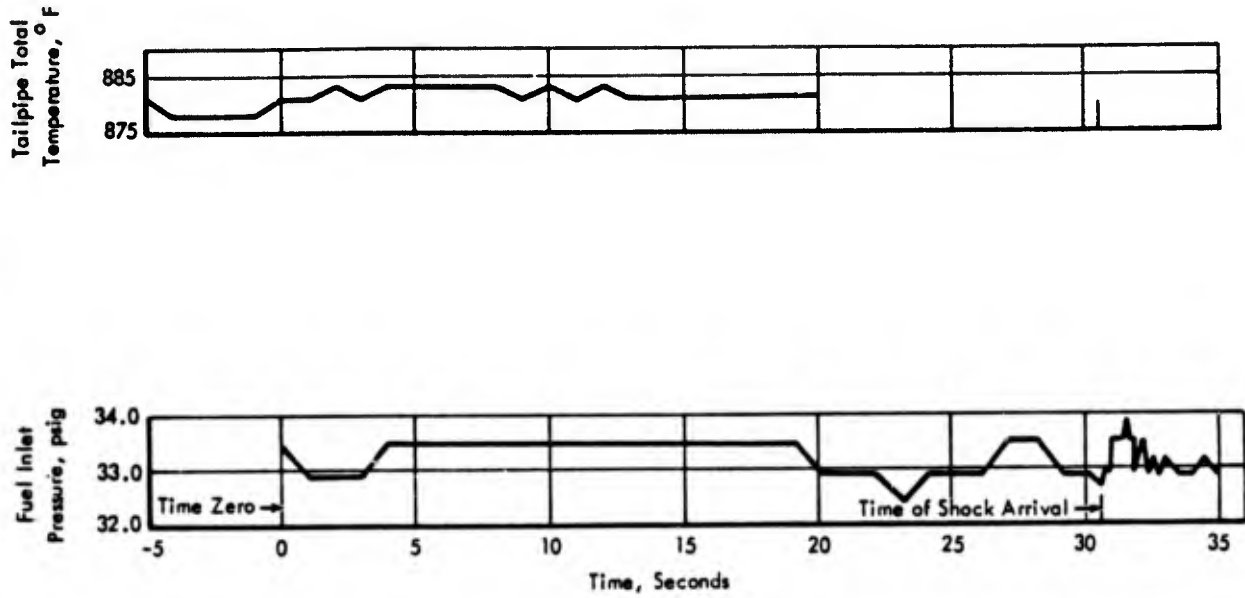


Figure G.7 Fuel inlet pressure and tailpipe total temperature for Aircraft 139467, Shot Yellowwood.

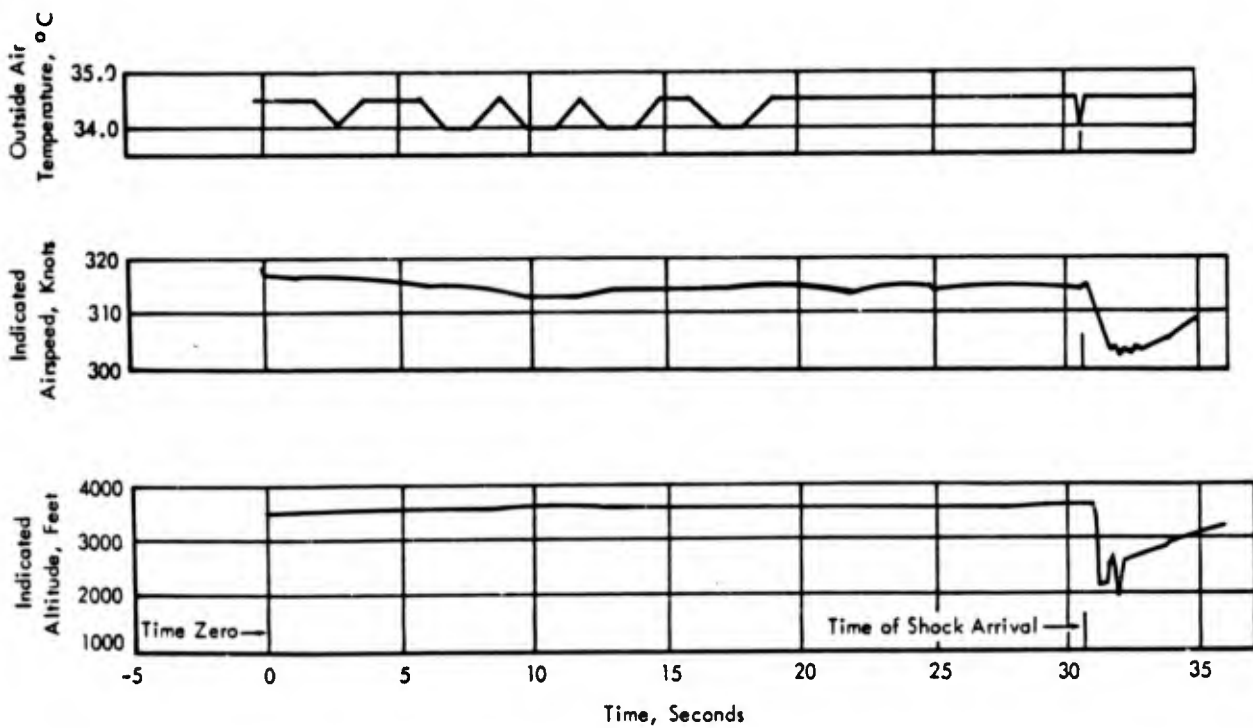


Figure G.8 Indicated altitude, airspeed and outside-air temperature for Aircraft 139467, Shot Yellowwood.

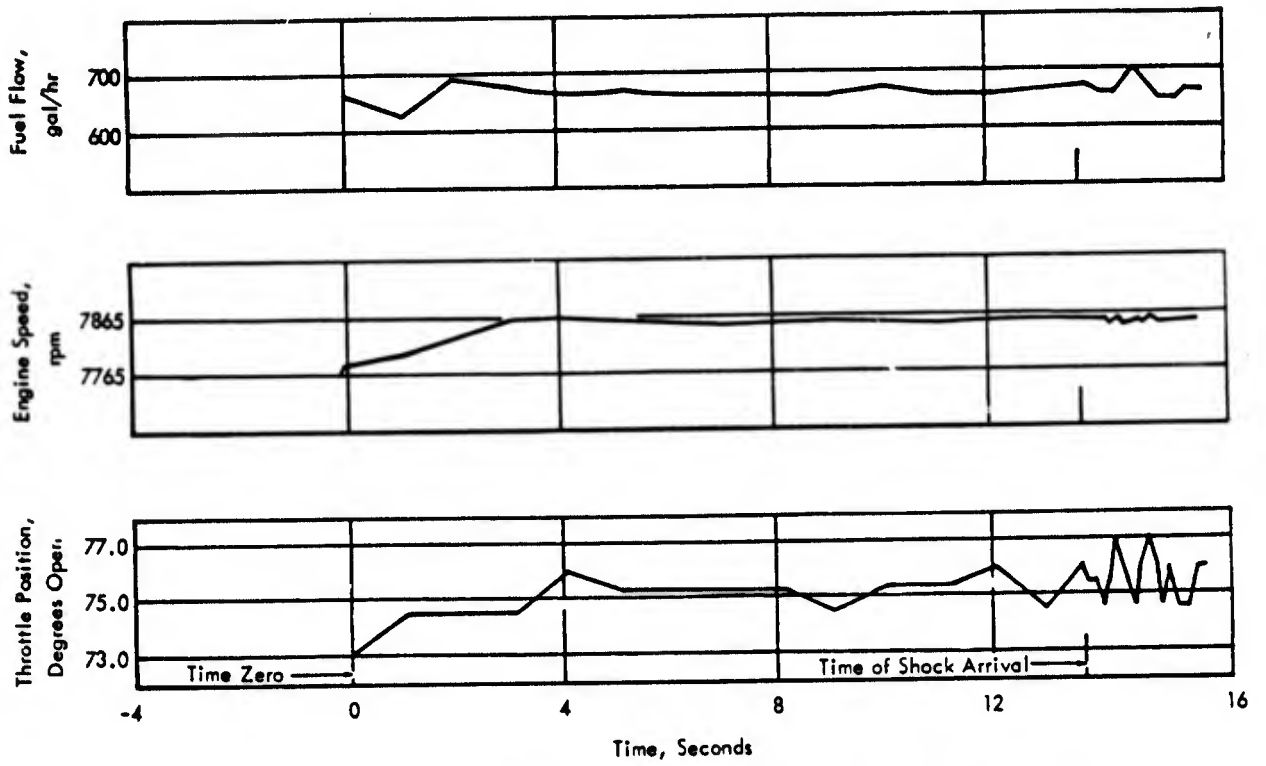


Figure G.9 Throttle position, engine speed and fuel flow for Aircraft 139467, Shot Tobacco.

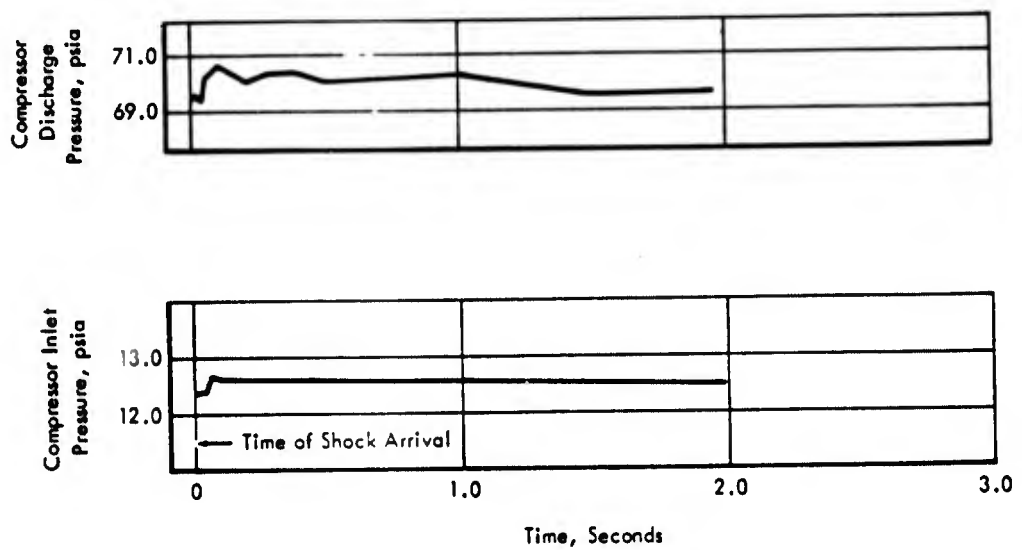


Figure G.10 Compressor inlet and discharge pressure for Aircraft 139467, Shot Tobacco.

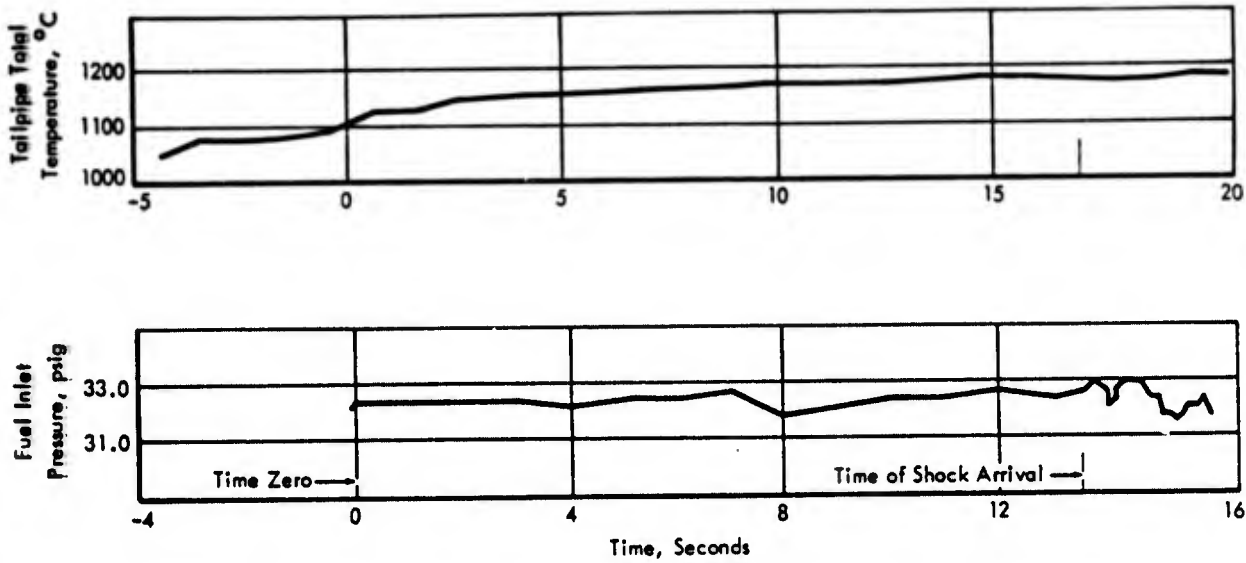


Figure G.11 Fuel inlet pressure and tailpipe total temperature for Aircraft 139467, Shot Tobacco.

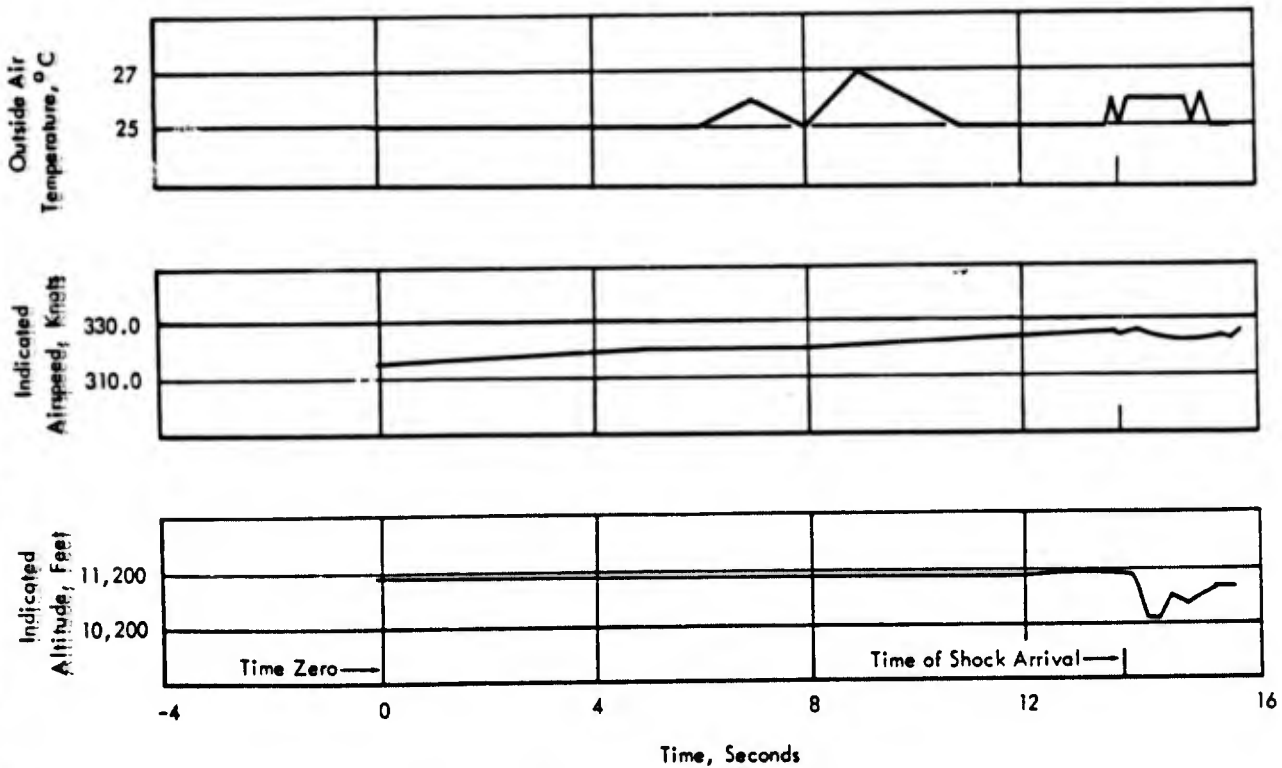


Figure G.12 Indicated altitude, airspeed and outside-air temperature for Aircraft 139467, Shot Tobacco.

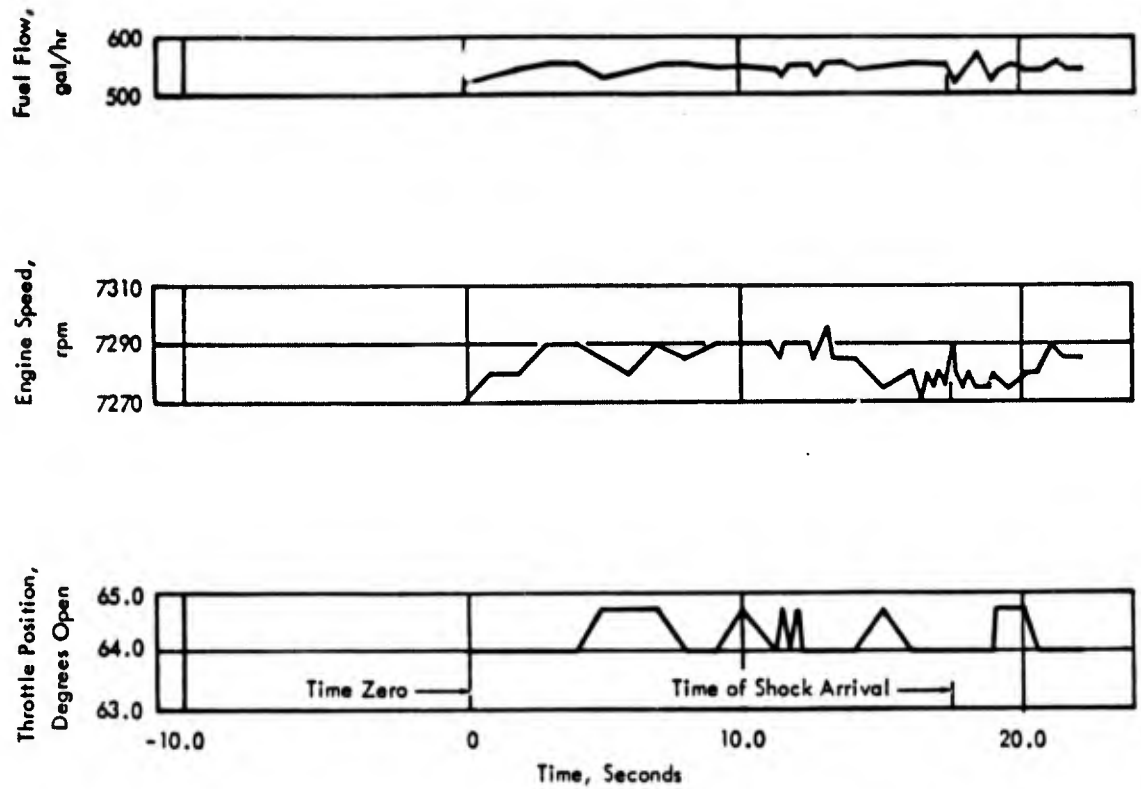


Figure G.13 Throttle position, engine speed and fuel flow for Aircraft 139467, Shot Rose.

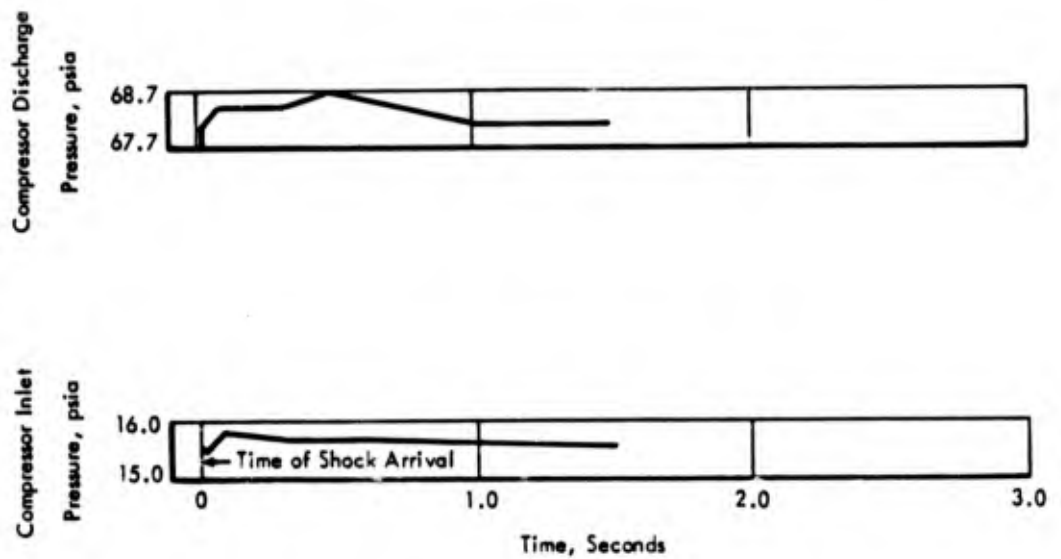


Figure G.14 Compressor inlet and discharge pressures for Aircraft 139467, Shot Rose.

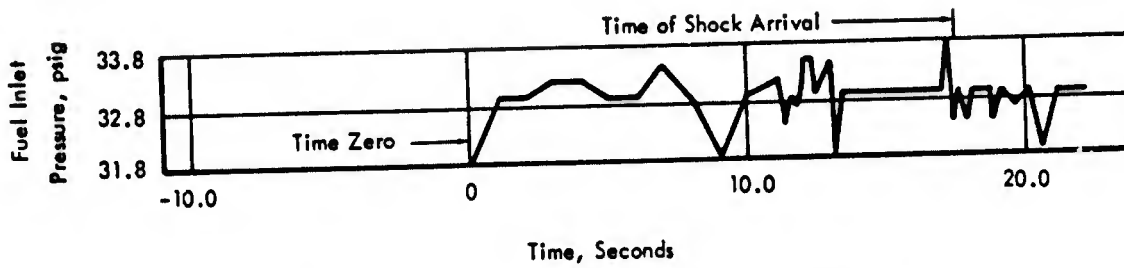
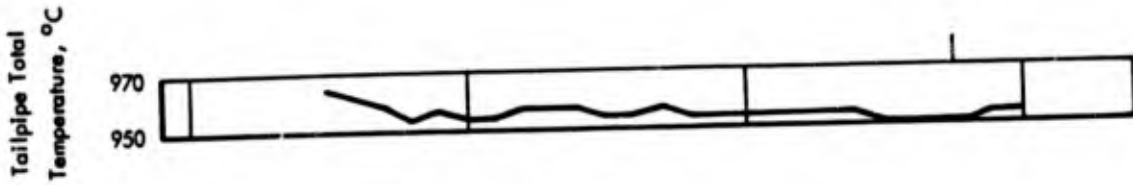


Figure G.15 Fuel inlet pressure and tailpipe total temperature for Aircraft 139467, Shot Rose.

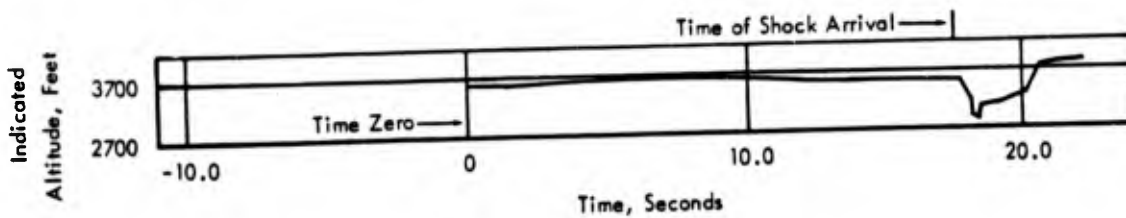
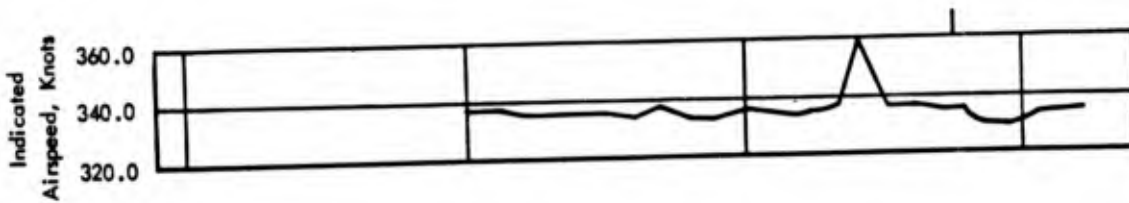
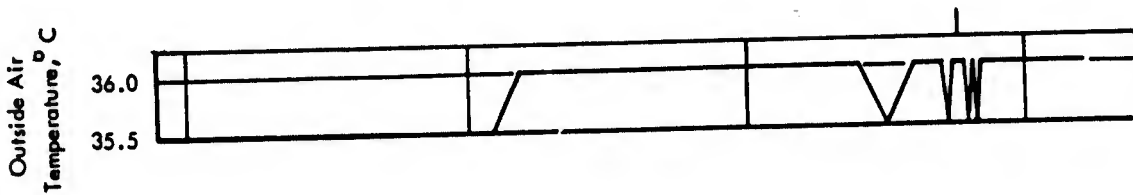


Figure G.16 Indicated altitude, airspeed and outside-air temperature for Aircraft 139467, Shot Rose.

REFERENCES

1. A. N. Julian; "In-Flight Structural Response of FJ-4 Aircraft to Nuclear Detonations"; Project 5.3, Operation Plumbbob, WT-1432, February 1960; Bureau of Aeronautics, Washington 25, D. C. and North American Aviation, Inc., Columbus Division, Columbus, Ohio; Confidential.
2. Commander, Field Command, AFSWP, Albuquerque, New Mexico; Letter to Bureau of Aeronautics Representative, North American Aviation, Inc., Columbus, Ohio; FCWT1/AG, Subject: "Hardtack Yields as of 8 October 1958 (U)", 3 November 1958; Secret Formerly Restricted Data.
3. Chief, Bureau of Aeronautics, Department of the Navy, Washington, D. C.; Letter to: North American Aviation, Inc., Columbus, Ohio; Aer-AD-41, Serial 001609, Subject: "Revised Hardtack Yields", 21 October 1958; Secret Formerly Restricted Data.
4. "Nuclear Weapon Effects Criteria for Naval Aircraft"; BUAERINST 03401.1, 10 March 1959; Bureau of Aeronautics, Department of the Navy, Washington, D. C.; Confidential.
5. "Capabilities of Atomic Weapons"; Department of the Army Technical Manual TM 23-200, Department of the Navy OPNAV Instruction 03400.1B, Department of the Air Force AFM 136-1, Marine Corps Publication NAVMC 1104 Rev; Revised Edition, November 1957; Prepared by AFSWP, Washington, D. C.; Confidential.
6. R. F. Smiley and E. L. Krasnoff; "Unsteady Aerodynamic Forces on Subsonic Aircraft Exposed to Blast Gusts of Arbitrary Orientation"; WADC TR 57-594, June 1958; Wright Air Development Center, Wright-Patterson Air Force Base, Ohio; Unclassified.
7. Gabriel, Wallner, and Lubick; "Some Effects of Transients in Inlet Pressure and Temperature on Turbojet Engines"; Presentation at the 25th Annual IAS Meeting, January 28-31, 1957; IAS Preprint No. 709; Unclassified.
8. D. A. Smith; "An Analysis of the Thermal Flux from Low Altitude Nuclear Detonations"; NA59H-251, 1 December 1959; North American Aviation, Inc., Columbus Division, Columbus 16, Ohio; Secret Restricted Data.
9. L. M. Barker; "Diffused Reflection of Radiation from Spherical and Hemispherical Sources to an Inclined Receiver"; SC-3827(TR), 4 April 1956; Sandia Corporation, Albuquerque, New Mexico; Secret Restricted Data.
10. R. M. Chapman and M. H. Seavey; "Preliminary Report on the Attenuation of Thermal Radiation from Atomic or Thermonuclear Weapons"; Air Force Surveys in Geophysics No. 59, AFCRC-TN-54-25, November 1954; Air Force Cambridge Research Center, Bedford, Massachusetts; Secret Restricted Data.
11. A. Ambrosio and T. Ishimoto; "Analytical Studies of Aircraft Structures to Transient External Heating, Volume II, Thermal Response of a Finite Plate and the 'Thin' Plate Criterion"; WADC-TR-54-579, November 1954; Wright Air Development Center, Wright-Patterson Air Force Base, Ohio; Unclassified.
12. K. C. Holmboe; "An Analysis of the Thermal Response of Bonded Aluminum Honeycomb Structure to Nuclear Detonations"; NA60H-192, 1 April 1960; North American Aviation, Inc., Columbus Division, Columbus, Ohio; Confidential.

13. B. E. Gatewood; "Thermal Stresses"; 1957; McGraw-Hill Book Company, Inc., New York, N. Y. ; Unclassified.
14. R. D. Lennel and others; "The Effects of Atomic Explosions on Aircraft - Vol. II, The Characteristics of Explosions"; WADC TR 52-244, January 1953; Wright Air Development Center, Wright-Patterson Air Force Base, Ohio; Secret.
15. R. W. Harr and G. L. Spencer; "Analysis of Nuclear Blast Overpressure Time Histories as Seen by a Moving Observer"; NA59H-755, 31 December 1959; North American Aviation, Inc., Columbus, Ohio; Secret.
16. R. L. Blispinghoff, H. Ashley, and R. L. Hoffman; "Aeroelasticity"; 1955; Addison-Wesley Publishing Company, Reading, Massachusetts; Unclassified.
17. R. H. Scanlan and R. Rosenbaum; "Introduction to the Study of Aircraft Vibration and Flutter"; 1951; Macmillan Company, New York, N. Y. ; Unclassified.
18. A. W. Walker; "Instrumentation Summary for Special Weapons Effects Tests, Operation Hardtack, Project 5.3"; NA58H-330, 11 May 1959; North American Aviation, Inc., Columbus Division, Columbus, Ohio; Confidential.